DESIGN AND IMPLEMENTATION OF PERFORATION ON HIGH FILL FACTOR STRUCTURES FOR UNCOOLED INFRARED SENSORS

A THESIS SUBMITTED TO
THE GRADUATE SCHOOL OF NATURAL AND APPLIED SCIENCES
OF
MIDDLE EAST TECHNICAL UNIVERSITY

BY

RAMAZAN ÇETİN

IN PARTIAL FULFILLMENT OF THE REQUIREMENTS
FOR
THE DEGREE OF MASTER OF SCIENCE
IN
ELECTRICAL AND ELECTRONICS ENGINEERING

AUGUST 2016

Approval of the thesis:

DESIGN AND IMPLEMENTATION OF PERFORATION ON HIGH FILL FACTOR STRUCTURES FOR UNCOOLED INFRARED SENSORS

submitted by **RAMAZAN ÇETİN** in partial fulfillment of the requirements for the degree of **Master of Science in Electrical and Electronics Engineering Department**, **Middle East Technical University** by,

Prof. Dr. Gülbin Dural Ünver _____
Dean, Graduate School of **Natural and Applied Sciences**

Prof. Dr. Tolga Çiloğlu _____
Head of Department, **Electrical and Electronics Eng.**

Prof. Dr. Tayfun Akın _____
Supervisor, **Electrical and Electronics Eng. Dept., METU**

Examining Committee Members

Prof. Dr. Haluk Külah _____
Electrical and Electronics Eng. Dept., METU

Prof. Dr. Tayfun Akın _____
Electrical and Electronics Eng. Dept., METU

Prof. Dr. Özlem Aydın Çivi _____
Electrical and Electronics Eng. Dept., METU

Assist. Prof. Dr. Mehmet Ünlü _____
Electrical and Electronics Eng. Dept., YBU

Assist Prof. Dr. Kağan Topallı _____
Institute of Materials Science and Nanotechnology, BU

Date: _____

I hereby declare that all information in this document has been obtained and presented in accordance with academic rules and ethical conduct. I also declare that, as required by these rules and conduct, I have fully cited and referenced all referenced material and results that are not original to this work.

Name, Surname: Ramazan Çetin

Signature:

ABSTRACT

DESIGN AND IMPLEMENTATION OF PERFORATION ON HIGH FILL FACTOR STRUCTURES FOR UNCOOLED INFRARED SENSORS

Çetin, Ramazan

M.S., Department of Electrical and Electronics Engineering

Supervisor: Prof. Dr. Tayfun Akın

August 2016, 90 pages

This thesis presents the design and implementation of the perforation on high fill factor structures; e.g., umbrella structures, for uncooled infrared detectors. The study is mostly focused on the effect of the perforation on the absorption performance of the sensor pixels. The introduction of the perforation to the umbrella structure is expected to improve the absorption performance which can be degraded due to a trending issue nowadays, the pixel size reduction. In literature, perforation is also proposed to decrease the thermal time constant, to relieve the low vacuum requirements and to ease the etching of the underneath layers.

Within the scope of this study, a canonical topology including only the perforated umbrella structure, but still resembling to the full pixel case, is designed, optimized and fabricated successfully. The canonical topology is used for the optimization of the perforated structures to have a high enough, broadband absorption rate in the LWIR (Long Wave Infrared, 8μm-12μm) range using the Cascaded Transmission

Line (CTL) technique and the commercial High Frequency Structural Simulator (HFSS) program. The LWIR is the optimized infrared range to get images of the objects having a body temperature around 300 Kelvin. Through these optimizations, a perforation ratio of 50%; i.e., the ratio of the perforation size to the period size is equal to 0.5, is advised to be the optimized value both to have a good absorption performance and also to benefit from other improvements that the perforation offers. The Frequency Transform Infrared (FTIR) spectroscopy results of a successful implementation of perforation on high performance pixels is presented, an average of 90% absorption rate is obtained in the LWIR range. Additionally, a contactless and non-destructive characterization of the absorbing Nichrome (NiCr) layer is presented. Also an improvement by more than 10% with the thermal time constant with the introduction of the perforation is proved through thermal simulations.

Keywords: Microbolometers, Perforation, Frequency Selective Surfaces, High Fill Factor Structures, MEMS Fabrication.

ÖZ

PERFORASYON İÇEREN YAPILARIN KIZILÖTESİ SENSÖRLER İÇİN YÜKSEK DOLULUK ORANLI YAPILARA TASARIMI VE UYGULAMASI

Çetin, Ramazan

Yüksek Lisans, Elektrik ve Elektronik Mühendisliği Bölümü

Tez Yöneticisi: Prof. Dr. Tayfun Akın

Ağustos 2016, 90 sayfa

Bu tez, soğutmasız detektörler için yüksek doluluk oranlı yapılar üzerine perforasyon (delikli yapılar oluşturma) tasarım ve uygulamasını sunmaktadır. Çalışmada, temelde, perforasyonun soğutmasız detektörlerin kızılötesi emilim performansına etkisi incelenmektedir. Literatürde, son zamanlarda piksel boyutlarının küçültülmesi yönünde genel bir eğilim mevcuttur. Küçültmeden kaynaklı problemlerin çözümü için ise şemsiye yapılarının kullanımı önerilmektedir. Bu tezde bu yapıların ayrıca delikli hale getirilerek kızılötesi emilim performansının artırılması amaçlanmaktadır. Delikli yapılar, bu işlevi dışında, ısıl zaman sabitinin iyileştirilmesi, detektörün vakum gereksinimlerinin azaltılması ve özellikle şemsiye yapılarının altında bulunan diğer yapıların aşındırılmasında kolaylık sağlaması için de önerilmektedir.

Bu tez çerçevesinde yapılan çalışmalarda, öncelikli olarak elektromanyetik benzetim maliyetini düşürmek için kanonik bir yapı önerilmiştir. Kanonik yapı sadece delikli yapıları içeren bir şemsiye yapısı olarak seçilmiştir. Perforasyon ile ilgili boyutlar uzun dalga kızılötesi (Long Wave Infrared, LWIR, (8-12) μm) emilim aralığı için

basamaklı iletim yolu yöntemi (Cascaded Transmission Line, CTL) ve yüksek frekans için yapısal çözümleme yapabilen ticari bir program (High Frequency Structural Simulator, HFSS) kullanılarak optimize edilmiştir. Bu arada şemsiye yapısında gömülü, elektromanyetik emilimi yüksek olan Nikrom malzemesi temassız ve malzemeye zarar vermeyen bir yöntemle karakterize edilip benzetim programına gömülmüştür. Optimize edilen perforasyon oranı %50 olarak belirlenmiştir, yani perforasyon açıklığının yine perforasyon periyoduna oranı 0,5 olarak optimize edilmiştir. Bu değer aşılmadığı sürece delikli şemsiye yapısının (8-12)μm aralığındaki emilim performansının en kötü ihtimalle korunduğu gözlemlenmiştir. Buradan elde edilen sonuçlar neticesinde, %50 perforasyon oranı, yüksek performanslı mikrobolometre piksellerine uygulanmış ve aynı şekilde emilim performansının değişmediği gözlemlenmiştir. Ölçümler neticesinde (8-12) μm emilim aralığındaki kızılötesi dalga emilim oranının %90 civarında olduğu ayrıca gözlemlenmiştir. Bir diğer konu ise, perforasyonun ısıl zaman sabitine olan etkisi, ısıl benzetimler neticesinde bu zaman sabitindeki olası iyileşmenin %10 ‘dan fazla olabileceği hesaplanmıştır.

Anahtar Kelimeler: Mikrobolometre, Yüksek Doluluk Oranlı Yapılar, Perforasyon (delikli yapılar oluşturma), Frekans Seçici yüzeyler, MEMS Üretimi.

To,

All restless minds.

ACKNOWLEDGEMENTS

First of all, I would like thank to my thesis advisor Prof. Dr. Tayfun Akın for his support, guidance, and encouragement during my graduate studies. I also would like to thank to Orhan Şevket Akar, Ozan Ertürk, Feyza Oruç, Bilge Temiz, Özgecan Dervişoğlu, Eren Canga and Selçuk Keskin for their support and help throughout my research.

I would like to thank to METU-MEMS members, Mustafa Yıldırım, Akın Aydemir, Adem Saraç, Ahmet Murat Yağcı, Başak Kebabcı, Evren Erdil, Taylan Töral, Talha Köse, Hasan Doğan Gavcar, Gülşah Demirhan, Eyüp Can Demir, Oğuzhan Temel, Yunus Terzioglu, Ulaş Aykutlu and Ferhat Yeşil for their support and friendship.

Last, but not least, I would like to thank to my family for their support and encouragement.

TABLE OF CONTENTS

ABSTRACT v

ÖZ vii

ACKNOWLEDGEMENTS x

TABLE OF CONTENTS xi

LIST OF TABLES xiii

LIST OF FIGURES xiv

CHAPTERS

1. INTRODUCTION 1

1.1 Infrared Radiation 1

1.2 A Brief History Regarding the Evolution of the Infrared Detection Technology 4

1.3 Infrared Detection Technologies 6

1.3.1 Photon Based IR Technology 7

1.3.2 Thermal Based IR Technology 8

1.4 Absorption Enhancement for Uncooled IR Detectors 26

1.5 Research Objectives and Thesis Organization 28

2. INFRARED CHARACTERIZATION OF UMBRELLA LAYERS 31

2.1 Spectroscopic Ellipsometry Technique 31

2.2 IR Characterization of Silicon Nitride Material 33

2.2.1 Verification by Simulation Results 36

2.3 IR Characterization of the NiCr Based Absorber Layer 39

2.3.1 Dispersive Model 39

2.3.2 Non-Dispersive Model 40

3. DESIGN AND FABRICATION OF PERFORATED STRUCTURES..... 47

3.1 Design and Simulation of Perforated Umbrella Structures..... 47

3.2 Fabrication of Perforated Umbrella Structures 54

3.3 A Comparison of the FTIR Measurement versus HFSS Simulation Results 66

3.4 Application of Perforation on High Performance Pixels 75

3.4.1 IR Absorption Performance..... 75

3.4.2 Thermal Simulations..... 78

4. CONCLUSION AND FUTURE WORK..... 83

5. REFERENCES 85

LIST OF TABLES

TABLES

Table 3-1: A schematic representation of the placement of various types of pixels in one die, changing in pixel pitch sizes, period sizes, perforation sizes, post number and sizes. Each die involves pixels in 20 rows and 4 columns (a total of 78 pixels). With this run, the effect of the NiCr and the perforation is also tested differentially. NN acronym explains for the 'No Nichrome' case and NP explains for the 'Not Perforated' case. All pixels are successfully released as expected, the ones in red are used for FTIR measurements. 55

Table 3-2: A summary of measured and designed topology parameters for different processes and different size of pixel pitches. All C-series (C9, C14, etc.) belong to 25µm and B-series (B8, B14, etc.) belong to 17µm pixel pitch sizes. There is a noticeable difference with the Post Sizes which actually does not affect the absorption performance much, nevertheless good agreement with the Period Size is observed. However there is noticeable over-etching problem observed with the Recess Size differences which will affect quite the absorption performance. I can optimize it with a few optimization trials with the lithography...... 64

Table 3-3: Tabulated simulation data for the thermal time constant (TTC) of 25µm pixels with umbrella structures for different body nitride thicknesses and for various perforation rates. Simulations suggest that there is an improvement by 10% to 16% with the thermal time constant for a 50% perforation rate. The period size is 3.0µm. 80

LIST OF FIGURES

FIGURES

Figure 1.1: Spectral distribution of thermal radiation for various temperature values assuming emissivity of unity for all wavelength range. As the temperature increases the maximum loci of the distribution shifts to the lower wavelength values. *3*

Figure 1.2: Transmission of the atmosphere for a 6000 ft. horizontal path over the sea level with a precipitation of 17mm, [5]. This is a generic plot of IR characteristics of the atmosphere; the dips in the transmission graph are due to the naturally existing absorbing molecules such as CO_2 and H_2O in the atmosphere. The graph shows the various IR windows which can be exploited to transmit the IR radiation with minimum loss. These windows are directly related to evolution of the various range IR technologies such as Mid Wave IR (MWIR) exploiting the (3-5) µm window and Long Wave IR (LWIR) exploiting the (8-12) µm window. *4*

Figure 1.3: The graph of the measured Resistance vs. Temperature (R-T) change (a) and the graph of the calculated TCR vs. Temperature change (b) of a specific Thin Film Resistor (TFR) produced at METU MEMS Center are shown. The R-T graph is obtained by simultaneously observing the resistance change and the temperature change of the TFR, while it is placed into a temperature controlled oven. The TCR is calculated by fitting the measured R-T data into the Arrhenius relation by using a two dimensional fitting algorithm and finding the activation energy (E_a) in return. While the fitted value of E_a for this specific sample is found to be 0.22eV, the calculated TCR value is to be around -2.9%/˚C @25˚C in accordance with. *10*

Figure 1.4: Simplified thermal circuit representation for a generic thermal detector, representing the dynamic temperature response of the detector. The model incorporates the thermal isolation concept into the equation through a detector specific thermal conductance, G_{th}, parameter, the thermal mass of the thermally isolated part, with a detector specific thermal capacitance, C_{th}, parameter and the quantity of the infrared power exposure with a generic source power, P_0, parameter. *13*

Figure 1.5: The block diagram of a generic responsivity measurement setup, [18]. The adjustable infrared (IR) power is generated by the Blackbody source. The generated IR signal is incident upon the single pixel (Device Under Test, DUT) to be tested. The single pixel is placed in vacuum environment (DEWAR). A voltage output at each chopper frequency can be read, if a current bias is applied. Examining the frequency characteristics of the output voltage, both the responsivity and the thermal time constant can be determined simultaneously. *14*

Figure 1.6: The graph of the measured and the fitted generated voltage obtained from a generic resistor type single pixel detector produced at METU MEMS Center. By dividing the generated voltage value by the absorbed incident IR power, the

responsivity parameter is obtained. For this specific example, the fitted DC voltage is found to be 1377μ-Volts (μV) and the time constant to be 8.5 milliseconds (msec). 15

Figure 1.7: The Scanning Electron Microscope (SEM) image (a) and IR image (b) obtained from DRS U6160 Model 640x480 IRFPA. This model has a pixel pitch of 17μm, working in LWIR range (8-14)μm, has an NETD of less than 40mK @ f/1.0 optics, and a time constant of less than 14msec,[28], [32], [33], [34]. 19

Figure 1.8: The SEM image (a) and IR image (b) obtained from 320X240 IRFPA produced by METU MEMS Center. The FPA has a pixel pitch of 50μm, working in LWIR range (8-14)μm, has a measured NETD of around 450mK @ f/1.0 optics, and a time constant of around 15msec,[36]. 20

Figure 1.9: The cross sectional schematic representation (a), SEM image (b) and IR image (c) obtained from 640X480 IRFPA based on SOI diodes, produced by Mitsubishi. The FPA has a pixel pitch of 25μm, working in LWIR range (8-14) μm and has a measured NETD of around 40mK @ f/1.0 optics, [41]..... 21

Figure 1.10: The oblique view of schematic representation (a) and SEM image obtained from 128X128 IRFPA based on p+-active/n-well diode, produced by METU MEMS Center. The FPA has a pixel pitch of 40μm, working in LWIR range (8-14)μm and has a measured NETD of around 1000mK @ f/1.0 optics with a time constant around 36msec, [46]. 22

Figure 1.11: The oblique view of schematic representation (a), SEM image (b) and IR image (c) obtained from 128X128 IRFPA based on p+-active/n-well SOI diode, produced by METU MEMS Center. The FPA has a pixel pitch of 70μm, working in LWIR range (8-14)μm and has a measured NETD of around 1100mK @ f/1.0 optics with a time constant around 46msec, [16]..... 23

Figure 1.12: The oblique view of schematic representation, (a) and SEM image, (b) obtained from 160X120 IRFPA based on p+-active/n-well SOI diode, produced by METU MEMS Center. The FPA has a pixel pitch of 50μm, working in LWIR range (8-14) μm and has a measured NETD of around 280mK @ f/1.0 optics. Within the scope of this study, while the fill factor of the low-cost detector pixels with 50μm pitch is increased from 46% to 92%, the responsivity of the FPAs is increased by 30% with the implementation of the umbrella structures over the diode including bodies, [47]. 24

Figure 1.13: The schematic view (a) and SEM graphs (b, c) of a simple mass producible uncooled thermoelectric infrared. . In air at room temperature, the sensor has a responsivity of 71.6V/W, noise equivalent power of 0.64nW/$Hz^{1/2}$, detectivity of 6.21×10^7cm. $Hz^{1/2}$/W and a time constant of 13.2msec, [55]..... 26

Figure 1.14: Schematic views to represent the two different topologies to implement the high fill factor structures in the literature, [28], [37]. One of them involves the isolating arms and the active material on different levels of the detector separated with an air gap, (a), which is difficult to realize in practice. The other one involves both the isolating arms and the active material on the same level, the second level is only responsible for the IR absorption..... 28

Figure 1.15: The SEM image and the regarding percentage absorption rate of a single pixel composed of a spaced apart body and umbrella structure, [71]. There is

an absorption enhancement in a narrow band around 9μm by 10%. The key issue here is actually not to degrade the absorption performance while decreasing the thermal mass with perforation as it will be underlined in this study. 29

Figure 1.16: SEM image (a) and absorption characteristics (b) of 17μm pixel pitch 640x512 IRFPA employing double sacrificial layer microbolometers with perforated umbrella structures as the absorber structures, amorphous vanadium oxide thin film as the active layer. NETD of 35mK @300K with f/1.0 optics is obtained. With the second platform incorporating frequency selective surface; i.e., perforation, responsivity of the microbolometer is improved by 30% over (8-14) μm range, [73]. 30

Figure 2.1: Schematic representation of the ellipsometric measurement. The incident linear polarization (E_{is}, E_{ip}) is disturbed after the interaction of the EM with the sample material resulting in another polarization (E_{rs}, E_{rp}). Two polarizations, s and p, represent the parallel and orthogonal components of both incident and the reflected field with respect to the plane of incidence, [74]. 33

Figure 2.2: Schematic representation of the deposition of several layers to characterize the Silicon Nitride (Si_3N_4) material. The blank wafer of Silicon (Si) is deposited over with 100nm Au layer for full reflection purposes and then 200nm of Si_3N_4 layer is deposited for the characterization. 34

Figure 2.3: Ellipsometric characterization of 200nm Si_3N_4 over 100nm Au through IR-VASE. Psi (Ψ) parameter, which is correlated to the amplitude change with the polarization (a) and the Delta (Δ) parameter, which is correlated to the phase change with the polarization (b), are shown. For thin layers, Psi is not a sensitive one as you may also observe while Delta is quite sensitive to spectral change. The peaks in the figure give an idea about the absorption bands. 35

Figure 2.4: The measured complex permittivity values of the Si_3N_4 by the IR-VASE Ellipsometry (a) and the thickness measurement result (b). The nitride thickness seems to be around 172nm, which is verified through cross-sectional SEM examination. 36

Figure 2.5: The unit cell simulation setups for the Floquet based (a) and the PML based (b) approaches in HFSS for a Si3N4 slab of 1μm thickness. They are equivalent techniques, PML box and the incident plane wave excitation both can replace the Floquet port concept 38

Figure 2.6: A comparison of the simulation results regarding the percentage absorption rate for a Si3N4 slab of 1μm thickness with different simulation setups. They seem all consistent, the subtle differences near 20μ can be blamed for the different fitting algorithms for the embedded optical constants employed by the simulation programs, i.e., it is expected. Nevertheless the variation in percentage absorption rate is at most 5% for lower frequencies. 38

Figure 2.7: Measured complex permittivity belonging to a NiCr sample of 15nm thickness. The measurement is done through SENDIRA IR ellipsometer. The sample is deposited with DC magnetron sputtering technique. An average percentage absorption of 77% for the total device, employing V_2O_5 as the active material, is reported with this study, [81]. 40

Figure 2.8: The topology used in the non-dispersive characterization of the NiCr layer, (a) and the FTIR absorption characteristics of the topology, (b) to examine the correlation between the deposition time and the sheet resistance (R_s) of the NiCr layer. The characterization is done over a fitting of the FTIR measurements between the Cascaded Transmission Line (CTL) pre and FTIR measurements. For the 90sec. case, the fitting is good and the R_s is determined to be around 400Ω/□. For the 200sec. case, the fitting is also successful and the R_s is determined to be around 150Ω/□, which is less than the 90 sec. case. A thicker NiCr layer resulted in a smaller sheet resistance as expected. *41*

Figure 2.9: Schematic representation of the application of the Cascaded Transmission Line (CTL) code for the topology shown in Figure 2.8 – (a), used for the non-dispersive characterization of the NiCr layer. *42*

Figure 2.10: The simultaneous optimization of the sheet resistance of the NiCr and the thickness of the Silicon Nitride layer is done through a CTL code. The goal function is the FTIR measurement regarding a deposition time of 90 sec. for the NiCr layer. The R_s is predicted to be around 400Ω/□ with this code. The optimization with a narrow band around (3 - 8) μm is more reliable since it contains the maximum absorption value and also disregards the CO_2 absorption range (4.16-4.76) μm, i.e.; (2100-2400) cm^{-1}. The thickness measurement of the Silicon Nitride layer with the ellipsometry and the SEM examination also makes this fitting much more reliable. *44*

Figure 2.11: The simultaneous optimization of the sheet resistance of the thin IR absorbing NiCr layer and the thickness of the Silicon Nitride layer is done through a CTL code. The goal function is the FTIR measurement regarding a deposition time of 200 sec. for the NiCr layer. The R_s is predicted to be around 150Ω/□ with this code. The optimization with a narrow band around (3-8) μm is more reliable since it contains the maximum absorption value and disregards the CO_2 absorption range (4.16-4.76) μm, i.e.; (2100-2400) cm^{-1}. *45*

Figure 2.12: The absorption performance of the thin, absorbing NiCr layer after exposure to various O_2 plasma recipes. It is shown that O_2 plasma recipes degrade the absorbing performance unless the NiCr layer is passivated with an additional Si_3N_4 layer. *46*

Figure 3.1: 3D model of the designed unit cell to represent the perforated umbrella structures embedded into the HFSS simulation program. The nitride layers are defined as the new materials for HFSS by embedding the frequency dependent EM parameters (n, k). Since the nominal thickness of the NiCr layer is in the order of a few nanometers, the ellipsometric characterization of this layer was unsuccessful. Thu a 2D resistive layer modelling for this layer is employed through a contactless field based FTIR measurement. *48*

Figure 3.2: Schematic representation of the application of the CTL (Cascaded Transmission Line) code for the suspended umbrella structures. The CTL method assumes un-patterned, 1D (infinite sheets of layers) which has only a thickness in the propagation direction of the EM wave. Thus, this method cannot explain for the effect of the perforation yet. *49*

Figure 3.3: Percentage absorption rate of a unit cell for a canonical single perforation umbrella structure with various thicknesses of the bottom nitride; 100nm, 200nm, 400nm and 600nm. All configurations are covered with a top nitride of 50nm

thickness. R_s is set to be 377Ω/□ the air gap thickness is 2.0μm, the period size is 2.0 μm and there is no perforation. It is observed that as the thickness of the bottom nitride increases, the average percentage absorption in the LWIR range decreases and the peak in MWIR range shifts to lower frequencies. The structure seems to be a dual band device in terms of absorption performance. It is also observed that both the analytical (CTL) and numerical (HFSS) calculations give exactly the same results for the field calculations. 50

Figure 3.4: Sensitivity analysis of the proposed topology. This analysis gives an idea about the robustness of the topology against to the small process variations. The analysis is done for an average absorption rate in LWIR (8 - 12) μm range. The assumption is if there is a 50% change in the mean value of the related parameter how much the absorption rate would be affected. Certainly, in practice this much of change is not expected however still gives an idea. The most sensitive parameter seems to be the air gap thickness and the least sensitive one is the thickness of bottom Silicon Nitride layer. Considering the practical process related variations, the topology is quite robust. 51

Figure 3.5: A parameter sweep for the perforation size and for various period sizes over the average absorption within the LWIR range. These results show that the size of the perforations should not exceed the 50% of the period sizes, (f) not to degrade the absorption performance of the pixels in the LWIR range. 53

Figure 3.6: The effect of the post size on the absorption performance is examined for two pixel pitch sizes; 25μm and 12μm. The PML (Perfect Matched Layer) method with the Incident Plane Wave (IPW) is used for the simulations in HFSS. The unit cell used for the umbrella optimizations belongs to 50 % perforation percentage rate. The results show that the post diameter should not exceed the 25% of the pixel pitch size not to degrade the absorption performance in the LWIR range. 54

Figure 3.7: Process flow of the canonical perforated umbrella structures from plain wafer up to the release of the suspended structures (a-h). With this process flow, various sizes of pixel pitches, 12μm, 17μm, 25μm and 50μm with various sizes of perforations from 0.5μm to 3.0μm are optimized, produced and tested. 58

Figure 3.8: The SEM images of some critical steps for the process flow of the perforated umbrella structures; RIE of the sacrificial layer (a), etching of the absorbing layer (b), RIE of the umbrella nitride layers (c) and the release of the pixels (d). The sacrificial material with this run is PI2610 but satisfying results are also obtained with Level M10, another sacrificial material tested with these runs... 59

Figure 3.9: SEM images belonging to various recipes of NiCr patterning. To make a differential comparison between the w/ NiCr and w/o NiCr cases, the NiCr layer should be etched separately. This optimization had to be done since O_2 plasma or SVC cannot be used to completely strip the PR. O_2 plasma will damage the thin NiCr layer and SVC will damage the Level M10 sacrificial layer. The last trial with flood exposure seems fine enough to get meaningful FTIR measurements, still there is a side sputtering of NiCr layer though. 61

Figure 3.10: SEM images of all four cases; "with Perforation", "without Perforation", "with NiCr" and "without NiCr" for a specific type of pixel. With separate etching of the NiCr layer it is possible to make a differential analysis to

examine the effect of the perforation and the NiCr layer on the absorption performance. 62

Figure 3.11: SEM images of some of successfully released perforated umbrella configurations used in FTIR measurements. These configurations belong to P2 process with 17 µm (P2-B Series), 25µm (P2-C Series) and 50 µm (P2-D Series) pixel pitches. They all have NiCr layer deposited on them. This process is realized with the LM10 as the sacrificial layer and the NiCr layer is separately etched with Inverse Sputtering. Also with this process, there is a side-sputtering problem with the NiCr layer which is actually fixed with the P3. Still it seems that the side-sputtering problem does not seem to affect the absorption performance much after examining the measurement results. 65

Figure 3.12: These FTIR measurement results belong to the Process #2 (P2) for various pixel pitch sizes; 17µm, 25 µm and 50µm. This process is realized with LM10 as the sacrificial layer and also has a severe side sputtering problem regarding the inverse sputtering of the NiCr layer, but still the results are satisfying. All these results verify the fact that while the w/ NiCr case presents a broadband characteristic, the w/o NiCr case presents a narrow band, λ/4 resonance characteristic for the absorption performance. Also, as the perforation size exceeds the 50% of the period size, a degradation in absorption performance is observed... 68

Figure 3.13: These FTIR measurement results belong to the Process #3 (P3) for various pixel pitch sizes; 12µm, 17 µm and 25µm. This process is realized with PI2610 as the sacrificial layer and also has a severe side sputtering problem is relieved with this process. All these results verify the fact that while the w/ NiCr case presents a broadband characteristic, the w/o NiCr case presents a narrow band, λ/4 resonance characteristic for the absorption performance. Also, as the perforation size exceeds the 50% of the period size, a degradation in absorption performance is observed. 69

Figure 3.14: These FTIR measurement results belong to the Process #4 (P4) with various pixel pitch sizes, 12µm, 17µm and 25µm and w/ NiCr case. P4 is also realized with the LM10 sacrificial layer material. With this process, all umbrella layers are simultaneously etched, which means that the NiCr layer is protected during the etching processes. These results also verify that as the perforation ratio increases, at some point (~50%), a degradation with the absorption performance is observed.. With P4, observations for different period sizes are also made to verify the 50% perforation rate as the optimum value, it also checked out with the HFSS simulation results. 70

Figure 3.15: FTIR measurement results regarding the examination of the undesired process variations, such as air gap thicknesses, on the desired absorption performance for (w/ NiCr, w/o Perforation) and (w/o NiCr, w/o Perforation) cases, for various pixel pitch sizes and the processes. A cumulative effect of all undesired process related variations on the absorption performance in all IR range is observed o. The effect is more noticeable on the MWIR (3-5) µm range than on the LWIR range (8-12) µm, still not bad results. 71

Figure 3.16: The simultaneous optimization results of both the umbrella nitride thickness and the air gap thickness through CTL code. The aim function is the FTIR measurement results. The air gap is fitted to 2.3µm, which is actually the optimized

thickness during the sacrificial layer process optimizations. The nitride thickness is fitted to 190nm, which is actually quite different from the common knowledge used in the recipes it should have been (200+50) nm for both the top and the bottom nitrides. Nevertheless both results are verified through SEM inspection by observing the cross section of the layers. The total nitride layer thickness is actually measured around 190nm. 72

Figure 3.17: The simultaneous optimization results of both the top and the bottom umbrella nitride thicknesses through CTL code. For the optimization the LWIR band values are used The aim function is the FTIR measurement results. The air gap is 2.3µm and the total nitride thickness should be around 190nm from the previous optimization results. A three variable fitting also predicts the sheet resistance around 460Ω/□. This value can also be verified with the previously done NiCr layer optimizations. The nitride layer thickness is fitted to (160+20) nm which is not far from 190nm. 73

Figure 3.18: A comparison of the HFSS simulation results with the FTIR measurement results regarding the dependency of the absorption performance on the perforation sizes (duty cycles) for the w/ NiCr cases. The measurements are collected from all three processes and various pixel pitch sizes for the same period size, 3µm. All those results show that 1.5 µm perforation size for 3.0µm period size (50% Perf. Rate) is the limit to prevent any degradation with the absorption performance. The contamination can be blamed for the deviations of the FTIR measurement results from the HFSS simulation results for the larger perforation sizes. 74

Figure 3.19: A comparison of the HFSS simulation results with the FTIR measurement results regarding the dependency of the absorption performance on the perforation sizes (duty cycles) for the w/ NiCr cases and for different period sizes. All results show that 1.5 µm recess size for 3.0µm period and 2.0 µm for 4.0 µm (50% duty cycle) period is the limit to prevent any degradation with the absorption performance, which was already predicted by the HFSS simulations. 75

Figure 3.20: SEM images of 17µm single pixel structures produced at METU MEMS Center by Eren Canga. Single pixel consists of mainly the active material, supporting legs and umbrella structure..... 76

Figure 3.21: FTIR absorption measurement results of both "not perforated" and "perforated" cases belonging to two samples (Sample-1, 2) of 17µm pixel arrays. Average absorption rate in LWIR range is measured to be around 90%. The perforation rate is around 50%; i.e., the period size is 3.0µm and the perforation size is 1.4µm. The problematic etching with the active material can be blamed for the relatively bad result with Sample-2. Also the absorption rate can still be increased by tuning the air gaps, thus shifting the maximum absorption in the figures to the LWIR range. Due to non-conformal deposition of the sacrificial layer with this process run, there is still a need for fine tuning of the air gap thicknesses. Nevertheless, both measurements prove the optimized 50% perforation ratio to prevent the absorption performance from degradation. 77

Figure 3.22: Transient Thermal simulation results for a 25µm pixel with perforated umbrella structure. The total body nitride thickness is 100nm, so the arms are. In reality, this much of arm thickness cannot hold the whole structural layers, nevertheless, to prove our point with the perforations through simulations, this

thickness is still acceptable. The image is taken at the steady state. The final maximum temperature difference is about 2.6K. The perforated umbrella and the active material are heated as expected and the arms are isolating the hot spots from the ROIC part as expected. The simulation results are generated by COMSOL Multiphysics. *78*

Figure 3.23: The Transient Thermal simulation results for two different body nitride thicknesses, 100nm and 400nm. Since the maximum temperature that 100nm case is larger than the other it can be deduced that the thermal isolation is better for the 100nm case. Graphically, the performance improvement with the thermal time constant due to perforation can also be easily observed. *80*

CHAPTER I

INTRODUCTION

Detection technologies are all about devising a method exploiting some natural event, order or mechanism to harvest and process knowledge which cannot be easily done unless you lean on, differentiate it from other stuff and amplify it artificially. The artificial part includes defining an observable parameter and designing a device to sense the change in response. If there is a change, there is always information buried deep under or just left over the surface of the phenomenon waiting for to be exploited. The natural mechanism; i.e., order we are exploiting with Infrared (IR) detection is the fact that everything that has a temperature above 0K, emits thermal radiation, which is a part of the electromagnetic (EM) radiation spectrum with the wavelength range (0.7μm-1000μm), [1]. Although the occurrence of all types of EM wave are mainly due to accelerating charges, the canonical source of radiation for different regions of spectrum can be differentiated from each other in a practical sense such as follows; for instance, the source for radio frequency can be simplified to periodic currents of electric charges, microwave is generated by electron tubes using the motion of high speed electrons, visible spectrum is generated by molecular excitation, such as, the heat is related to kinetic energy of random motion of particles and due to this randomness it has a quite wide spectrum. We have to be aware of the fact that heat can also be transferred by convection mechanism which includes material displacement and conduction mechanism which includes direct contact of different materials. Heat can also be transferred through thermal radiation which does not need the material environment; i.e., it can propagate in vacuum since it is actually an EM wave.

1.1 Infrared Radiation

The thermal imaging refers to the ability that we can generate the image of a scene by detecting the thermal radiation entirely emitted by the objects in the scene, while

there are no any artificial or natural light sources in the environment except for the object itself. There are two essential ideas we exploit here to realize the IR technology at all. The first one is related to the source of the IR radiation, which can be anything having a temperature over 0 K and the second is related to the mediator between the IR source and the IR detector; i.e., atmosphere. First, all objects are composed of vibrating charged particles and these vibrating charged particles generates EM waves, capable of emitting waves in the thermal radiation range, whose spectral distribution (M(λ)) is mainly determined by the temperature (T) and the spectral emissivity of the object (ε(λ)), Equation (1).

$$M(\lambda) = \frac{2\pi hc^2 \varepsilon(\lambda)}{\lambda^5}\left[e^{\frac{hc}{\lambda kT}} - 1\right]^{-1} \quad W/(cm^2 \mu m) \qquad (1)$$

Where λ is the wavelength, c is the speed of light, k is the Boltzmann constant, h is the Planck's constant, T is the temperature and ε (λ) is the spectral emissivity of the object.

Emissivity of an object is related to its effectiveness in emitting its energy as the thermal radiation. The value of emissivity for an object is determined by measuring its spectral distribution with respect to a blackbody's spectral distribution. A blackbody is considered as the perfect emitter and a perfect emitter has an emissivity value of unity. Figure 1.1 shows the thermal radiation spectral distribution of a blackbody. A room temperature material (T=300K) has its maximum spectral distribution value around 10μm wavelength, such as humans. A higher temperature material such as jet engines has the maximum value around 3μm wavelength. For even hotter materials the wavelength is so short you can observe them in the visible region. What IR detectors do is to detect the thermal radiation signals at specific wavelengths for specific materials at specific temperatures. They create a 2D temperature distribution of the scene under observation, and we differentiate the objects in the scene from these temperature differences they create.

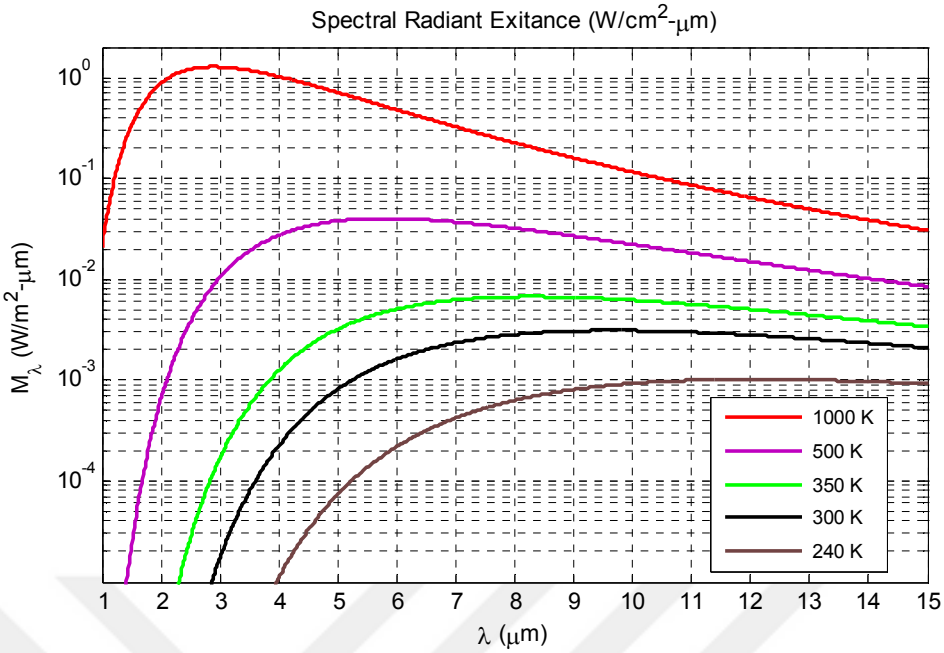

Figure 1.1: Spectral distribution of thermal radiation for various temperature values assuming emissivity of unity for all wavelength range. As the temperature increases the maximum loci of the distribution shifts to the lower wavelength values.

As we discussed in the beginning of this part, there are two essential considerations to realize the IR detection technologies. So far, we have described the source related one and the second is the mediator related one, which is actually IR transparency characteristics of the atmosphere, [2]–[4]. The IR detection is, in general, done over some length through the atmosphere. For the IR radiation through the atmosphere, either the scattering or the absorption mechanism may work to prevent an efficient transfer of the radiation, which might be quite problematic. Most of the gas molecules, the smoke and light mist particles are negligibly small in size when compared to the IR radiation wavelengths, thus the scattering mechanism is less likely to degrade the IR transmission efficiency through the atmosphere. However, specific absorption bands of the water, carbon dioxide and oxygen molecules affect the transmission efficiency severely. Figure 1.2 shows a generic IR transmission efficiency of the atmosphere.

The existence of various IR detector types with respect to the spectral usage such as Short Wave IR (SWIR), Mid Wave IR (MWIR) and Long Wave IR (LWIR) is directly related to these atmospheric windows. After getting the basics about what IR

radiation is, we will continue with the basic types of IR technologies used now with the next part.

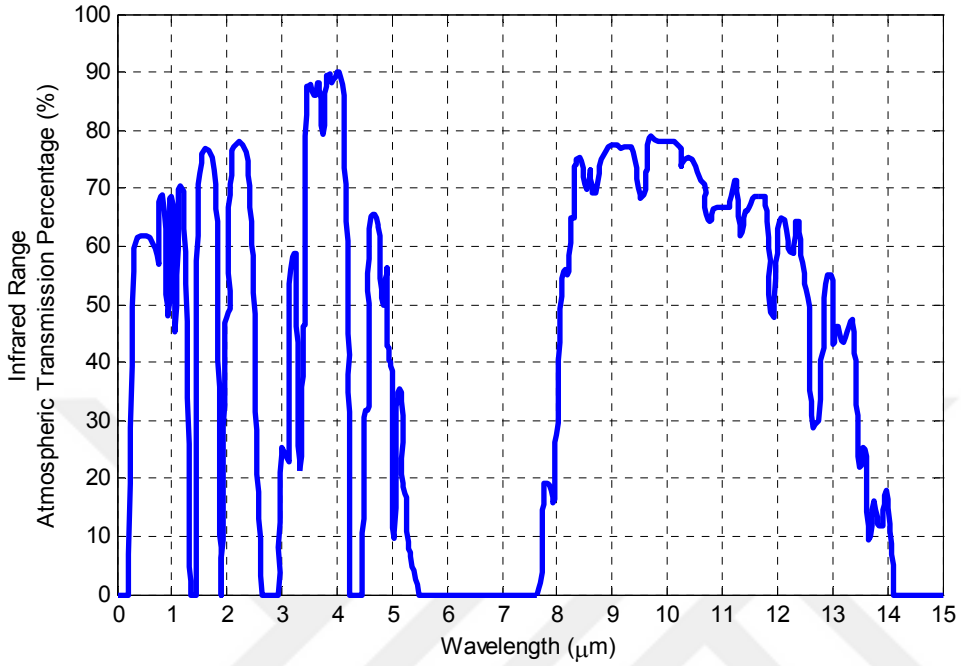

Figure 1.2: Transmission of the atmosphere for a 6000 ft. horizontal path over the sea level with a precipitation of 17mm, [5]. *This is a generic plot of IR characteristics of the atmosphere; the dips in the transmission graph are due to the naturally existing absorbing molecules such as CO_2 and H_2O in the atmosphere. The graph shows the various IR windows which can be exploited to transmit the IR radiation with minimum loss. These windows are directly related to evolution of the various range IR technologies such as Mid Wave IR (MWIR) exploiting the (3-5) μm window and Long Wave IR (LWIR) exploiting the (8-12) μm window.*

1.2 A Brief History Regarding the Evolution of the Infrared Detection Technology

Infrared radiation is known for merely about 200 years. It all began with the experiment of Frederick William Herschel. He studied the energy spectrum of sunlight with a prism, by deflecting each color onto different thermometers which are blackened to absorb sunlight efficiently, [6]. By measuring the temperature of each color, distribution of energy in sunlight is revealed and the highest temperature was just beyond the red color (infra-red). The next important step comes from Johann Seebeck. He discovered that an electric current can be induced between two

dissimilar metals heated when their junctions are kept at different temperatures, [7], which also alleviates the temperature sensitivity problem encountered with the Herschel's study. Still the induced current was seen as quite low until Leopoldo Nobili constructed the first thermopile. Interestingly, the first working examples of IR detectors were all thermal based, not photon based which dominates the military grade IR detectors. When it comes to photon detectors, as the other leading technology in the area, the technology evolved quite fast especially with the effect of the World War II, while the advancements in the thermal detector area were quite dormant until the second evolution of the technology in 1970s. The first photoconductive effect, as the ancestor of photon based detectors, is observed by Willoughby Smith while experimenting with the Selenium as an insulator for the submarine cables, [8]. Lead Sulphide was the first photoconductive material exploited in the application of the IR detectors during the World War II. After the transistor revolution, photoconductive materials with impurities found wide range application in the area. Germanium based detectors are known to be the first high performance of this kind. Shortly after, much narrower bandgap semiconductor materials and alloys are introduced to improve the wavelength selectivity and sensitivity such as InSb, InAsSb and HgCdTe, [2], [9].

Within the time interval when the two IR detector technologies exist, the photoconductive based detectors (Photon Detectors) were dominant in the field since the general perception about the thermal detectors were that they are slow, bulky, and less sensitive. However, the photon detector also needed the cryogenic cooling to beat the thermal generation noise directly related to thermally excited carriers, also this type of detectors were also bulky due to this cryogenic cooling unit. In 1970s some US research programs started to develop uncooled IR detector for practical military applications. Two initiatives Texas instruments and Honeywell focused on the issue, Texas instruments developed ferroelectric materials, such as Barium Strontium Titanate (BST) whose dielectric properties change with the temperature while Honeywell developed the vanadium oxide (VO_x) material whose conductivity changes with the temperature. Eventually VO_x and amorphous silicon (a-Si) became the widely used materials with the microbolometers while the microbolometers dominate the uncooled IR detector market with a 90% rate, [2]–[4].

1.3 Infrared Detection Technologies

The IR detection is done through either photon based (Cooled) detectors or thermal based (Uncooled) detectors depending on the application requirements when we examine the commercially available IR detectors in the market. As we have discussed in the previous chapter, for a long time the thermal detectors have been considered to be rather slow and insensitive in comparison with the photon detectors, thus exploited less in commercial and military systems in comparison with the photon detectors. However, in the last two decades it has been shown that extremely good imagery can be obtained from large thermal detector arrays of pixels operating uncooled at TV frame rates (30Hz). The speed of thermal detectors is found to be quite good enough for non-scanned imagers with two-dimensional (2D) detectors. This evolved into usage of FPAs (Focal Plane Arrays; i.e., 2D staring arrays of detector pixels) with the thermal detectors resulting in a moderate sensitivity of the thermal detectors. Up to now the evolution of the uncooled IR detectors are described from a technological point of view. From marketing point of view, we could say that the evolution of infrared (IR) imaging sensor technology for defense market has paved the way for developing civil applications market. The technologies of both pixel size reduction and vacuum package have transcended the usage of uncooled Long-Wave IR (LWIR; 8-14 μm wavelength range) imaging sensor into the civil market. The uncooled LWIR market can be divided into two areas; one is the high-end market where the performance of the uncooled LWIR sensors are aimed to be as close as to the cooled counterparts, while the other one is the low-end market in which the device miniaturization and the reduction in price is more desirable than the high performance.

In general, an IRFPA (Infrared FPA) consists of two parts, the infrared sensitive one does the sensing part and the Read-Out Integrated Circuit (ROIC) one does the interpretation part. What ROIC does is to address the pixels sequentially and get a reading related to a voltage or current change from each of them in response to the output of the sensing part and do some form of signal processing, such as, amplification, signal integration, and multiplexing. FPAs can be classified as either “hybrid” or “monolithic” with respect to the merging configuration of the sensor and

the ROIC parts. Hybrid type consists of two parts made separately, which are later mechanically and electrically connected to each other; such as it happens with the flip-chip bonding. With monolithic arrays, the detecting part is deposited as a thin film on the silicon substrate containing the ROIC. The trend is strongly towards to the monolithic construction for reasons of performance, strength, and cost, [1], [3].

1.3.1 Photon Based IR Technology

For the photon based detectors, the detection is done through the interaction of the photons as the radiation particles with the electrons of the detecting material. This material is generally a semiconductor device whose IR spectral response range is determined by either its forbidden energy gap or the ionization energies of the injected donors or acceptors, Equation (2).

$$E_{gap}(eV) = \frac{1.24}{\lambda\ (\mu m)} \qquad (2)$$

For instance, for MWIR range (3 μm-5 μm), the forbidden energy gap must be around 0.31eV and for a LWIR range (8μm-12 μm), this energy should be around 0.12 eV.

Through the photon-electron interaction, the electron density; i.e., charge carrier density in the conduction band is disturbed. These photo-excited carriers change the current and in return, the discretization of this change is interpreted as the image. However, for this type of detectors the charge carrier density is not only disturbed by the photon exposure. For bandgap devices, there is always a thermal agitation factor which degrades the sensitivity of the photon based detectors. The effect of the thermally excited carriers is alleviated through the cryogenic cooling, cooling around 77K. However, the cryogenic cooling unit, in turn, makes the detector big, bulky and expensive while beating the effects of the thermal agitation. An important feature of the photon detectors, since the transition is electronic, a photon detector is a fast response device.

1.3.2 Thermal Based IR Technology

Thermal based detection relies on the exploitation of a measurable quantity of a very special material which is quite responsive to small changes in the temperature due to IR absorption, such as; conductivity, dielectric properties and polarization of the material. This special material is called as the active part of the detector; i.e., the part mostly affected by the temperature variations. In the past several years, a remarkable progress has been made in uncooled infrared focal plane arrays (IRFPAs). Two marketable directions are promoted with this technology. The first is to produce high performance IR cameras to compete and even replace photon detectors and the second is for low cost or ultra-small IR cameras which can produce new markets for IR camera usage. A nice example of this would be the application of the low cost technology in driver's vision enhancement system.

1.3.2.1 Figure of Merits for Thermal Based IR Detectors

Evaluation of the performance of thermal based IR detectors actually means to analyze the performance parameters of IRFPAs which accounts for both the sensor part and the ROIC part of the FPAs as a whole. For instance, while the thermal conductivity or thermal response time is mostly related to the sensor part, the NETD involves not only the sensor array but also the optics and the ROIC part.

Although there are many parameters to be analyzed, the most interest relies on the analysis of the thermal sensitivity, responsivity, noise equivalent temperature difference, thermal conductivity and thermal response time parameters. These performance parameters may also be considered as the characterization parameters in the development process. While developing a specific FPA technology, we first create both the single pixels and array of pixels on the same blank wafer, the wafer without the CMOS ROIC, relieving the R&D cost. Single pixels are manufactured to observe the specific performance parameters such as responsivity, thermal conductance and thermal response time through which we can get a rough estimation for the NETD before the realization of the CMOS backed pixels, while the array is manufactured for only the process optimization goals.

1.3.2.1.1 Temperature Sensitivity

In previous sections, we have mentioned that the thermal detectors are based on the exploitation of the temperature dependency of some measurable quantity of a specific material. Thus the temperature sensitivity is one of the prime concerns for the performance parameters for these types of detectors in question. The higher the sensitivity, the better the performance is. For various realizations of the thermal detectors, the sensitivity description changes as well. For resistor type bolometers, the parameter, called as the Temperature Coefficient of Resistance (TCR) is used as a measure of temperature dependency of the Thin Film Resistors (TFRs). The TFRs are produced by depositing the active material over the electrode structures. For the diode type bolometers, while the temperature dependency of forward bias voltage of a diode is correlated to the temperature variations, for thermoelectric type ones, the Seebeck Coefficient sets the measure of this very same type of relation.

Equation (3) gives the description of the TCR value for resistor type bolometers, where *R (T)* describes the temperature variation of the resistance value over some range around the room temperature, *T* is the temperature. Both metals and semiconductors have high enough TCR values, however semiconductors are more dominantly used since they present higher values than the metals do, [10]. In general, while the semiconductor based resistors have negative TCR values, the metals have positive TCR values. For a negative TCR material, as the temperature gets higher the resistance value, exposed to this temperature change, gets lower.

$$TCR = \frac{1}{R(T)}\frac{\partial R(T)}{\partial T} \ (1/K) \qquad (3)$$

For semiconductor type materials, the TCR value is also closely related to the bandgap energy of the material also called as the activation energy (E_a). Equation (4), called as the Arrhenius Relation, [11] explains for this relation, where k is the Boltzmann constant. Equation (5) gives the simplified TCR expression for the semiconductor materials with the assumption that the activation energy is a slowly

varying function of the temperature over the given temperature range in question, [11], [12].

$$R(T) = R_0 e^{\frac{E_a}{kT}} \ (\Omega) \qquad (4)$$

$$TCR = -\frac{E_a}{kT^2} \ (1/K) \qquad (5)$$

Figure 1.3 shows a generic characterization of the temperature sensitivity of a TFR produced at METU MEMS Center. For the characterization, we first measure the resistance variation over the temperature change of the specific TRF in a temperature controlled environment. Then by using the fitting tools we obtain the activation energy of the resistor structure then we can calculate the TCR value. We try to increase this value in magnitude by optimizing the deposition conditions of both the active material and the electrodes.

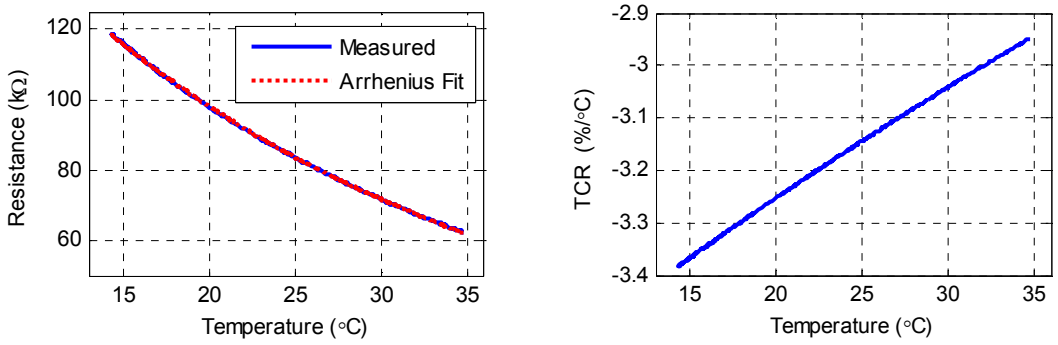

(a) Resistance vs. Temperature graph.

(b) TCR vs. Temperature graph.

Figure 1.3: The graph of the measured Resistance vs. Temperature (R-T) change (a) and the graph of the calculated TCR vs. Temperature change (b) of a specific Thin Film Resistor (TFR) produced at METU MEMS Center are shown. The R-T graph is obtained by simultaneously observing the resistance change and the temperature change of the TFR, while it is placed into a temperature controlled oven. The TCR is calculated by fitting the measured R-T data into the Arrhenius relation by using a two dimensional fitting algorithm and finding the activation energy (E_a) in return. While the fitted value of E_a for this specific sample is found to be 0.22eV, the calculated TCR value is to be around -2.9%/˚C @25˚C in accordance with.

However it is not that simple, for most active materials used in TFR production, when you try to increase the TCR value, the resistivity of the material also increases, in turn the noise level of the resistor increases which is not desirable at all. Thus, the optimization of a TFR is actually a trade-off between the TCR value and the noise level it introduces, [13].

For diode type bolometers, the temperature sensitive quantity is the applied forward bias voltage. Equation (6) shows the generic I-V characteristics of a diode, where I_d is the diode current, V_f is the forward bias voltage of the diode, I_s is the reverse saturation current, k is the Boltzmann constant, q is the unit charge of an electron, T is the temperature and n is the ideality factor which explains for the difference between the practical and theoretical I-V characteristics of a diode, [14]–[16].

$$I_d = I_s\left(e^{\frac{V_f}{nkT/q}} - 1\right) \ (Ampere) \qquad (6)$$

Equation (7) shows the sensitivity description for the diode type bolometers, where m is a constant in some range, E_g explains for the bandgap energy of the silicon, which can be taken as 1.12 eV. This relation can be simplified to Equation (8), around room temperature and with an ideality factor of unity, where p is the number of serially connected diodes. We should remember that SOI diodes have this advantage over standard CMOS diodes to be produced in multiples to enhance the sensitivity, [14], [16], [17].

$$\frac{dV_f}{dT} = -\frac{mn\frac{kT}{q} + \frac{E_g}{q} - V_f}{T} \ (Volt/Kelvin) \qquad (7)$$

$$\frac{dV_f}{dT} = -p\frac{0.025m + 1.12 - V_f}{T} \ (Volt/Kelvin) \qquad (8)$$

1.3.2.1.2 Responsivity

Bolometers measure the temperature variations generated by the heat exchange with the surroundings and convert this into a measurable electrical quantity such as a voltage or current. This measurable electrical quantity is transferred to the ROIC part for further processing. The magnitude of this transferred quantity for a given heat flow is characterized by the responsivity parameter. Before we learn how to make sense of the responsivity parameter, first we need to solve the related heat flow equation and then we need to understand the measurement procedure, finally we will make some observations. Figure 1.4 shows the simplified thermal circuit model through which we will derive the related heat flow equation. This model simply tells us that the incident IR power (P_0, *Watts*) is absorbed with some efficiency (η) by the absorber part of the detector pixel. This absorber part is thermally insulated from the ROIC part, to enable the thermally active part benefit from the generated heat efficiently. The measure of this isolation is characterized with the detector-characteristic thermal conductance (G_{th}, *Watts/Kelvin*) parameter. The heat change over the thermally isolated part, i.e., the thermally active part, does not happen instantaneously, it needs some time to bring the mass of the isolated part to its final temperature. The thermal mass is characterized by the (C_{th}, *Joules/Kelvin*) parameter which is also a detector-characteristic parameter. The detector-characteristic transient time to bring the temperature of the thermal mass to its final value is characterized with the thermal time constant (τ_{th}, *seconds*) parameter, which is actually (C_{th}/G_{th}) in value. ΔT represents the steady state temperature difference over the thermally active part which will be interpreted as the electrical signal eventually, due to the absorbed incident IR power (P_0). It is assumed that the model is linear; i.e., there is no Joule heating accounted for with this model. When the detector is biased, due to resistive elements there will already be some temperature rise, other than the one spawned by the coupled infrared power. This is called Joule heating and it is not something desirable. To understand what (ω, *Hertz*) represents in the model; the measurement set-up should be examined.

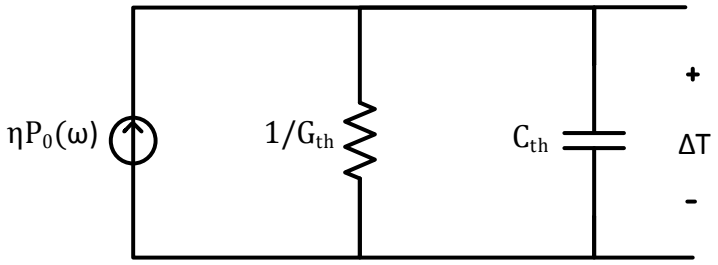

Figure 1.4: Simplified thermal circuit representation for a generic thermal detector, representing the dynamic temperature response of the detector. The model incorporates the thermal isolation concept into the equation through a detector specific thermal conductance, G_{th}, parameter, the thermal mass of the thermally isolated part, with a detector specific thermal capacitance, C_{th}, parameter and the quantity of the infrared power exposure with a generic source power, P_0, parameter.

Figure 1.5 shows a generic setup for the responsivity measurements. At METU-MEMS Center, during the development course, we make measurements for single pixels instead of pixel arrays to lower the Research and Development (R&D) cost by not using CMOS backed wafers. An indirect method derived from the dynamic heat flow equation, Equation (9) suggests finding a frequency response representation, [1], [18]. While the DC ($\omega=0$) value of this derived frequency response gives the responsivity value, we can also obtain the time constant of the detector pixel by forcing the measurement data into the derived frequency response, Equation (12), with the help of a two dimensional fitting algorithm.

The adjustable infrared (IR) power is generated by the Blackbody source. The generated IR signal is modulated with a chopper wheel whose frequency (ω) is adjusted by the controller unit to separate the generated IR signal from the background IR signals. The modulated IR signal is incident upon the single pixel; i.e., Device under Test (DUT), to be tested. The single pixel is placed in vacuum environment (DEWAR) to prevent the heat flow into the ROIC via air molecules. Due to modulated IR signal, we can read a voltage output at the chopper frequency, if we bias the pixel with a current source and examine the frequency characteristics of the output voltage with the help of a lock-in amplifier or a Digital Signal Analyzer (DSA). The maximum signal output at the chopper frequency is collected by the

computer, and the data is fitted into a specific equation, Equation (12), to determine the responsivity and the thermal time constant simultaneously.

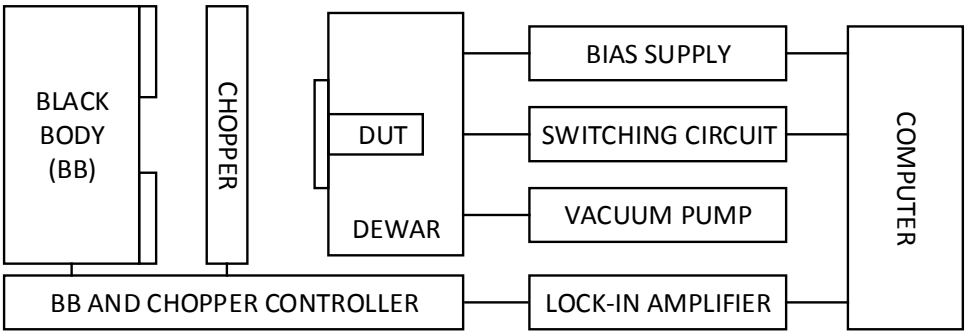

Figure 1.5: The block diagram of a generic responsivity measurement setup, [18]. *The adjustable infrared (IR) power is generated by the Blackbody source. The generated IR signal is incident upon the single pixel (Device Under Test, DUT) to be tested. The single pixel is placed in vacuum environment (DEWAR). A voltage output at each chopper frequency can be read, if a current bias is applied. Examining the frequency characteristics of the output voltage, both the responsivity and the thermal time constant can be determined simultaneously.*

By following the successive derivations from Equation (9) to (12), the meaning and the usefulness of the ω parameter is obvious which is actually related to the chopper frequency.

$$C_{th}\frac{d(\Delta T)}{dt} + G_{th}(\Delta T) = \eta P_0 e^{jwt} \qquad (9)$$

$$\Delta T = \frac{\eta P_0}{G_{th}\sqrt{1 + \left(w\frac{C_{th}}{G_{th}}\right)^2}} \qquad (10)$$

$$R = \frac{\Delta V_{out}}{P_0} = \frac{\eta(\Delta V_{out}/\Delta T)}{G_{th}\sqrt{1 + (w\tau_{th})^2}} \qquad (11)$$

$$R = \frac{R_{DC}}{\sqrt{1 + (w\tau_{th})^2}} \qquad (12)$$

Figure 1.6 shows the measured and fitted data to obtain the responsivity parameter for a generic high performance pixel produced at METU MEMS Center. The raw measured data is actually the output voltage of the single pixel in rms (root-mean-square) at swept chopper frequencies. The ratio of the voltage output to the absorbed IR power is defined as the responsivity

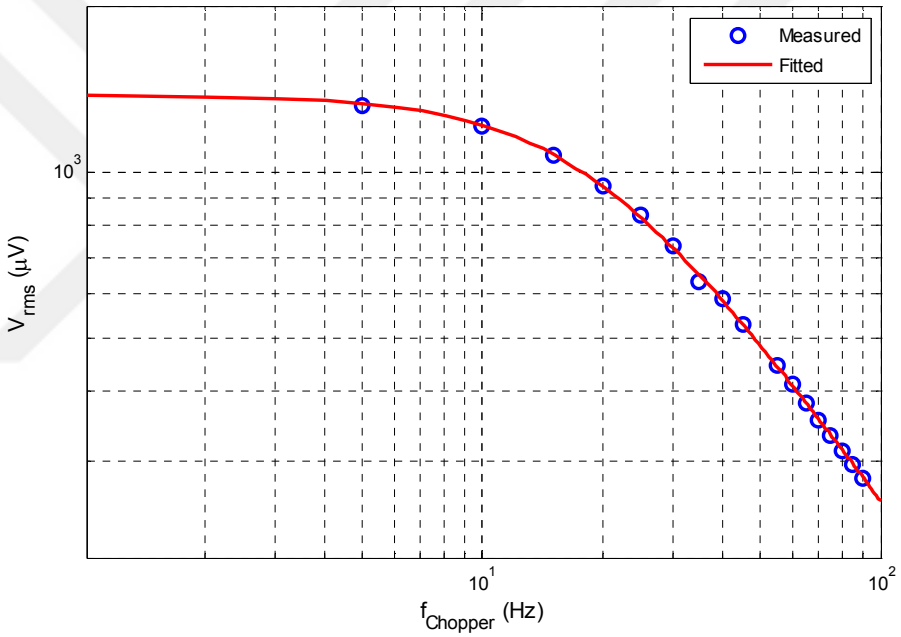

Figure 1.6: The graph of the measured and the fitted generated voltage obtained from a generic resistor type single pixel detector produced at METU MEMS Center. By dividing the generated voltage value by the absorbed incident IR power, the responsivity parameter is obtained. For this specific example, the fitted DC voltage is found to be 1377μ-Volts (μV) and the time constant to be 8.5 milliseconds (msec).

Another important performance parameter, which is already implicitly employed in the formulation of both the responsivity and the thermal time constant, is the thermal conductance (G_{th}). This parameter is a measure of the thermal isolation of the sensing part of the detector from the ROIC part. For the extraction of these parameters of a resistor type bolometer, first the I-V characteristics is observed for the resistor placed

on the single pixel at room temperature (normally 300 K, i.e., the room temperature). This characteristic deviates from the ohmic behavior due to self-heating effects. The experiment is done in a vacuum environment (DEWAR), and under Joule heating assumption, there is no IR radiation exposure, the pixel is blind in this sense. Thus the only heat comes from the self-heating effects due to Joule heating. Equation (13) shows the generated heat from the dissipated electrical energy, where T_0 is the temperature of the body which is holding the thermally isolated part up in the air with some supporting legs. R_e is the electrical resistance and i_b is the bias current.

A part of this heat is conducted through the supporting legs and a very small part of it is radiated into the surrounding atmosphere, and the remaining heat increases the bolometer temperature, and hence decreases the value of the resistor placed on the single pixel. Assuming that the heat conduction through supporting legs is the dominant heat loss mechanism, then we can obtain Equation (14) by incorporating the *TCR* parameter into the equation, [10], [18]–[21]. R_e is the collected electrical resistance data under vacuum condition while sweeping the bias current, i_b. R_{e0} is the electrical resistance value under atmospheric pressure. We bias the resistors placed over the single pixels with a current source and measure the voltage output. TCR is an already extracted parameter with another measurement setup, i.e., we already knows its value. The slope of Equation (14) gives the thermal conductance parameter.

$$i_b^2 R_e = G_{th}(T - T_0) \qquad (13)$$

$$\frac{1}{R_e} = \frac{1}{R_{e0}} - \frac{TCR}{G_{th}} i_b^2 \qquad (14)$$

1.3.2.1.3 Noise Equivalent Temperature Difference

Noise Equivalent Temperature Difference (NETD) is the most common metric for bolometer performance in uncooled sensors, which expresses for the sensitivity of the microbolometer, [1], [18], [22]. NETD is the difference in the temperatures of objects in a scene, which will produce a signal-to-noise ratio of unity. It accounts for the minimum signal level which is comparable to the overall noise level of the

imaging system. The overall noise level is composed of various noise components such as; Flicker (1/f) noise, Johnson noise and ROIC noise, Equation (15), [23]. The exact source of 1/f noise is not known, but there are some observations/theories about its characteristics that have been made, Hooge's Law, [24], [25]. One of the theories suggests that the traps and defects within the active material are the sources for this kind of noise. The Flicker noise is dependent on temporal frequency and is the major source of noise for resistor type of bolometers. Johnson noise exists in all types of resistors and independent of temporal frequency distribution. The thermal fluctuation noise is due to random heat exchange between the bolometer and its environment. It is independent of the temporal frequency distribution. The thermal fluctuation noise is the fundamental limit on microbolometer performance; i.e., if other noise sources are somehow eliminated or made negligible, thermal fluctuation noise will still exist.

$$NETD_{Overall}^2 = NETD_{1/f}^2 + NETD_{Johnson}^2 + NETD_{Thermal}^2 + NETD_{ROIC}^2 \qquad (15)$$

Equation (16) shows a generic formulation of the NETD incorporating several performance parameters which we have already analyzed.

$$NETD_{Overall} = \frac{(4(f/\#)^2 + 1)V_{Noise-Overall}}{R\Gamma A_d(\Delta P/\Delta T)_{\lambda_1,\lambda_2}}\ (K) \qquad (16)$$

Where ($f/\#$) is the focal ratio of the optics, Γ is the transmittance of the optics, R is the responsivity, $V_{Noise\text{-}Overall}$ is the total noise voltage within the frequency band determined by the ROIC part, and $(\Delta P/\Delta T)_{\lambda 1, \lambda 2}$ is the change in power per unit area radiated by a scene at temperature T within the IR spectral band (λ_1, λ_2). The lower the NETD value, the better the performance is.

1.3.2.2 Resistor Type Microbolometer

The material quantity which is responsive to the temperature variations for the resistive bolometers is the conductivity of the material. With resistors produced from

this material and biased with a current source, the voltage variations due to temperature changes can map the temperature distribution of a scene under observation. As the temperature rises on the active part, the resistance value of the resistor structure constructed from the active material will rise or fall. If it is a metallic material, the resistance will increase as the temperature increases, we call it a positive TCR (Temperature Coefficient of Resistance) material and if it is a semiconductor based material as the temperature increases the resistance value will decrease and we call it a negative TCR material. This temperature active part is suspended from the structure it is constructed on, which is mostly a CMOS ROIC wafer, to provide thermal isolation and to prevent the heat sink effect of the ROIC, [1], [2].

There are several resistive active materials reported with high TCR values in the literature, such as Vanadium Oxide (VO_x), [19], [23], [26]–[28], amorphous Silicon (a-Si), [29]–[31] , Yttrium Barium Copper Oxide (YBCO), all actively used with the detectors in the market with various companies like FLIR, DRS, Figure 1.7, Ulis, LETI, Raytheon.

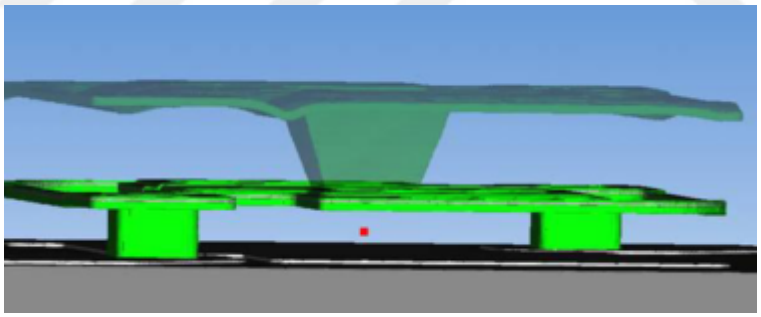

(a) Cross section view of schematic representation for resistor based bolometer pixel with umbrella structure produced by DRS, Figure 1.7 (continued).

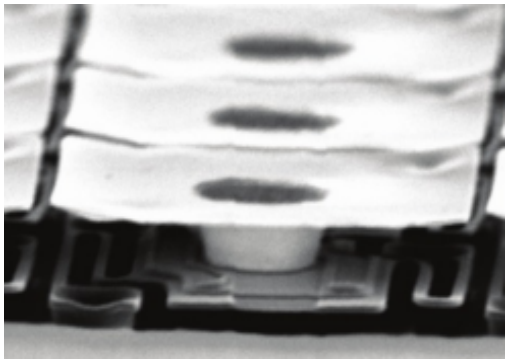

(b) Scanning Electron Microscope (SEM) image of 17 µm pitch uncooled FPA pixels produced by DRS.



(c) IR image obtained from a 640x480, 17 µm pitch uncooled FPA, (DRS U6160 Model).

Figure 1.7: The Scanning Electron Microscope (SEM) image (a) and IR image (b) obtained from DRS U6160 Model 640x480 IRFPA. This model has a pixel pitch of 17µm, working in LWIR range (8-14)µm, has an NETD of less than 40mK @ f/1.0 optics, and a time constant of less than 14msec,[28], [32], [33], [34].

At METU MEMS Center, the resistive active material studies starts with the employment of CMOS n-well layer as the infrared sensing part using a commercial 0.8µm CMOS process line. The n-well is suspended by bulk-micromachining of the fabricated CMOS dies for thermal isolation purposes. Since this approach does not require any lithography or high TCR material deposition after the CMOS fabrication, has actually resulted in the ultra-low cost trials. Nevertheless, these studies have also continued with relatively high performance versions which include the high TCR material deposition after the CMOS fabrication. The n-well has a TCR of 0.5–0.7%/K, relatively low compared to special high TCR materials; however, it also presents negligible noise due to its single crystal structure. With this study, a 16X16 prototype FPA with 80µm pixel pitch size and 13% fill factor with an NETD of 200mK is implemented, [35]. Next, a high performance type of 320X240 size FPA with a pixel pitch of 50µm is realized with surface-micromachining techniques, not bulk-micromachining, [36], Figure 1.8. Within the scope of this study, the high TCR material is preferred as YBCO with a measured TCR of -3.4 %/K. A fill factor of 64% and an expected NETD of 50mK (measured as 450mK) is also obtained, Another study at METUMEMS has increased the fill factor to 92% with single pixel measurements with an expected NETD of 36mK for an 640X320 FPA, [37].

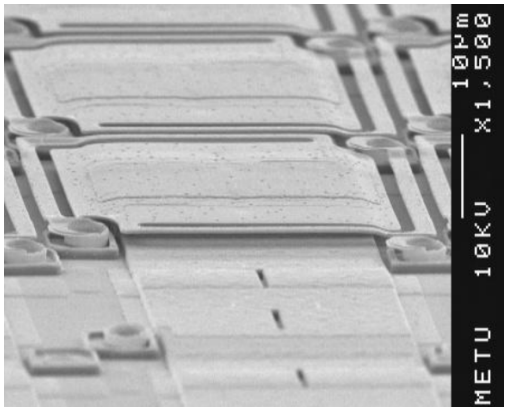

(a) SEM image of 50μm pitch uncooled FPA pixels produced by METU MEMS Center.



(b) IR image obtained from a 320X240, 50μm pitch uncooled FPA produced by METU MEMS Center.

Figure 1.8: The SEM image (a) and IR image (b) obtained from 320X240 IRFPA produced by METU MEMS Center. The FPA has a pixel pitch of 50μm, working in LWIR range (8-14)μm, has a measured NETD of around 450mK @ f/1.0 optics, and a time constant of around 15msec,[36].

1.3.2.3 Diode Type Microbolometer

Diode based microbolometers exploit the temperature sensitivity of p-n diodes. As the temperature of the diode is increased with the help of a deposited absorber layer the forward bias voltage of the diode changes, and this can be used to extract the temperature map of a scene. These types of bolometers are considered to be suitable for low-cost applications, thus expected to be also suitable for monolithic integration and CMOS compatibility. Basically there are two featured types reported in the literature. One of them involves a suspended single p-n diode, however this type is reported to have problems with the implementation of large format FPAs due to large pixel size and large thermal time constant, [38], [39]. The other type uses suspended multiple series diodes implemented in a SOI (Silicon-on-Insulator) CMOS process, first introduced as in the form of 320X240 FPA with 40μm pixel pitch size and an NETD of 120mK (f/1.0) by the Mitsubishi, [40]. The SOI diode based detectors has other favorable characteristics other than being low-cost; such as, due to good crystal quality of SOI films, there are fewer defects, and thus the Flicker noise caused by defects is less than that of amorphous or polycrystalline materials. Another advantage is reported as the excellent uniformity of the electrical characteristics and their thermal dependence. Up to now, several array formats of 640X480, Figure 1.9,

320X240 and 160X120 for the SOI diode IRFPAs are reported for both with 25μm and 17μm pixel pitches, [40]–[42]. For 25μm pixel pitch 640X480 IRFPA, a noise equivalent temperature difference (NETD) of 21mK (f/1.0, 30Hz) and a thermal time constant (τ_{th}) of 16msec with excellent uniformity is also reported in another study, [43] .

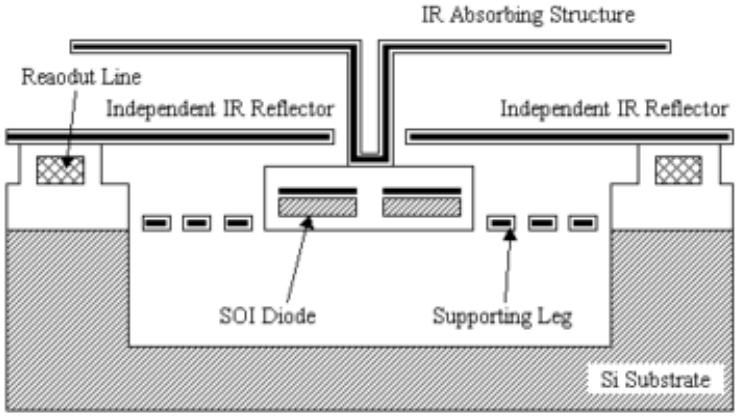

(a) Cross section view of schematic representation for SOI diode based bolometer pixel produced by Mitsubishi.

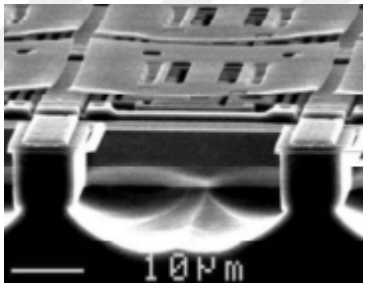

(b) SEM image of 25 μm pitch, SOI diode based uncooled FPA pixels produced by Mitsubishi.



(c) IR image obtained from a 640X480, 25μm pitch uncooled FPA produced by Mitsubishi.

Figure 1.9: The cross sectional schematic representation (a), SEM image (b) and IR image (c) obtained from 640X480 IRFPA based on SOI diodes, produced by Mitsubishi. The FPA has a pixel pitch of 25μm, working in LWIR range (8-14) μm and has a measured NETD of around 40mK @ f/1.0 optics, [41].

At METU MEMS Center, the low cost studies start with the successful implementation of a 16X16 prototype FPA employing suspended CMOS n-well layers belonging to a standard 0.8μm CMOS process line. Then, the previous study is extended to both 64X64 and 128X128 format, as shown in Figure 1.10, FPAs with a pixel pitch of 40μm and a fill factor of 44% with an NETD of around 500mK

(f/1.0, 30 Hz). The thermally active parts are implemented with suspended and thermally isolated p+-active/n-well diodes by using a standard 0.35 µm CMOS process line, [44]–[46].

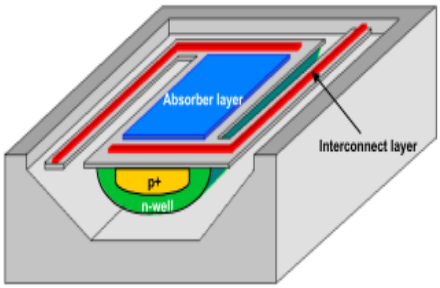

(a) An oblique view of schematic representation for p+-active/n-well diode based bolometer pixel produced by METU MEMS Center.

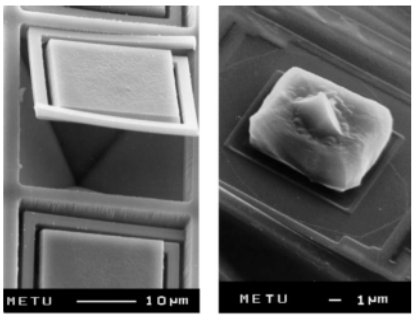

(b) SEM image of 40 µm pitch, p+-active/n-well diode based uncooled FPA pixels produced by METU MEMS Center.

Figure 1.10: The oblique view of schematic representation (a) and SEM image obtained from 128X128 IRFPA based on p+-active/n-well diode, produced by METU MEMS Center. The FPA has a pixel pitch of 40µm, working in LWIR range (8-14)µm and has a measured NETD of around 1000mK @ f/1.0 optics with a time constant around 36msec, [46].

The low cost studies continued with the successful realization of 64X64 FPA based on p-diffusion/n-well SOI diode with a pixel pitch of 70µm and an expected NETD of 498mK, [14]. The shift from standard CMOS to SOI-CMOS is mainly due to the fact that SOI-CMOS technology enables the employment of the usage of multiple diodes to promote the sensitivity of the detectors. Figure 1.11 shows the realization of a 128X128 FPA with the SOI employment, with a pixel pitch of 70µm and a measured NETD of 1110mK, [16].

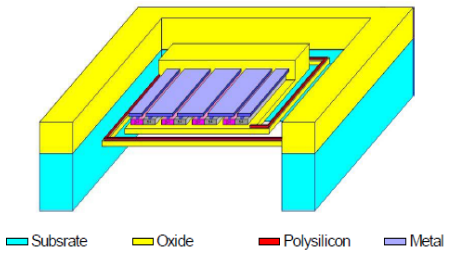

(a) An oblique view of schematic representation for p+-active/n-well SOI diode based bolometer pixel produced by METU MEMS Center. SOI technology is able to employ multiple diodes to increase the sensitivity, Figure 1.11 (continued).

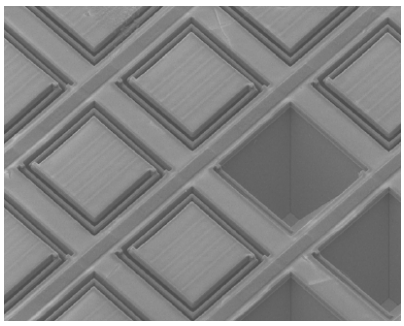

(b) SEM image of 70 µm pitch, p+-active/n-well SOI diode based uncooled FPA pixels produced by METU MEMS Center.



(c) IR image obtained from a 128X128, 70 µm pitch SOI based uncooled FPA produced by METU MEMS Center.

Figure 1.11: The oblique view of schematic representation (a), SEM image (b) and IR image (c) obtained from 128X128 IRFPA based on p+-active/n-well SOI diode, produced by METU MEMS Center. The FPA has a pixel pitch of 70µm, working in LWIR range (8-14)µm and has a measured NETD of around 1100mK @ f/1.0 optics with a time constant around 46msec, [16].

The SOI based technology at METU MEMS Center kept going with the enhancement trials regarding a decrease in the NETD values, reduction in the pixel pitch size to 50µm, [17] and an increase in the absorption rate, [47]. The measured NETD values are set back to 280mK from higher values reported in [14], [16] by making revisions on the ROIC part of the chips for a 160X120 IRFPA. We should remember the fact that the unexpected noise performance of a sensor based chip can be either due to sensor part or the ROIC part. Secondly, within the framework of the studies conducted in the METU MEMS Center another success was the realization of a smaller pixel size of 50µm without any degradation in the performance. This is accomplished by employment of more serially connected diodes in the pixel bodies and thinner arm legs, [17]. The sensitivity of an SOI based sensor can be increased by implementing more serially connected diodes, which was the trick actually SOI technology was offering in the first place and standard CMOS diodes was not. Thinner arm lengths means to better thermal isolation, which in turn prevents the coupling of the generated thermal heat on the sensor part to the ROIC part more efficiently. Figure 1.12 shows the topology and the performance results for a 50µm pixel with the implementation of high fill factor structures to the SOI wafers at METU MEMS Center.

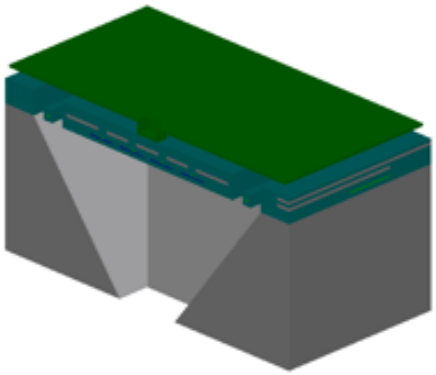

(a) An oblique view of schematic representation for p+-active/n-well SOI diode based bolometer pixel with umbrella structure produced by METU MEMS Center.

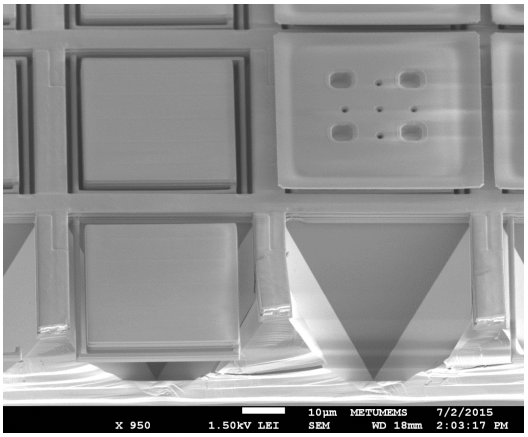

(b) SEM image of 50µm pitch, p+-active/n-well SOI diode based uncooled FPA pixels both with and without umbrella structures, produced by METU MEMS Center.

Figure 1.12: The oblique view of schematic representation, (a) and SEM image, (b) obtained from 160X120 IRFPA based on p+-active/n-well SOI diode, produced by METU MEMS Center. The FPA has a pixel pitch of 50µm, working in LWIR range (8-14) µm and has a measured NETD of around 280mK @ f/1.0 optics. Within the scope of this study, while the fill factor of the low-cost detector pixels with 50µm pitch is increased from 46% to 92%, the responsivity of the FPAs is increased by 30% with the implementation of the umbrella structures over the diode including bodies, [47].

1.3.2.4 Thermopile Type Microbolometer

Another physical effect that can be exploited for thermal sensing is the Seebeck Effect (Thermoelectric Effect) which assigns different materials with different Seebeck coefficients. If you join two different materials at two different joints, leave one joint hotter than the other one, insert a voltmeter between the two materials and you will observe an induced voltage, [7], [48], [49]. This induced voltage will be proportional to the temperature difference between the two joints and the difference between the Seebeck coefficients of the materials used to construct the structure. This structure is known as a thermocouple. Both metals and semiconductors exhibit thermoelectric properties, however, the Seebeck coefficients of semiconductors, in general much larger than those of metals, depending on the semiconductor and the sign and concentration of impurities within the semiconductor, [50]. Although the thermoelectric voltage read from a single junction is small, it is possible to construct many of them in series to get higher voltage readings and such a device is called a thermopile. The thermal mass of such structures must be very small to get fast

responses and the junctions must be thermally isolated very well to get higher responsivities, [50], [51], as it was with the resistive bolometers.

Today, micro-machined thermopiles are already commercialized in many different applications such as radiation temperature sensors and infrared gas detectors. Customer needs have grown in recent years due to many benefits of micro-machined thermopiles. For example, the self-generating nature of the thermopile output voltage makes the biasing unnecessary, these type of detectors do not need cooling, cooling stabilizer or modulation either which reduces the overall system complexity. Further advantages include insensitivity to vibrations and the lack of self-heating, long-term stability and continuous miniaturization due to CMOS IC compatibility, [52], [53]. All these features make thermopiles very attractive for ultra-low-cost applications with moderate responsivity and resolution although their low responsivity and large pixel sizes. In addition to the fore mentioned features, their broadband response and the wide operating temperature range make them also well suited for some space-based scientific imaging applications, [51], [54]. Figure 1.13 shows a sample of mass producible thermopiles.

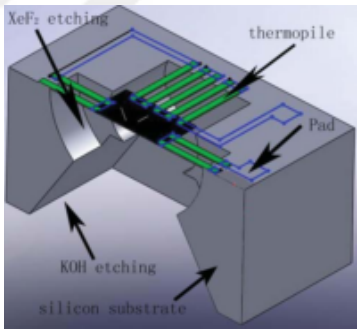

(a) Schematic view of a bulk micromachined thermopile, Figure 1.13 (continued).

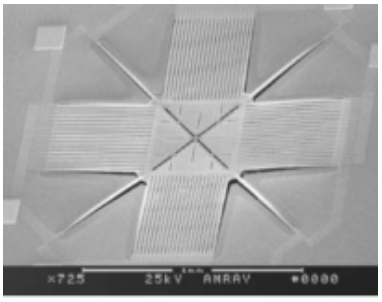

(b) SEM graph of top view of a bulk micro-machined thermopile.

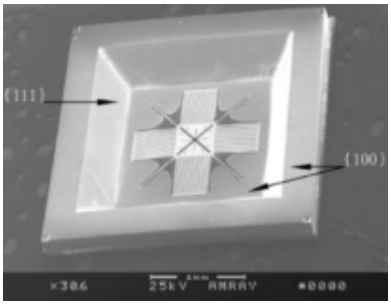

(c) SEM graph of bottom view of a bulk micro-machined thermopile.

Figure 1.13: The schematic view (a) and SEM graphs (b, c) of a simple mass producible uncooled thermoelectric infrared. . In air at room temperature, the sensor has a responsivity of 71.6V/W, noise equivalent power of 0.64nW/Hz$^{1/2}$, detectivity of 6.21×10^7cm. Hz$^{1/2}$/W and a time constant of 13.2msec, [55].

1.4 Absorption Enhancement for Uncooled IR Detectors

Bolometers absorb heat from the surroundings, transfer it to the temperature sensitive part of the detector, and the resulting temperature rise is employed to form the IR image of the surroundings. Thus to maximize the temperature sensitivity, i.e. temperature rise, all incident heat should be absorbed and employed to increase the temperature of the sensitive part. As the pixel dimensions get smaller, the total absorbed power by the absorber surface belonging to each pixel also decreases since the physical dimension of the each pixel gets smaller. The absorbed power is directly proportional to the size of the absorber surface. Another consequence of decreasing dimensions is that the suspending arm lengths also get shortened which makes the thermal isolation of the sensor part from the ROIC part much more difficult. Due to these reasons maximizing the absorption rate of the individual pixels within the respective IR range is vital. There are basically two ways to improve the IR absorption. First is to make sure that reflection, scattering or transmission mechanisms do not share any of the incident power, so that all incident EM power can be transduced into usable heat power; i.e., perfect absorption. The second method for absorption enhancement is to increase the absorption area directly, which means placing high fill factor individual pixels into the FPA, [47], [56]–[58].

Perfect absorber means that transmission, reflection, scattering (can be eliminated by creating less rough surfaces) mechanism and Surface Electromagnetic Waves (SEWs) are disabled for the interaction of EM waves with the material. There are mainly two types of absorbers; resonant and broadband types. The simplest way is to design multiple layers separated by a quarter of the operation wavelength; i.e., $\lambda_0/4$, backed by an Perfect Electric Conductor (PEC) layer and put an impedance layer of 377Ω, which is actually equal to free space wave impedance for impedance matching purposes, to the most front side. In Transmission Line Theory (TLT), quarter wavelength transmission lines act like an impedance transformer. PEC layer acts like a short circuit termination, which is transformed into open circuit termination, the open circuit which is parallel connected to the 377Ω load will match the free space wave impedance. In literature, there are many configurations exploiting this idea. Salisbury absorbers are the first examples of classical quarter wavelength absorbers. Jaumann absorbers are the multi-layer version of Salisbury absorbers, also first examples of broad-band absorbers. Dallenbach absorbers use the lossy media to absorb the incident power. Circuit Analog absorbers both use resistive and reactive lumped components in a layer. Geometric Transition absorbers are mostly used in anechoic chamber, creating slowly varying transition from free space into the lossy media. The slowly varying geometry is realized with pyramids or wedges. Low Density absorber is the material with a porous or sparse structure to resemble free space conditions and thick to create enough loss. The above mentioned topologies mostly share the following common properties; the absorber thickness should be more than $\lambda_0/4$ and poses a problem for multi-resonant structures since they have to be multi layers each of which should have a thickness at least of $\lambda_0/4$. The material within the quarter wavelength should be naturally impedance matching which means that there is a need for specific materials. Due to the reasons above mentioned, these sort of absorbers are mainly restricted to the frequencies below 30GHz. Metamaterial based absorbers propose a remedy for the above mentioned problems, [59]–[61]. While classical absorbers need a quarter wavelength thickness, metamaterial absorbers can do the same job with smaller thickness; i.e., $\lambda_0/35$.

Figure 1.14 shows two different approaches cited in the literature to implement the high fill factor structures. One of them involves the isolating arms and the active

material on different levels of the detector separated with an air gap, Figure 1.14 - (a), which is difficult to realize in practice since the ROIC connection must extend beyond two levels to reach the active part. The other one involves both the isolating arms and the active part on the same level, now the ROIC connection should extend only one level to reach the active part. The second level is only responsible for the IR absorption. In this study, the latter one will be examined due to the easiness it presents in the process.

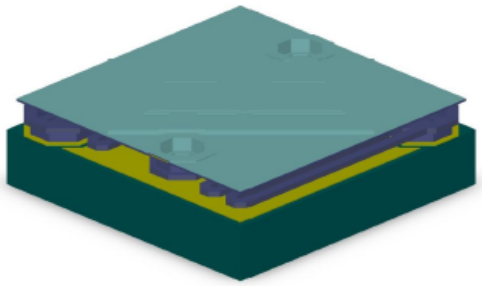

(a) Schematic view of a two-level bolometer. The isolating arms and the active material are on the different levels separated with an air gap with this topology, [37].

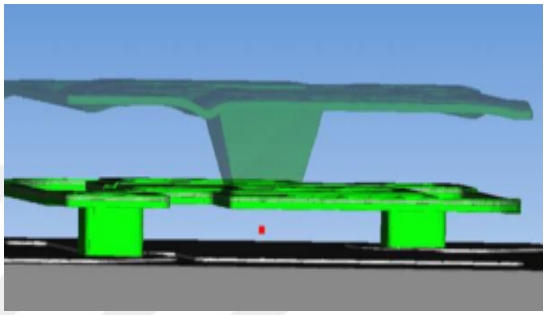

(b) Schematic view of a one-level bolometer. The isolating arms and the active material are on the same level, [28].

Figure 1.14: Schematic views to represent the two different topologies to implement the high fill factor structures in the literature, [28], [37]. *One of them involves the isolating arms and the active material on different levels of the detector separated with an air gap, (a), which is difficult to realize in practice. The other one involves both the isolating arms and the active material on the same level, the second level is only responsible for the IR absorption.*

1.5 Research Objectives and Thesis Organization

In literature, the absorber part of the bolometers is generally composed of a lossy metal layer used for the free space impedance matching purposes and a passivation layer mostly holding the resistive metal layer. Also, the whole absorbing layer is quarter wavelength away from a reflector layer ensuring a Fabry-Perot resonance,[62]–[65]. The absorbing layer material could be a variety of metals Nichrome (NiCr), Titanium (Ti), Titanium Nitride (TiN), Gold Black, Tungsten, [66]–[70]. The absorbing layer might be spaced apart from the temperature sensitive part or not as explained in the previous section. In literature, there are examples of pixel structures where the isolation arms with the active material and the IR

absorption layer are separated away on different levels of the structure, which will also be the pixel topology examined in this study. Two aspects for the employment of the perforation with this sort of topology are thoroughly examined in the literature. One aspect tells that the perforation provides artificial increase in the sheet resistance of the absorber metal that it might not be obtained as high as with the usual deposition of the metal, in turn, increasing the absorption rate, [70], [71]. An improvement with the time constant is also expected due to loss by the thermal mass. Another aspect ensures that the vacuum requirements for the packaging are relieved by decreasing the molecular heat transfer ratio with the employment of the perforated structures, [72]. Also from process point of view, the perforation gives an ease while patterning the layers beneath the perforated structures. The aim of this thesis study is the analysis and the implementation of the perforated structures to the pixel topologies employed at METU MEMS facility.

Figure 1.15 shows the regarding Scanning Electron Microscope (SEM) images and the FTIR measurement results regarding the effect of the perforation on absorption performance for a study reported in the literature, [71]. The claimed enhancement seems, actually, minimal in the LWIR range.

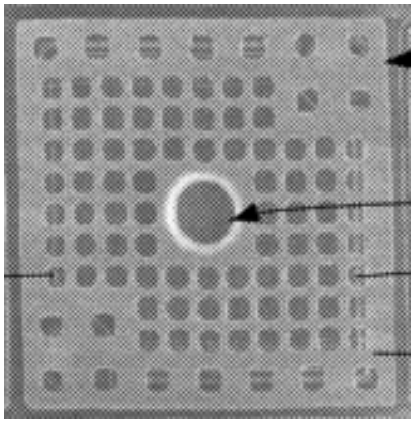

(a) SEM image of a perforated umbrella structure on a single pixel.

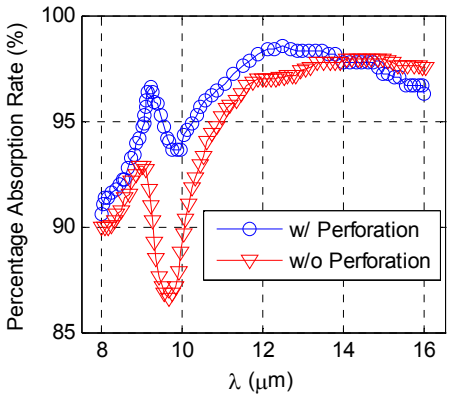

(b) Effect of the perforation on the percentage absorption rate in LWIR range.

Figure 1.15: The SEM image and the regarding percentage absorption rate of a single pixel composed of a spaced apart body and umbrella structure, [71]. *There is an absorption enhancement in a narrow band around 9μm by 10%. The key issue here is actually not to degrade the absorption performance while decreasing the thermal mass with perforation as it will be underlined in this study.*

Figure 1.16 shows the SEM image and the FTIR results of another implementation of perforated pixel structures in the literature, [73]. They present the FTIR results and the HFSS simulations of the perforated structure, not a differential analysis result as in the previous study. They claim an improvement by 30% with the responsivity performance.

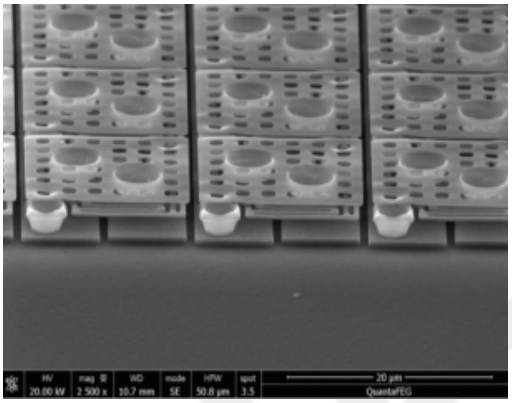

(a) SEM image of double sacrificial layer, perforated 17μm microbolometer.

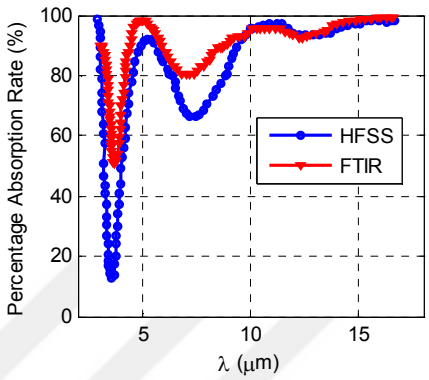

(b) Simulated and measured absorption characteristics of microbolometers with perforated umbrella structure.

Figure 1.16: SEM image (a) and absorption characteristics (b) of 17μm pixel pitch 640x512 IRFPA employing double sacrificial layer microbolometers with perforated umbrella structures as the absorber structures, amorphous vanadium oxide thin film as the active layer. NETD of 35mK @300K with f/1.0 optics is obtained. With the second platform incorporating frequency selective surface; i.e., perforation, responsivity of the microbolometer is improved by 30% over (8-14) μm range, [73].

In Chapter 1, the concept of IR radiation with a brief examination of the literature is familiarized. The motivation behind the implementation of perforation is also explained in this chapter. Chapter 2 introduces the IR characterization results for the perforated umbrella layers. In Chapter 3, a canonical topology to optimize the perforation related topology is examined through simulations. The fabrication and the measurement results are also presented in this chapter for both the canonical topology and high performance detector pixels. Lastly, in Chapter 4, a brief summary of the studies performed is presented and some steps to be taken as a future work are mentioned.

CHAPTER II

INFRARED CHARACTERIZATION OF UMBRELLA LAYERS

This chapter is mainly about presenting the IR characterization results for the umbrella layers; i.e., Silicon Nitride (Si_3N_4) and the Nichrome layers. Thus the characterized parameters can be embedded into simulation programs. First a method, spectroscopic ellipsometry, to make the dispersive IR characterizations is introduced. Then the dispersive model for the silicon nitride (Si_3N_4) is presented and examined through simulations. The examination and the characterization of the silicon nitride layer along with the Nichrome (NiCr) layer are also done simultaneously with the employment of both the FTIR measurement results and the CTL (Cascaded Transmission Line) theory. A non-dispersive model for the Nichrome resistive layer is proposed.

2.1 Spectroscopic Ellipsometry Technique

The characteristic interaction of EM waves with a material can be described through complex refractive index ($\tilde{\boldsymbol{n}}$) or complex permittivity ($\tilde{\boldsymbol{\varepsilon}}$) for a non-magnetic material as follows, Equation (17).

$$\tilde{n} = n + ik$$
$$\tilde{\varepsilon} = \varepsilon_r + i\varepsilon_i \qquad (17)$$
$$\tilde{\varepsilon} = \tilde{n}^2$$

While the refractive index, n, is directly related to the speed of the EM wave in the medium, the extinction coefficient, k, is related to the absorption mechanism that take energy from the EM wave. The type of mechanism depends on the wavelength of the EM wave. For instance, while IR absorption is commonly caused by molecular

vibration, phonon vibration, or free-carriers, UV absorption is generally due to electronic transitions, where light provides energy to excite an electron to elevated states. The interaction mechanism can manifest itself with a measurable change in the amplitude or the phase of the polarization of the EM wave, [74], [75].

Spectroscopic ellipsometry manages to extract these values from polarization changes of the interacting EM wave, [74]. The orientation and progress of electric field of an EM wave in space and time is known as polarization. When the EM wave has completely random orientation and phase, it is considered un-polarized. For ellipsometric measurements, however, we are interested in the kind of polarized one which means that the electric field vector traces out a distinct shape in space within a given time interval. When two orthogonal components of EM waves are in phase, the resulting wave will be linearly polarized. The relative amplitudes will determine the resulting spatial orientation. If the orthogonal waves are of arbitrary amplitude and phase, the resulting wave is said to be elliptically polarized.

For the ellipsometric measurement, a broad spectrum of IR beam with a known polarization, produced via a polarizer, is incident upon the sample. Then the change in the polarization of the reflected beam is measured via another continuously rotating polarizer. The complex parameter ρ, Equation (19), indicates the ratio of the reflected polarization to the incident polarization. Two other parameters in the equation define this complex value; while tangent of Psi (Ψ) parameter defines the amplitude part, Delta (Δ) defines the phase of the complex number. Both ellipsometric parameters, Ψ and Δ, are dependent on the thin film thickness, optical constants of the sample material, angle of incidence and of course on the wavelength of the IR illumination, [74], [75]. Figure 2.1 explains for the schematic representation of the ellipsometric measurement.

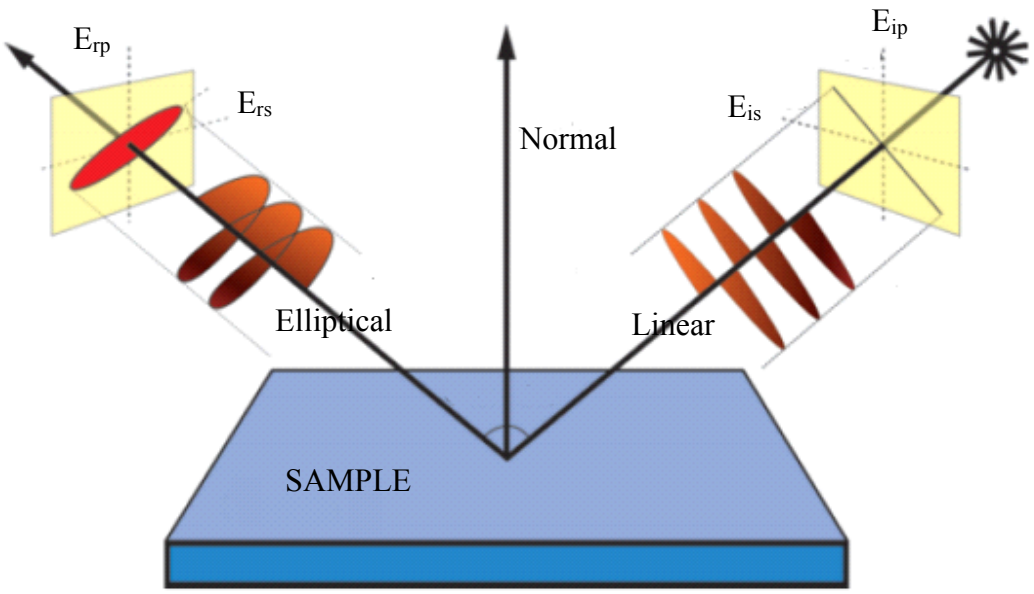

Figure 2.1: Schematic representation of the ellipsometric measurement. The incident linear polarization (Eis, E_{ip}) is disturbed after the interaction of the EM with the sample material resulting in another polarization (Ers, E_{rp}). Two polarizations, s and p, represent the parallel and orthogonal components of both incident and the reflected field with respect to the plane of incidence, [74].

The change in polarization is formulized as follows, Equation (18) and (19) in accordance with the configuration presented in Figure 2.1.

$$\tilde{E}_{xp} = E_{xp} e^{i\beta_{xp}} \text{ , x=i, r} \qquad (18)$$

$$\rho = \frac{E_{rp}/E_{ip}}{E_{rs}/E_{is}} e^{\left\{i\left[\left(\beta_p-\beta_s\right)_r-\left(\beta_p-\beta_s\right)_i\right]\right\}} = \tan(\Psi)e^{i\Delta} \qquad (19)$$

Within the scope of this study, the optical characteristics in the region of interest are examined using Infrared Variable Angle Spectroscopic Ellipsometer (IR-VASE) device with the trademark of J.A. Woollam Company.

2.2 IR Characterization of Silicon Nitride Material

Silicon nitride layer is one of the vital materials used in bolometer structures mostly used as the structural layer. Other than being used as the structural layer holding the

active part of the pixels, it can also be employed to construct the umbrella layer itself. The silicon nitride layer is deposited through Plasma Enhanced Chemical vapor Deposition (PECVD) as a low-stress layer at the METU MEMS Center. During the perforation, both Si_3N_4 layers and the NiCr layer sandwiched by the Si_3N_4 layers are patterned together. After underlining the importance of the material, it is obvious that the optical characterization of such a frequently used material is a must. Figure 2.2 shows the schematic view of the preparation of this material for the characterization through IR-VASE. A sample of 200nm thickness is used to characterize the material; however 400nm and 600nm are also tested for other studies, which all give the same optical constants within an acceptable error range. After the Ψ and Δ data are measured, by modelling, in other words, by introducing these layers in the same deposition order into the IR-VASE interface, both optical constants and thickness of the layers are obtained. The very same topology can also be used for the FTIR measurements, thus we can compare both the measured and simulated reflections for the layer in question which is in this case the Silicon Nitride layer.

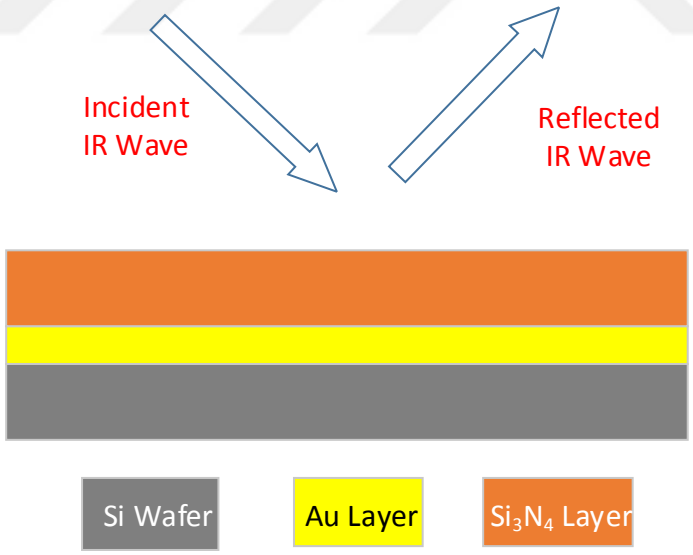

Figure 2.2: Schematic representation of the deposition of several layers to characterize the Silicon Nitride (Si_3N_4) material. The blank wafer of Silicon (Si) is deposited over with 100nm Au layer for full reflection purposes and then 200nm of Si_3N_4 layer is deposited for the characterization.

Figure 2.3 shows the measurement results for the ellipsometric characterization, Ψ and Δ parameters. After obtaining these results, we introduce a model into the program giving a rough estimate for the thickness and the optical constants and fit the measured data with the rough estimates.

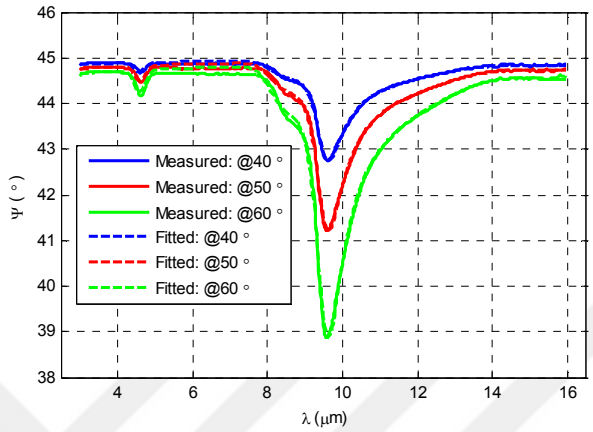

(a) Spectral distribution of Psi (Ψ) parameter.

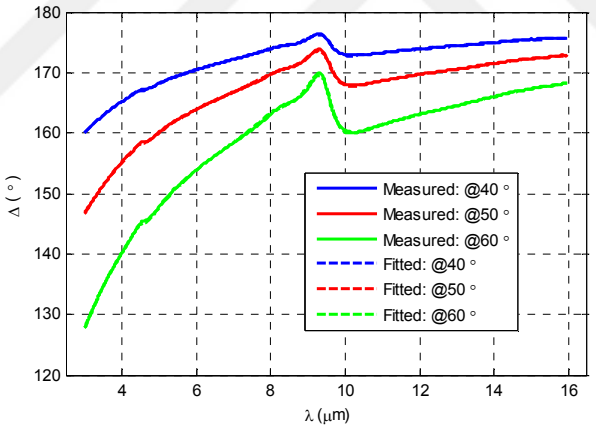

(b) Spectral distribution of Delta (Δ) parameter.

Figure 2.3: Ellipsometric characterization of 200nm Si_3N_4 over 100nm Au through IR-VASE. Psi (Ψ) parameter, which is correlated to the amplitude change with the polarization (a) and the Delta (Δ) parameter, which is correlated to the phase change with the polarization (b), are shown. For thin layers, Psi is not a sensitive one as you may also observe while Delta is quite sensitive to spectral change. The peaks in the figure give an idea about the absorption bands.

Figure 2.4 shows the measured optical constants for the 200nm nitride layer and the real thickness of the deposited thin film, which is around 170nm. The thickness is

also verified with the cross-sectional SEM image examination. The measured optical constants for the nitride layer fits also well with the results presented in the literature, [76]–[79].

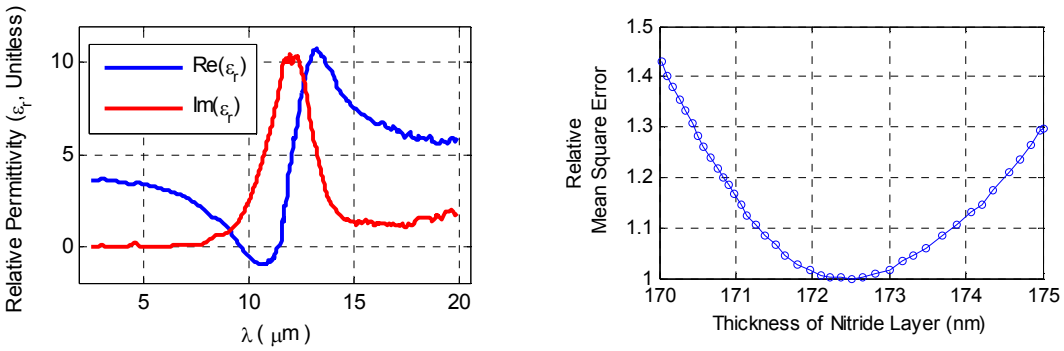

(a) *(b)*

Figure 2.4: The measured complex permittivity values of the Si_3N_4 by the IR-VASE Ellipsometry (a) and the thickness measurement result (b). The nitride thickness seems to be around 172nm, which is verified through cross-sectional SEM examination.

The confirmation of these results will be done through both simulations and the measurements with the characterization of the thin film NiCr layer in the following section.

2.2.1 Verification by Simulation Results

The verification of the measured optical constants of the Silicon Nitride is done by embedding the measured data into various simulation programs; i.e., obtaining the percentage absorption rate accordingly and predicting the FTIR measurement results. We did a comparative study for a 1μm thickness of bulk Si_3N_4 layer with various 3D EM simulation programs; HFSS, Lumerical and CST, even examined the response of different techniques; Floquet, Perfect Match Layer (PML) and Perfect Electric Conductor/Perfect Magnetic Conductor (PEC/PMC), in each simulation program. This study is done to make sure if there is anything wrong with the simulation setups and the embedded data. We have also had the opportunity to observe the differences presented by various programs and the methods. Another reason was that we did not have the FTIR measurement results in time. With HFSS, one of the methods we have

employed is the Floquet approach with the Master/Slave boundary conditions (BCs). Floquet approach is a purely mathematical model to handle infinite arrays thus we can employ it to extract the EM response of a large enough bulk material. The Floquet port both includes the field excitation and the matching layers preventing the undesired reflections at the port sides. Another method is to employ PEC/PMC BCs instead of the Master/Slave with the Floquet port approach. By using the PEC BCs, you can infinitely duplicate electric field within a period size, which is actually a generic way to model large arrays in EM simulation programs. Eventually you automatically calculate the S-parameters with these techniques and get the reflection and transmission data. PML method with the Incident Plane Wave (IPW) excitation can replace the Floquet port concept. After employing this method we do not have the S-parameters, you directly calculate the Poynting vector (a vector giving the amount of the EM power within its flow direction) over a surface, through which you can extract the reflection and transmission data by using the "Field Calculator", [80]. For PML we have two methods to calculate the absorbed power: First we can find the Volume Loss Density inside the slab and integrate it within the volume and normalize with respect to the incident power (PML-1). Secondly we can calculate the incident, reflected, and the transmitted power. The difference between them corresponds to the absorbed power (PML-2). There will be a difference between these two methods. Practically, this difference stems from the different Field Calculator expressions employed.

The methods employed for the transmission/reflection calculations in HFSS can also be directly applied for the other simulation programs. Figure 2.5 shows the simulation setups for both Floquet and PML approach. As it is observed, the PML box and the IPW can replace the Floquet port.

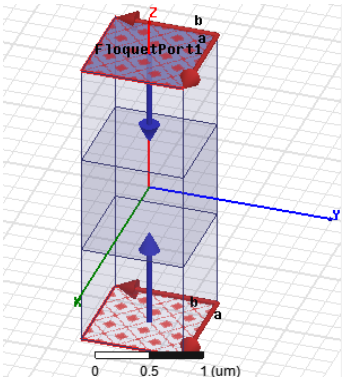

(a) Floquet based unit cell simulation setup for a slab of material

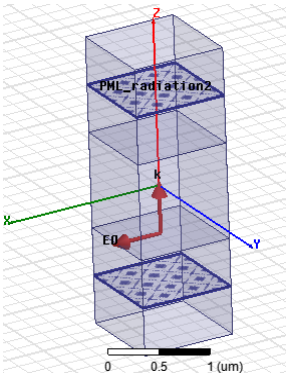

(b) PML based unit cell simulation setup for a slab of material.

Figure 2.5: The unit cell simulation setups for the Floquet based (a) and the PML based (b) approaches in HFSS for a Si3N4 slab of 1μm thickness. They are equivalent techniques, PML box and the incident plane wave excitation both can replace the Floquet port concept

Figure 2.6 shows the percentage absorption for a nitride slab of 1μm thickness obtained through various simulation programs and different techniques employed. The results are quiet satisfying; the difference in absorption rate for various methods is at most 5% for the lower frequency range. These results are confirming the fact that the setup is working for all types of methods and they verify each other.

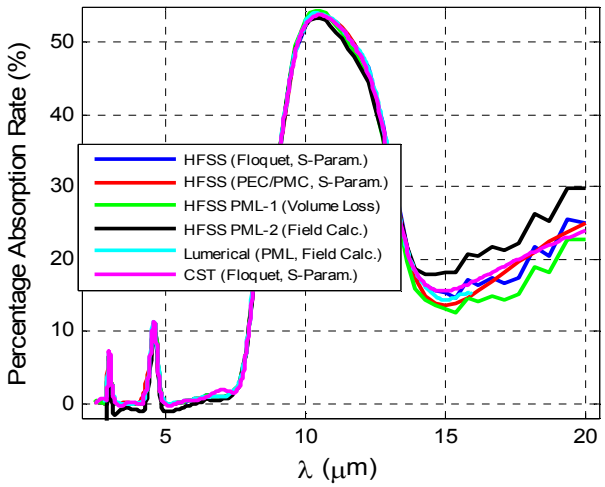

Figure 2.6: A comparison of the simulation results regarding the percentage absorption rate for a Si3N4 slab of 1μm thickness with different simulation setups. They seem all consistent, the subtle differences near 20μ can be blamed for the different fitting algorithms for the embedded optical constants employed by the simulation programs, i.e., it is expected. Nevertheless the variation in percentage absorption rate is at most 5% for lower frequencies.

2.3 IR Characterization of the NiCr Based Absorber Layer

2.3.1 Dispersive Model

Among many IR absorbing materials, NiCr is the mostly used one in literature. At METU MEMS Center, this material is deposited with Sputtering. By using SEM inspection or mechanical profiler it is estimated that 900 seconds of deposition time corresponds to a thickness of 50nm. However, the deposition time used for to create the IR absorber layer is around 90 seconds. The corresponding thickness cannot be measured directly using the infrastructure of the METU MEMS Center, however the sputtered thickness is considered to be directly proportional to the deposition time with Sputtering technique and then it is estimated to be around 5nm for a deposition time of 90 seconds.

Ellipsometry can be used to characterize both thin films and bulk materials, infrared ellipsometer works best for a thickness range of 100nm to 50μm, [75]. Also roughness of features on the sample should be less than 10% of the probing beam wavelength to eliminate non-specular scattering resulting in depolarization. Thus, a thickness of 5nm is quite problematic to deal with. Thus, a dispersive model; i.e., a model with frequency dependent optical constants, could not be obtained after many trials with various thicknesses of NiCr. However there is a study in the literature claiming that it can be done for about 15nm NiCr layers, [81]. In this study, the sample is deposited with DC magnetron sputtering technique. Average percentage absorption of 77% for the total device, employing V_2O_5 as the active material, is reported.

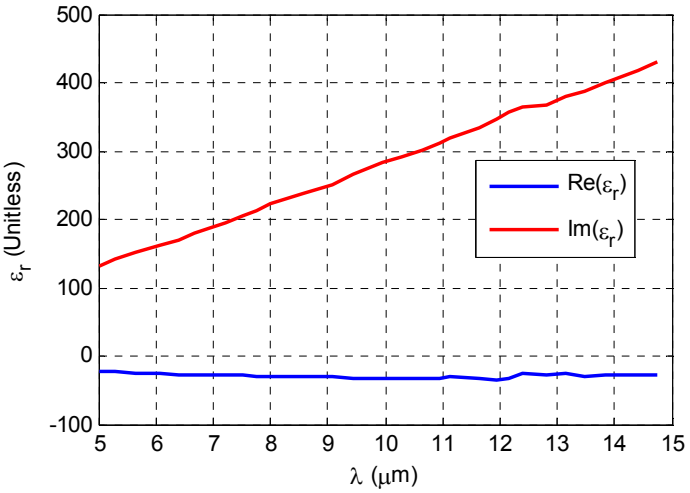

Figure 2.7: Measured complex permittivity belonging to a NiCr sample of 15nm thickness. The measurement is done through SENDIRA IR ellipsometer. The sample is deposited with DC magnetron sputtering technique. An average percentage absorption of 77% for the total device, employing V_2O_5 as the active material, is reported with this study, [81].

2.3.2 Non-Dispersive Model

Problems with ellipsometric characterization of the thin IR absorbing NiCr layer led us to make a non-dispersive assumption; i.e., to find a model for the thin NiCr layer involving a frequency independent parameter. With the model proposed, the NiCr layer is represented by a non-dispersive two-dimensional resistive layer and the regarding parameter would be the effective sheet resistance (R_s) of this resistive layer. In classical ellipsometric characterization, information related to the polarization change is used. However, the method proposed here is using directly the change in the field values instead of polarization changes with the help of Cascaded Transmission Line (CTL) theory. Thus, to examine this assumption, measurement samples, including a mirror layer of 100nm Au, backing up a 600nm Silicon Nitride (Si_3N_4) layer which is terminated with a NiCr layer, are prepared, Figure 2.8 - (a). The Si_3N_4 layer is needed in those characterizations to obtain measurable change in the measured field values. Specifically, this topology is selected to characterize the thin NiCr layer since it resembles to the real scenario where the NiCr layer will be sandwiched by the two Si_3N_4 layers, also there is no any lithography or mask needed to make those characterizations with this method. The main intention here is to find a correlation between the deposition times and the effective R_s of the thin, IR

absorbing, resistive NiCr layers. The layer thickness of the Si_3N_4 is selected to be around 600nm to read high enough values with the FTIR measurements. Figure 2.8 - (b) shows the FTIR measurement results for characterization purposes, for the proposed topology employing NiCr layers having various deposition times. The characterization is done over the deposition times rather than the exact thickness values of the NiCr layer since they are arguable as it is explained in the previous section.

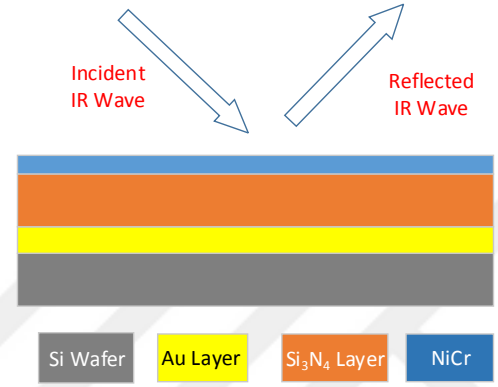

(a) Cross-sectional schematic view of the deposited layers to characterize the NiCr layer.

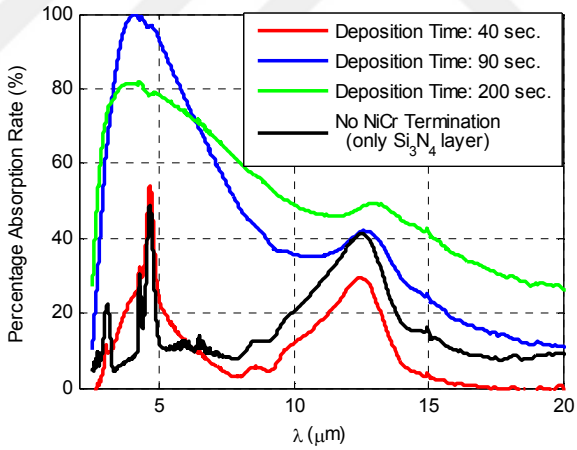

(b) FTIR absorption results for the topology described in (a), with various deposition times of the thin, IR absorbing NiCr layers.

Figure 2.8: The topology used in the non-dispersive characterization of the NiCr layer, (a) and the FTIR absorption characteristics of the topology, (b) to examine the correlation between the deposition time and the sheet resistance (R_s) of the NiCr layer. The characterization is done over a fitting of the FTIR measurements between the Cascaded Transmission Line (CTL) pre and FTIR measurements. For the 90sec. case, the fitting is good and the R_s is determined to be around 400Ω/□. For the 200sec. case, the fitting is also successful and the R_s is determined to be around 150Ω/□, which is less than the 90 sec. case. A thicker NiCr layer resulted in a smaller sheet resistance as expected.

The effective sheet resistance (R_s) measurement for NiCr layer is obtained through a fitting between the measured data and the simulated data via a Cascaded Transmission Line (CTL) code. The aim is to minimize the Root Mean Square (RMS) error between the fitted and the measured data. HFSS can replace the CTL code since they are exactly giving the very same result for the proposed topology above. However CTL presents a faster way of making those fittings. Figure 2.9 shows the schematic for the application of the CTL method to 1D thin film layers (an infinite length in transverse direction and a finite length in the longitudinal direction), specifically for the topology presented in Figure 2.8 – (a). In transmission line theory (TLT), 1D thin film layers can be modeled uniquely with a characteristic wave impedance (Z_{ch}) and wavenumber (γ). The assumption is that the sample is illuminated with a TEM (Transverse Electromagnetic) wave with a normal incidence.

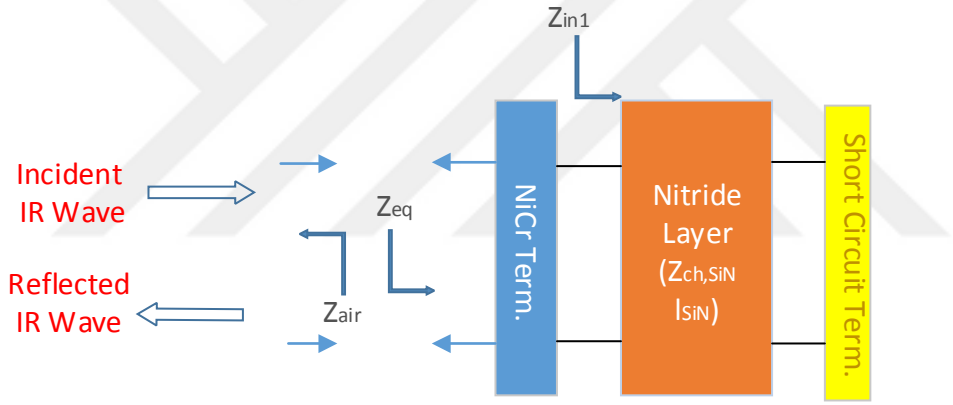

Figure 2.9: Schematic representation of the application of the Cascaded Transmission Line (CTL) code for the topology shown in Figure 2.8 – (a), used for the non-dispersive characterization of the NiCr layer.

The goal functions for the fitting trials are to be the FTIR measurements. A two-dimensional fitting is done over both the R_s of the NiCr layer and the thickness of the Si_3N_4 layer beneath it. Since the Si_3N_4 thickness is already known via different methods such as ellipsometric fitting or SEM inspection, actually one-dimensional fitting for the determination of the R_s will also be enough, since it is the prime concern. However, the inclusion of the Si_3N_4 thickness to the fitting will also be a nice cross-check to assess how successful the CTL method is. Because if one

dimensional fitting with the R_s is done, no matter what the result is, the result should be accepted; i.e., there is no cross-check for it. However, with the inclusion of the Si_3N_4 thickness, the success of the CTL fitting can also be assessed through a comparison between the fitted and the measured Si_3N_4 thickness values. In literature, there is also a similar, contactless, non-destructive method employed at microwave frequencies, [82].

Equation (20), (21), (22), and (23) explains for how the fitting function is obtained using the CTL assumptions. $Z_{ch,SiN}$ represents for the characteristic impedance, γ_{SiN} for the complex wavenumber, and l_{SiN} for the thickness of the Si_3N_4 layer. R_S stands for the sheet resistance of the NiCr layer. Z_{air} is the characteristic wave impedance of the free air, which is actually 377Ω in value. Z_{in1} is the terminal value obtained at a point of the cascaded lines using the CTL theory. Using the CTL, a terminal impedance value at any point of a multi-layer structure can be found. Since the whole structure is terminated with an IR mirror layer (short circuit termination), through the total reflection calculated using Equation (22), absorption can also be expressed as *(1-Reflection)*.

$$Z_{in1} = Z_{ch,SiN} * \tanh(\gamma_{SiN} * l_{SiN}) \quad (20)$$

$$Z_{eq} = Z_{in1} // R_s \quad (21)$$

$$Reflection = \left(\frac{Z_{eq} - Z_{air}}{Z_{eq} + Z_{air}}\right)^2 \quad (22)$$

$$\gamma_{SiN} = j * w * \sqrt{\mu_{air} * \varepsilon_{SiN}} \text{ and } Z_{ch,SiN} = \frac{j*w*\mu_{air}}{\gamma_{SiN}} \quad (23)$$

Figure 2.10 shows the fitting trials for the 90sec. of deposition time. The fitting band is set to be (2 - 20) μm range, additionally, a narrow-band examination around the peak absorption values disregarding the CO_2 effect is also done. There is a difference between the wide and the narrow band fitting results, which can be ignored since it still gives out a distinctive range for both the R_s and the Si_3N_4 thicknesses. The effect of the CO_2 absorption around 4.5μm is intentionally eliminated since it was

disturbing the results. The simultaneous fitting of the sheet resistance of the NiCr layer and the thickness of the Si_3N_4 layer resulted in the following values: 400Ω/□ for the R_s and 550nm for the Si_3N_4 thickness. This value of Si_3N_4 thickness is also roughly verified through other methods; such as SEM inspection giving out a value around 540nm, which is actually quiet close to the CTL prediction. Thus the fitted value for the R_s is more reliable now since a nice match between the fitted and measured values for the Si_3N_4 thickness is also observed through the two-dimensional fitting and the SEM inspection.

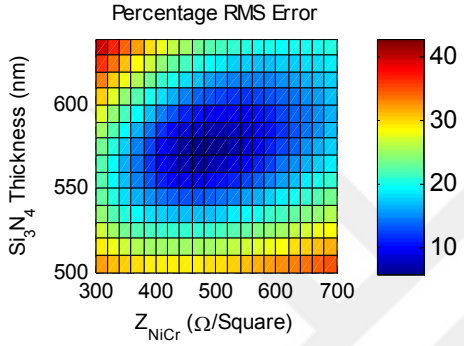

(a) Two-Dimensional optimization graph for 90sec. deposition time of the thin IR absorbing NiCr Layer.

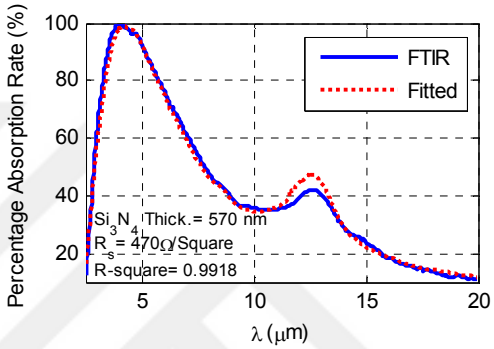

(b) Full-Band optimization results.

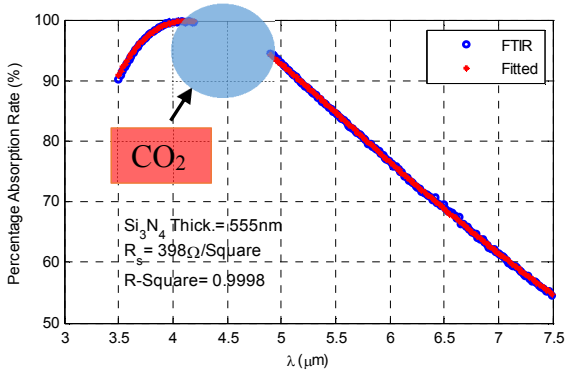

(c) Narrow-Band optimization disregarding the range of CO_2 absorption.

Figure 2.10: The simultaneous optimization of the sheet resistance of the NiCr and the thickness of the Silicon Nitride layer is done through a CTL code. The goal function is the FTIR measurement regarding a deposition time of 90 sec. for the NiCr layer. The R_s is predicted to be around 400Ω/□ with this code. The optimization with a narrow band around (3 - 8) μm is more reliable since it contains the maximum absorption value and also disregards the CO_2 absorption range (4.16-4.76) μm, i.e.; (2100-2400) cm^{-1}. The thickness measurement of the Silicon Nitride layer with the ellipsometry and the SEM examination also makes this fitting much more reliable.

Certainly, while doing these fittings, it should be remembered that the minima obtained with the RMS error graph is a local minima considering the inherent, generic λ/2 periodicity with the EM calculations. However if the values for the parameters under examination are kept in a practical range as it is done in this study, there will not be any problem; i.e., there will not be any extra local minima observed.

Figure 2.11 also verifies those results for a longer deposition time, 200 seconds. Since there is an increase with the deposition time, a decrease in the R_s value is also expected. The R_s value for 200 sec. deposition time is fitted to be around 150Ω/□.

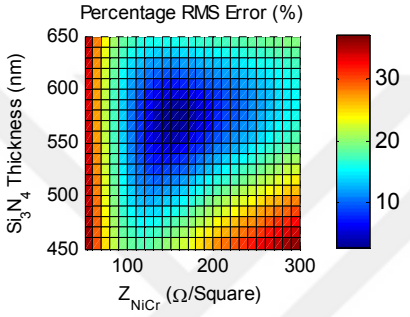

(a) Two-Dimensional optimization graph for 200sec. deposition time of the thin IR absorbing NiCr Layer.

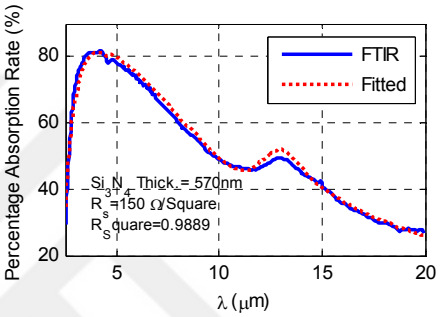

(b) Full-Band optimization results.

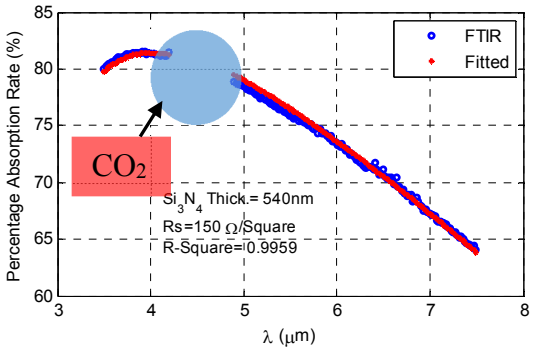

(c) Narrow-Band optimization disregarding the CO_2 absorption.

Figure 2.11: The simultaneous optimization of the sheet resistance of the thin IR absorbing NiCr layer and the thickness of the Silicon Nitride layer is done through a CTL code. The goal function is the FTIR measurement regarding a deposition time of 200 sec. for the NiCr layer. The R_s is predicted to be around 150Ω/□ with this code. The optimization with a narrow band around (3-8) μm is more reliable since it contains the maximum absorption value and disregards the CO_2 absorption range (4.16-4.76) μm, i.e.; (2100-2400) cm^{-1}.

In this chapter, to sum up, a dispersive modelling of 200nm Silicon Nitride in IR range is done by ellipsometric measurements and verified through the HFSS simulations, the CTL theory, and FTIR measurements. It is also explained why a dispersive model for the NiCr cannot be constructed, and how the situation is handled with a non-dispersive modelling by both using the FTIR measurement results and a CTL code.

Through the characterization trials, it is also proved that the absorbing performance of the thin NiCr layer is highly sensitive to the O_2 plasma recipes which are mostly used for the PR removal or Release processes. Figure 2.12 proves the performance degradation of the absorbing NiCr layer when it is directly exposed to various O_2 plasma recipes. It is also shown that a solution to this problem is to passivize the NiCr layer with an additional Si_3N_4 layer before the O_2 plasma exposure.

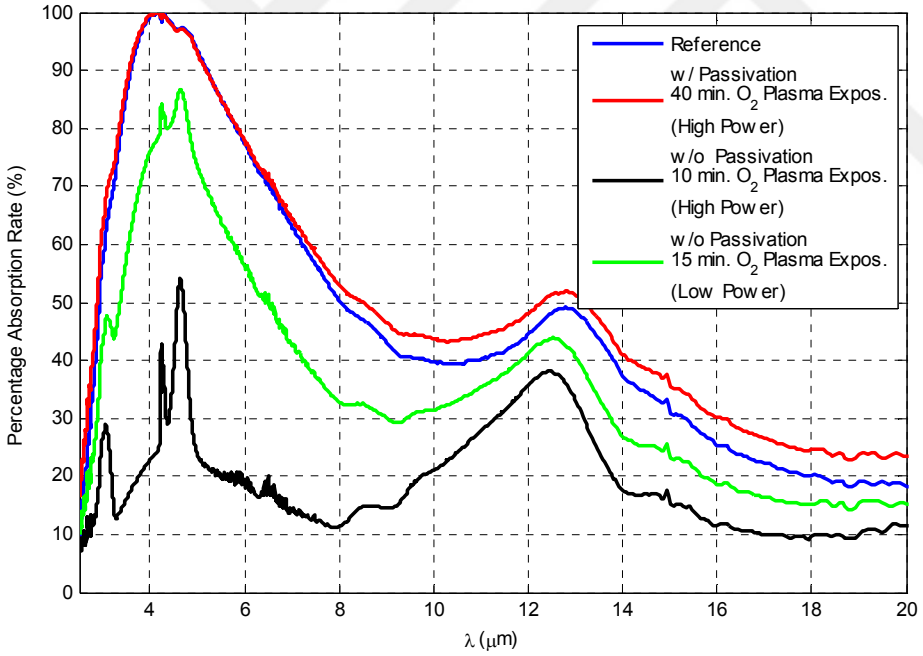

Figure 2.12: The absorption performance of the thin, absorbing NiCr layer after exposure to various O_2 plasma recipes. It is shown that O_2 plasma recipes degrade the absorbing performance unless the NiCr layer is passivized with an additional Si_3N_4 layer.

CHAPTER III

DESIGN AND FABRICATION OF PERFORATED STRUCTURES

This chapter introduces the design, simulation, fabrication and measurement results for a canonical perforated umbrella topology along with the high performance pixels. First, through HFSS simulations unit cells for the perforation are optimized to obtain high absorption rates. Then the fabrication process is explained thoroughly, process related optimization results have been justified. Next, both the FTIR measurement and HFSS simulation results are compared for the canonical topology. It is observed that there is a good agreement between them. Thus the optimized values are also implemented with the high performance topology, there is also a good agreement with the expectation. Finally, some transient thermal analysis is done to examine the effect of the perforation on the thermal time constant. Through simulations, the improvement with the implementation of the perforation is also observed.

3.1 Design and Simulation of Perforated Umbrella Structures

The examination of perforated umbrella case needs for some canonical problem definition since the solution domain for the full pixel size can be diminished and also a physical insight into the problem can be obtained with a decrease in the complexity of the full pixel structure. This canonical structure both should answer for these needs yet should not lose its generality in terms of the results it presents. For this reason, we have selected the canonical; i.e., simpler version of the real problem topology, as suspended perforated umbrella structures backed with an Au mirror layer. This structure does not involve the effects of the body nitride, arm metals, electrode and the active material for a high performance pixel. Although it is a simpler version of more complex problem geometry for the high performance pixels, whole structure can be used to represent the exact situation by placing it on a low cost pixel. However, for low cost case we are aiming to place only the perforated

umbrella nitride layer without backing it up with the metal mirror due to cost issues. And, since we do not have the information about the IR characterization of the CMOS layers underneath the pixels, the whole optimization relies on educated guesses and differential analysis. Figure 3.1 shows the simulation setup and the topology for a unit cell in HFSS of the canonical perforated umbrella structure.

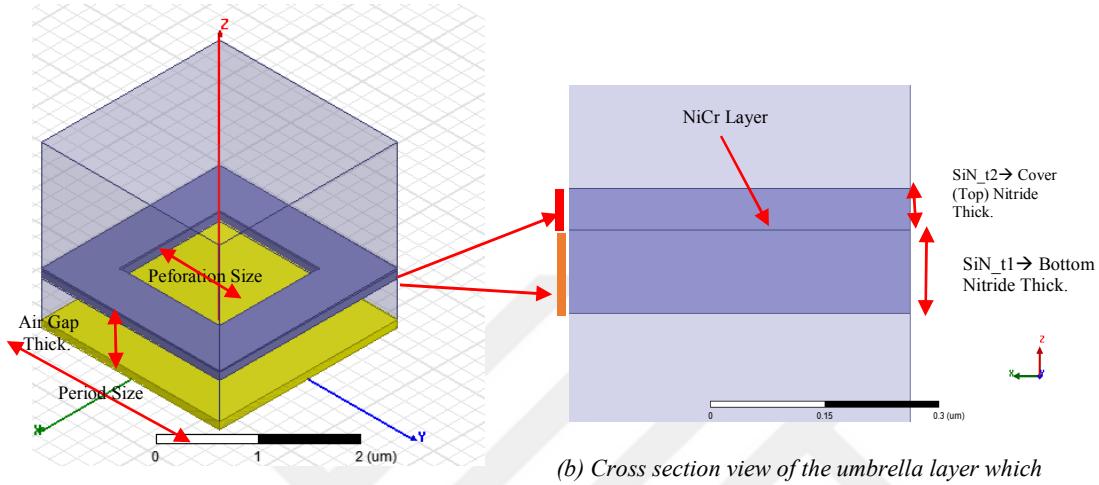

(a) HFSS unit cell topology for perforated umbrella structure backed with IR mirror layer.

(b) Cross section view of the umbrella layer which contains a thin NiCr layer sandwiched by cover (top) and bottom nitride layers. The NiCr layer is modeled with a simple 2D resistance layer.

Figure 3.1: 3D model of the designed unit cell to represent the perforated umbrella structures embedded into the HFSS simulation program. The nitride layers are defined as the new materials for HFSS by embedding the frequency dependent EM parameters (n, k). Since the nominal thickness of the NiCr layer is in the order of a few nanometers, the ellipsometric characterization of this layer was unsuccessful. Thu a 2D resistive layer modelling for this layer is employed through a contactless field based FTIR measurement.

Figure 3.2 shows the schematic representation of the CTL applied to canonical umbrella layers without perforation. Mirror layer is modeled with a short circuit termination. Sandwiched NiCr layer is modeled with a lumped resistor.

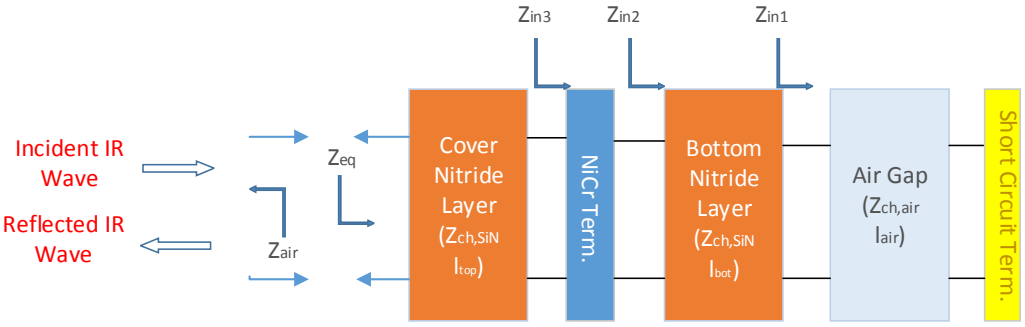

Figure 3.2: Schematic representation of the application of the CTL (Cascaded Transmission Line) code for the suspended umbrella structures. The CTL method assumes un-patterned, 1D (infinite sheets of layers) which has only a thickness in the propagation direction of the EM wave. Thus, this method cannot explain for the effect of the perforation yet.

Figure 3.3 shows the wide band IR absorption performance of the single perforation unit cell. Through this figure, it is observed that there is a good match between the analytical and the numerical calculations, the effect of the perforation is not observed in this figure yet. It seems that as the thickness of the umbrella increases the absorption performance degrades in the LWIR range and the peak in the MWIR range shifts.

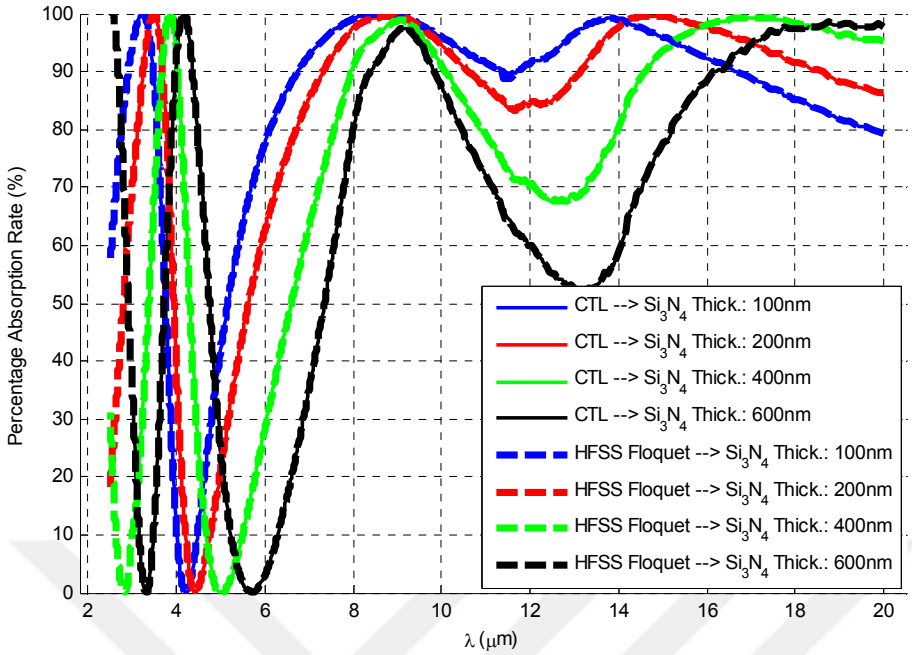

Figure 3.3: Percentage absorption rate of a unit cell for a canonical single perforation umbrella structure with various thicknesses of the bottom nitride; 100nm, 200nm, 400nm and 600nm. All configurations are covered with a top nitride of 50nm thickness. R_s is set to be 377Ω/□ the air gap thickness is 2.0μm, the period size is 2.0 μm and there is no perforation. It is observed that as the thickness of the bottom nitride increases, the average percentage absorption in the LWIR range decreases and the peak in MWIR range shifts to lower frequencies. The structure seems to be a dual band device in terms of absorption performance. It is also observed that both the analytical (CTL) and numerical (HFSS) calculations give exactly the same results for the field calculations.

Figure 3.4 shows a simple sensitivity analysis done for the LWIR range to observe the feasibility of the proposed topology. The sensitivity of the air gap thickness, perforation size, sheet resistance, and bottom nitride thickness to the absorption performance is examined. If the topology proved to be a sensitive one, due to unexpected process variations, this topology would not be feasible. Nevertheless, according to the simulation results, the topology is quite robust and the most sensitive parameter within the topology seems to be the air gap thickness.

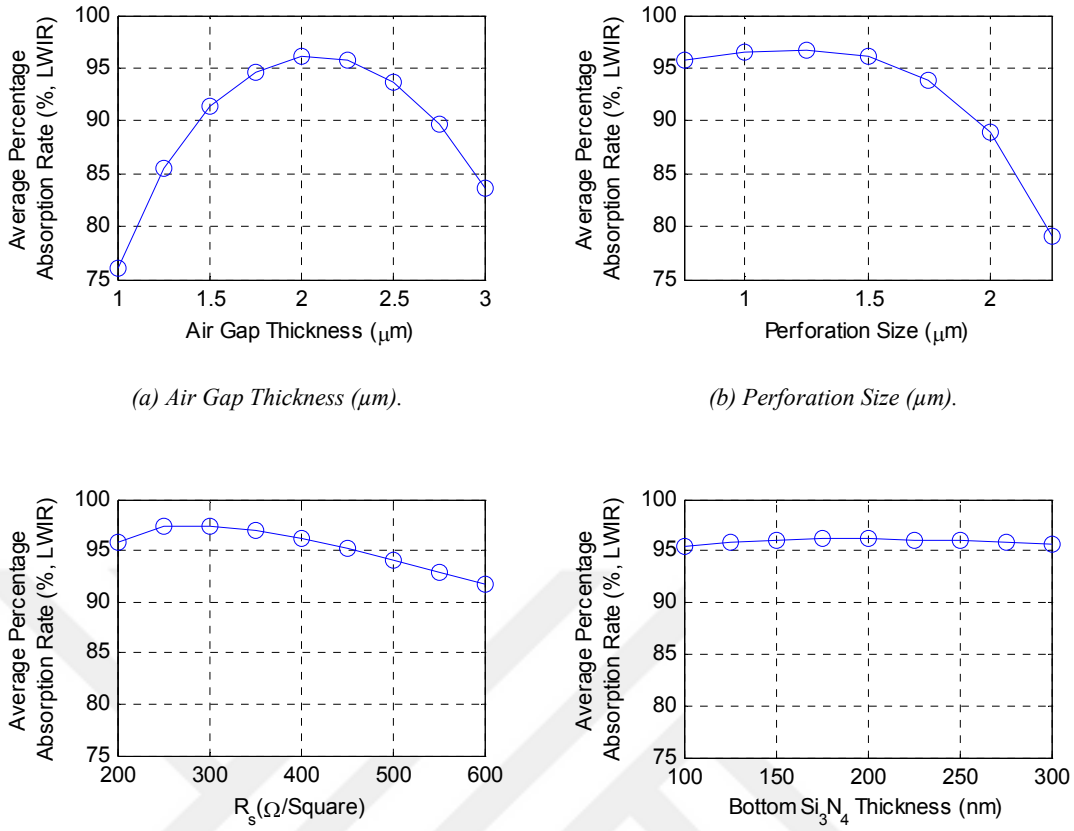

(a) Air Gap Thickness (μm).

(b) Perforation Size (μm).

(c) Sheet Resistance of NiCr (Ω/□).

(d) Bottom Silicon Nitride Thickness (nm).

Figure 3.4: Sensitivity analysis of the proposed topology. This analysis gives an idea about the robustness of the topology against to the small process variations. The analysis is done for an average absorption rate in LWIR (8 - 12) μm range. The assumption is if there is a 50% change in the mean value of the related parameter how much the absorption rate would be affected. Certainly, in practice this much of change is not expected however still gives an idea. The most sensitive parameter seems to be the air gap thickness and the least sensitive one is the thickness of bottom Silicon Nitride layer. Considering the practical process related variations, the topology is quite robust.

Figure 3.5 shows the optimization results examining the size of the perforation for various umbrella nitride thicknesses and various period sizes. It seems that for 100nm and 200nm thicknesses of the nitride, the perforation does not seem to enhance the absorption much. For other cases, the enhancement is not any more than 10%. On the other hand, for all nitride thicknesses, 50% perforation rate (perforation size/period size=0.5) seems to be upper limit for the size of the perforation, also independent of the period size not to degrade the absorption performance in the LWIR range. This optimization study should have to be done since the perforation size is also desired to be as large as possible for other concerns. For instance, if the

perforation rate is increased, the time constant of the pixel will decrease since the thermal mass would also be decreased, which is a desired condition. As the material mass is decreased the collision statistics between the air molecules and the pixel structure would be in favor of the vacuum requirements of the detector. With less material there will be fewer collisions and in turn less heat transfer will be done through the conduction by air. This will relieve the vacuum requirements of the detector. However if the perforation size keeps increasing, there will be a degradation with the absorption performance of the detector. Thus it turns out there is an upper limit for the size of the perforation to keep the absorption performance intact.

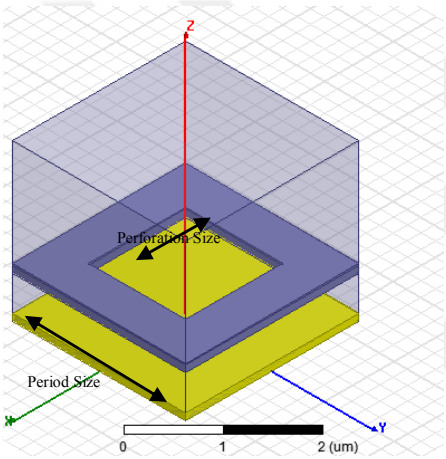

(a) Cross-view of the perforation unit cell.

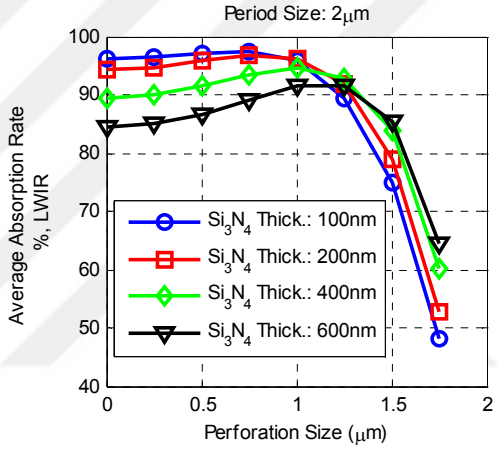

(b) Period size → 2μm.

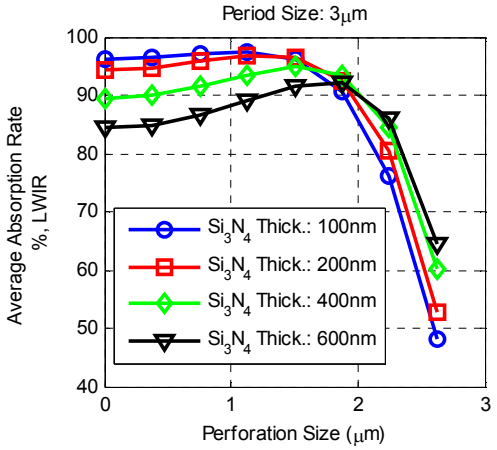

(c) Period size → 3μm, Figure 3.5 (continued).

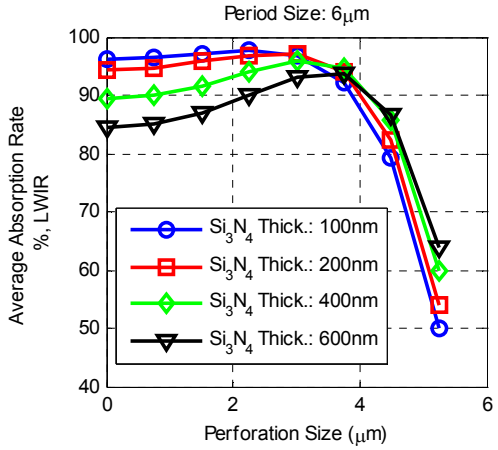

(d) Period size → 6μm, Figure 3.5 (continued).

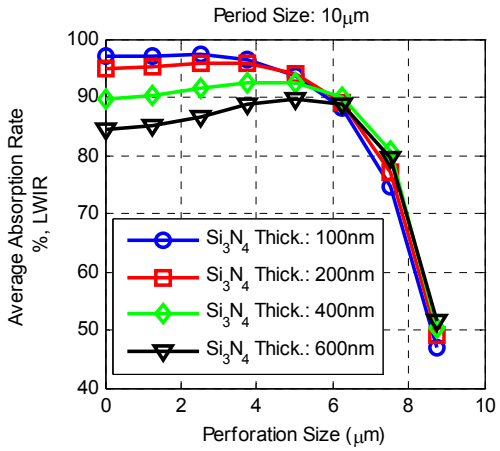

(e) Period size → 10μm

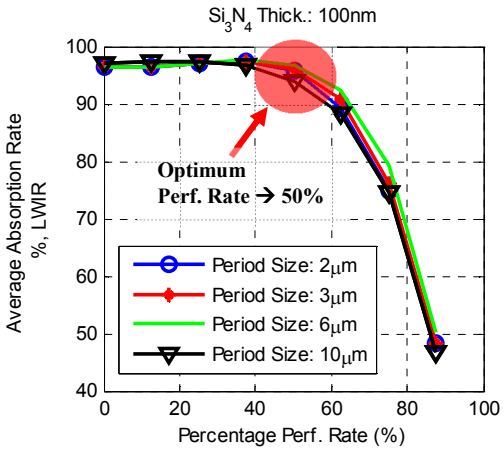

(f) Si_3N_4 Thick. → 100nm

Figure 3.5: A parameter sweep for the perforation size and for various period sizes over the average absorption within the LWIR range. These results show that the size of the perforations should not exceed the 50% of the period sizes, (f) not to degrade the absorption performance of the pixels in the LWIR range.

Figure 3.6 shows the effect of the post size on the absorption performance of the perforated umbrella. Posts are the structures holding the umbrella structure. It can be deduced from the simulation results that as long as the post diameter is less than 25% of the pixel pitch size, the absorption performance in LWIR range is not degraded by the existence of the post.

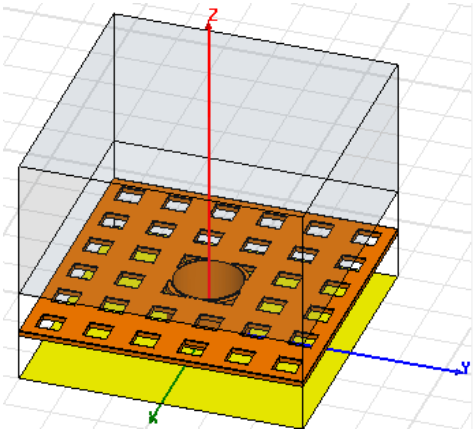

(a) The canonical HFSS model for the umbrella perforations, Figure 3.6 (continued).

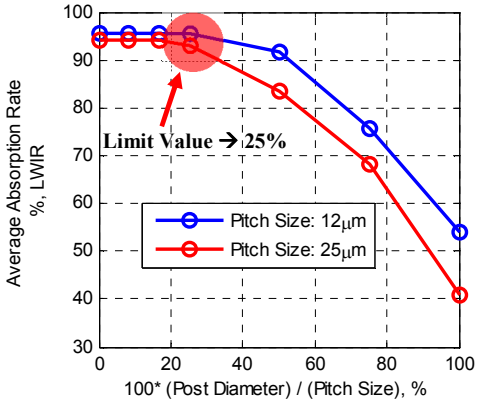

(b) Effect of post size on absorption characteristics, Figure 3.6 (continued).

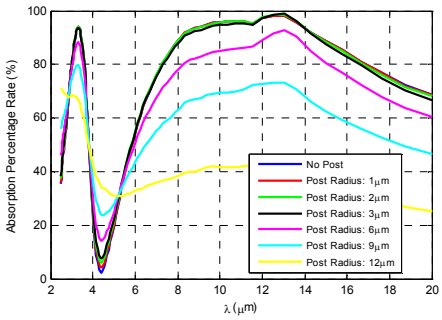

(c) Effect of various post sizes on absorption characteristics for 25μm pixel pitch size.

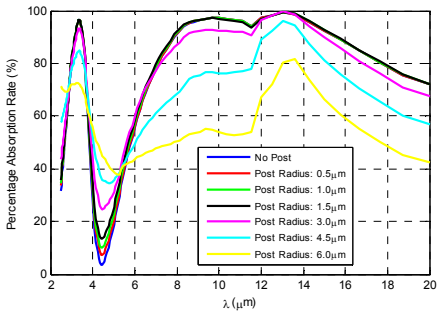

(d) Effect of various post sizes on absorption characteristics for 12μm pixel pitch size.

Figure 3.6: The effect of the post size on the absorption performance is examined for two pixel pitch sizes; 25μm and 12μm. The PML (Perfect Matched Layer) method with the Incident Plane Wave (IPW) is used for the simulations in HFSS. The unit cell used for the umbrella optimizations belongs to 50 % perforation percentage rate. The results show that the post diameter should not exceed the 25% of the pixel pitch size not to degrade the absorption performance in the LWIR range.

3.2 Fabrication of Perforated Umbrella Structures

The canonical topology having 69 configurations are examined to compare the HFSS (High Frequency Structural Simulation) modelling and the FTIR (Fourier Transform Infrared Spectroscopy) measurement results for the perforated umbrella process. Pixels having pitch sizes of 12μm, 17μm, 25μm and 50μm in each die are simulated, optimized, produced and tested. Additional to the various pixel pitch sizes, the effect of the different period sizes in which various size of perforations are placed, are all examined. The period size of 3μm and 4μm are tested with perforation sizes ranging from 0.5μm up to 3.0μm. The effect of different number of posts (1, 2 and 4) with various post sizes ranging from 1.5μm up to 25μm is also observed to evaluate their effects on both mechanical and electromagnetic performance. Table 3-1 shows the detailed information regarding the examined parameters for the optimization of the canonical perforated umbrella structures. The regarding mask is designed by Ozan Ertürk.

Table 3-1: A schematic representation of the placement of various types of pixels in one die, changing in pixel pitch sizes, period sizes, perforation sizes, post number and sizes. Each die involves pixels in 20 rows and 4 columns (a total of 78 pixels). With this run, the effect of the NiCr and the perforation is also tested differentially. NN acronym explains for the 'No Nichrome' case and NP explains for the 'Not Perforated' case. All pixels are successfully released as expected, the ones in red are used for FTIR measurements.

	12µm				17µm				25µm				50µm			
	Post Size	Post #	Period Size	Perf. Size	Post Size	Post #	Period Size	Perf. Size	Post Size	Post #	Period Size	Perf. Size	Post Size	Post #	Period Size	Perf. Size
#1		TEST RESISTORS							2	4	3.0	1.5	25	1	3.0	1.5
#2	1.5	1	2.0 2.0	1.3 1.0	3	1	2.0	0.5	5	1	3.0 3.0	1.7 1.5	15	1	3.0	1.5
#3	1.5	1	NN NP	NN NP	2	1	NN NP	NN NP	4	1	3.0	1.5	4	4	3.0	1.5
#4	1.5	1	NN 3.0	NN 1.5	2	1	NN 3.0	NN 1.5	2	2	3.0	1.5	3	4	2.0	1.0
#5	1.5	1	NN 3.0	NN 1.0	2	1	NN 3.0	NN 1.0	2	1	NN NP	NN NP	3	2	3.0	1.5
#6	1.5	1	NN 2.0	NN 1.0	3	1	NN 2.0	NN 1.0	2	1	NN 3.0	NN 1.5	3	2	2.0	1.0
#7	1.5	1	NN 2.0	NN 0.5	3	1	NN 2.0	NN 0.5	2	1	NN 3.0	NN 1.0	8	1	3.0	1.5
#8	1.5	1	NP	NP	2	1	NP	NP	2	1	NN 2.0	NN 1.0	8	1	2.0	1.0
#9	1.5	1	4.0	3.0	2	1	4.0	3.0	2	1	NP	NP	4	1	NN NP	NN NP
#10	1.5	1	4.0	2.5	2	1	4.0	2.5	2	1	4.0	3.0	4	1	NN 3.0	NN 1.5
#11	1.5	1	4.0	2.0	2	1	4.0	2	2	1	4.0	2.5	4	1	NN 3.0	NN 1.0
#12	1.5	1	4.0 4.0	1.7 1.5	2	1	4.0 4.0	1.7 1.5	2	1	4.0	2.0	4	1	NN 2.0	NN 1.0
#13	1.5	1	4.0 4.0	1.4 1.0	2	1	4.0 4.0	1.2 1.0	2	1	4.0	1.5	4	1	NP	NP
#14	1.5	1	3.0	2.5	2	1	3.0	2.5	2	1	3.0	2.5	4	1	4.0 2.0	2.5 1.0
#15	1.5	1	3.0	2.0	2	1	3.0 3.0	2.2 2.0	2	1	3.0	2.0	4	1	4.0 4.0	2.3 1.5
#16	1.5	1	3.0	1.5	2	1	3.0	1.5	2	1	3.0	1.5	4	1	4.0	1.5
#17	1.5	1	3.0	1.0	2	1	3.0	1.0	2	1	3.0 3.0	1.2 1.0	4	1	3.0	2.0
#18	1.5	1	2.0 2.0	1.7 1.5	3	1	2.0 2.0	1.6 1.5	2	1	2.0	1.5	4	1	3.0	1.5
#19	1.5	1	2.0	1.0	3	1	2.0 2.0	1.3 1.0	2	1	2.0	1.0	4	1	3.0 3.0	1.3 1.0
#20	1.5	1	2.0	0.5	3	1	2.0	0.5	2	1	2.0	0.5	4	1	2.0	1.0

The canonical topology involves a 25nm/100nm Titanium/Gold (Ti / Au) as the mirror layer. The air gap of 2µm length for ensuring quarter wave (λ/4) resonance is realized with the PI2610 or Level M10 sacrificial layers. The perforated umbrella structure involves 200nm/5nm/50nm (Silicon Nitride /Nichrome/ Silicon Nitride) sandwich layer. The umbrella is suspended over the mirror layer through the release of the sacrificial layer. The lithography process is done with the ASML stepper, which means that all configurations are tested in one die simultaneously.

A fresh start for a usual bolometer process run is initiated as follows; a prime wafer is deposited with 200nm Silicon Nitride (Si_3N_4) layer to provide electrical isolation of the deposited layers from the doped silicon of the prime wafer, Figure 3.7 - (a). Then the IR range mirror layer is deposited over the nitride layer, which is realized with the physical sputtering of 25nm Ti and 100nm Au layers, Figure 3.7 - (b, c). Ti layer is used to ensure the adhesion of the Au layer to the Si_3N_4 layer. The resulting metal layers are amorphous and the thickness is way larger than the skin depth of the

Au metal to obtain a perfect mirror for the IR range. At this point it should be remembered that the metal mirror is employed to create a Fabry–Perot effect to increase the IR absorption rate of the pixels, reference. Then a sacrificial polyimide (PI) layer, which will help forming the air gap after the release, is deposited over the mirror layer with the manual spinner device, Figure 3.7 - (d). The PI2610 material as the PI layer is deposited with the usual photoresist (PR) recipe with a spin speed of 2200rpm which corresponds to a thickness of roughly 2.0μm. At this point it should be remembered the fact that while depositing PI or PR materials to the one side of the wafer with a manual spinner, the other side is also contaminated with these materials which should be dealt with for the next steps of the process. Then a soft-bake @130˚C for 5 minutes is applied to strengthen the material. Next, a usual PI Bake recipe is applied to the wafer to harden the PI material. After baking, a hard mask of 30nm SiO_2 is deposited over the PI layer through PECVD method. A usual soft mask is not used since it would not survive the etching process of a 2.3μm PI layer. The hard mask is also protected with a soft mask, SPR220-3 @2000rpm. This soft mask is protecting the front side of the wafer which involves both oxide and PI layers, thus the back side of the wafer can be decontaminated. Without any lithography process is applied, the wafer is exposed to 15 minutes of O_2 plasma to clean the back side of the wafer from the PI residuals. Now, the damaged soft mask can be stripped, the SPR220-3 PR, with a usual acetone recipe. A fresh SPR220-3 PR layer with the spinner is re-deposited, this time to pattern the oxide hard mask. After patterning of the soft mask with the lithography process, an RIE of 22 seconds is applied to pattern the oxide layer to create the oxide hard mask. While the soft mask, which is used to pattern the hard mask is still on, an RIE of 70 minutes is applied to pattern the PI layer to obtain the post openings. The post is the structure holding the suspended umbrella. After making sure that the post openings are finalized, the soft mask PR is stripped away with usual Descum and acetone recipes, the oxide hard mask is also stripped with a suitable recipe with the RIE. After checking the patterned post openings with the Scanning Electron Microscope (SEM), the first nitride layer of the umbrella, with a thickness of 200nm is deposited over the PI layer with the PECVD method, Figure 3.7 - (e). Then Nichrome (NiCr) layer of approximately 5nm, the absorber layer, is deposited over the first nitride layer with the physical sputtering method. The lithography is done with Ultra-I, and the etching

is done with Inverse Sputtering, Figure 3.7 – (f). However etching of NiCr layer is actually quite problematic with Inverse Sputtering since it causes side-sputtering issue, some sort of contamination. To avoid it, the PR after the Inverse Sputtering is weakened with PR Strip recipe for 3 minutes, then a flood exposure of 40sec. is applied to weaken the PR layer more. Then MF24A developer is used to strip the Ultra-I, Acetone is also applied for 15 minutes. The result was quite satisfying and it is repeatable. This method has proved to be eliminating side sputtering well enough. Then 50nm protective nitride is deposited, both the bottom and the top protective nitride layer is etched simultaneously for 130 seconds exposure of RIE, Figure 3.7 – (g). Without removing the PR, the dies are exposed for 4 hours of O_2 plasma for release purposes, Figure 3.7 – (h).

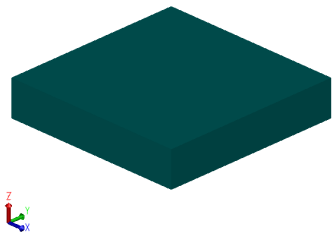

(a) Plain wafer.

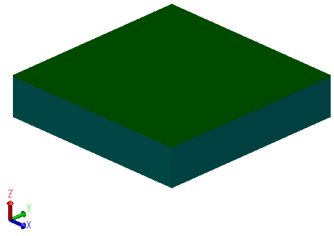

(b) Plain wafer is deposited with 200nm of Si_3N_4 for electrical isolation purposes.

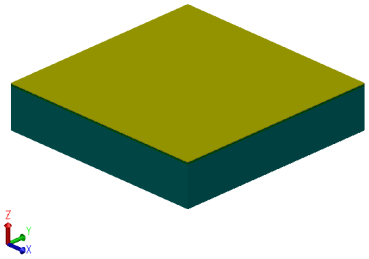

(c) Au layer of 100nm is deposited over a 25nm Ti adhesion layer. The thickness of Au is much longer than the skin depth of the Au in (2-20) μm IR range.

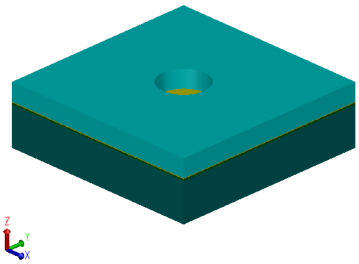

(d) Sacrificial layer of 2.0μm is spun over the Au layer and patterned via RIE process to form the post, holding the umbrella structure.

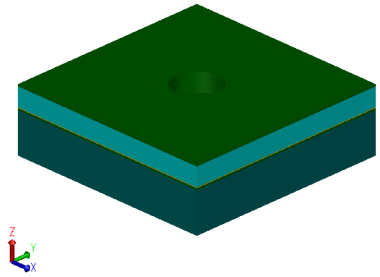

(e) The first nitride layer of 200nm thickness for the umbrella structure is deposited over the patterned sacrificial layer through PECVD, Figure 3.7 (continued).

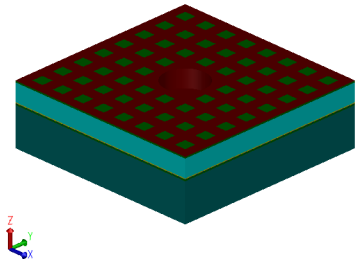

(f) Previously optimized NiCr layer with 90 seconds deposition time is deposited via Sputtering and patterned over the first nitride layer of the umbrella structure through Inverse Sputtering, Figure 3.7 (continued).

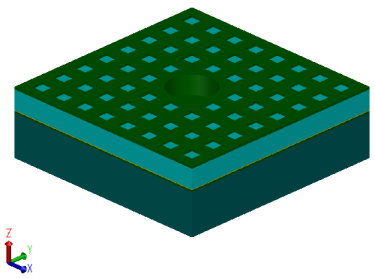

(g) Second nitride layer of 50nm thickness for the umbrella structure is deposited over the patterned NiCr layer via PECVD and patterned simultaneously with the first nitride layer through RIE.

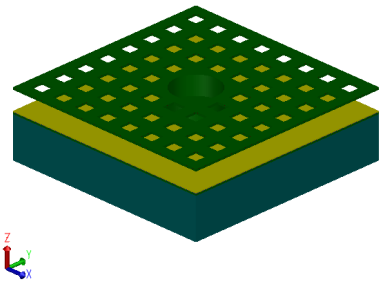

(h) The whole structure is released with O_2 plasma; i.e., the sacrificial layer is etched away.

Figure 3.7: Process flow of the canonical perforated umbrella structures from plain wafer up to the release of the suspended structures (a-h). With this process flow, various sizes of pixel pitches, 12µm, 17µm, 25µm and 50µm with various sizes of perforations from 0.5µm to 3.0µm are optimized, produced and tested.

Figure 3.8 summarizes the critical process steps with SEM images. The etching of the sacrificial PI2610 layer is done with an RIE exposure of 70 minutes for 2.0µm, Figure 3.8 – (a), what is observed here is only the PI layer, after both the hard mask and the soft masks are removed. The same layer can also be realized with Level M10, this material has a shorter release time (30 minutes for 2.3µm), while the PI layer needs around 4 hours for release. The next critical step is the etching of the NiCr wideband absorbing layer. Actually, in a generic process since all dies will have this layer, there is no need to etch this layer separately. RIE process can etch all umbrella layers, the top, bottom nitrides and the NiCr layer simultaneously with one soft mask. Since the NiCr layer is quite thin, the RIE can handle it. However, in this process, since there is a differential analysis planned for the 'with NiCr' and 'without NiCr' cases to confirm the wideband absorbing characteristics of the NiCr layer, there is also a need to etch the absorbing layer separately, Figure 3.8 – (b). However, in turn, this effort results in severe side sputtering problems, some sort of contamination, due to the separate etching of the NiCr layer. Next, the SEM image of the pixels after the nitride RIE, the PR is still on, is shown, Figure 3.8 – (c). As it is mentioned before, the RIE is used to etch both the top protective nitride and the bottom nitride of the umbrella structure simultaneously. Next SEM image, Figure 3.8 – (d), belongs to the pixels after the release is done without removing the soft mask (PR).

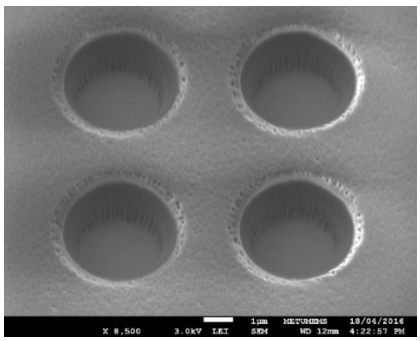

(a) SEM image of a 4-post case after the sacrificial layer patterning, both soft and the hard masks are removed.

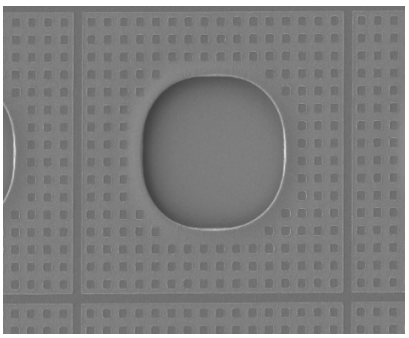

(b) SEM image of a 1-post case for 50µm pixel pitch size after the NiCr patterning through Inverse Sputtering (IS).

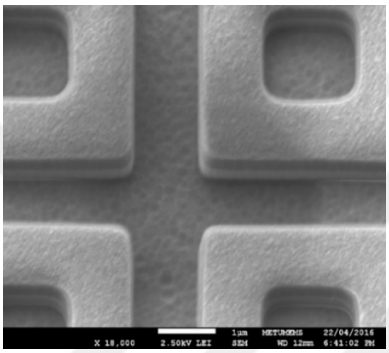

(c) SEM image of the patterned sandwiched umbrella structures. The PR is still not removed.

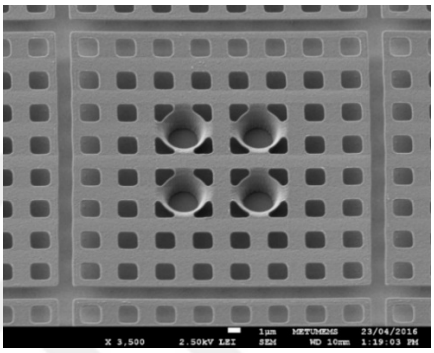

(d) SEM image of a 4-post suspended perforated umbrella structure after the release.

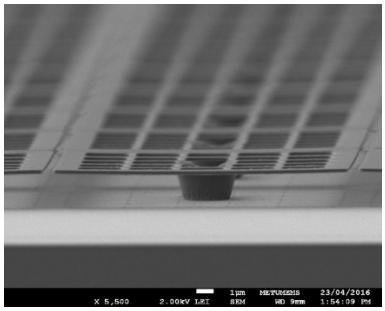

(e) A cross-view SEM image of a suspended perforated umbrella structure after the release.

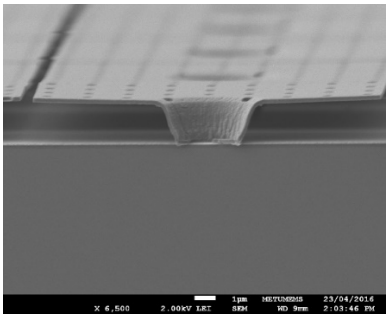

(f) A side-view SEM image of a suspended perforated umbrella structure after the release.

Figure 3.8: The SEM images of some critical steps for the process flow of the perforated umbrella structures; RIE of the sacrificial layer (a), etching of the absorbing layer (b), RIE of the umbrella nitride layers (c) and the release of the pixels (d). The sacrificial material with this run is PI2610 but satisfying results are also obtained with Level M10, another sacrificial material tested with these runs.

As it is mentioned previously, separate etching of the NiCr layer is problematic. Figure 3.9 summarizes the tested recipes to solve the problem, to optimize the pattering of the NiCr layer. This optimization had to be done since O_2 plasma or SVC (a chemical used to remove PR) cannot be used to completely strip the PR over the NiCr layer. Direct O_2 plasma exposure damages the thin NiCr layer and degrades its absorption performance and SVC will damage the Level M10 sacrificial layer. The last trial with flood exposure seems fine enough to get meaningful FTIR measurement results, still there is a side sputtering issue of NiCr layer though. Through measurements, it is shown that there is no any noticeable effect of this level of contamination on the absorption performance when they are compared with the simulation results. With the optimized recipe, Ultra-I (thickness of 700nm) is used as the PR since it is expected that a thinner PR will reduce the side-sputtering problem. The lithography is done with ASML stepper. Develop is done with the MF24A chemical, etching of the NiCr layer is done with the Inverse Sputtering with an exposure time of 25 seconds.

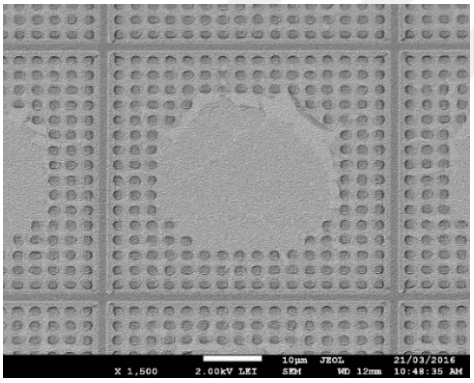

(a) SEM image of NiCr layer after Inverse Sputtering with S1813 @3k rpm + Descum + Acetone recipe, Figure 3.9 (continued).

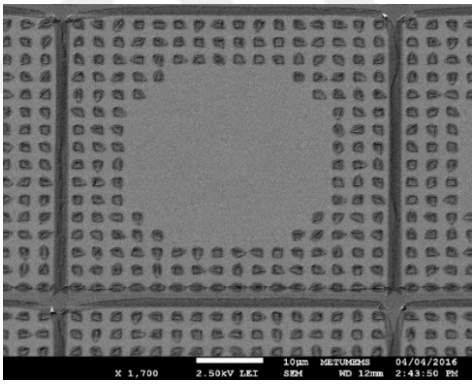

(b) SEM image of NiCr layer after Inverse Sputtering with SPR220-3 @4k rpm + Descum + Acetone recipe, Figure 3.9 (continued).

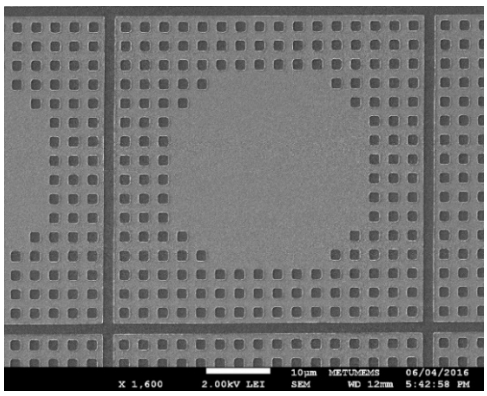

(c) SEM image of NiCr layer after Inverse Sputtering with Ultra-i @3k rpm after + PR Strip (3min) + Flood Exposure + MF24A Developer + Acetone recipe.

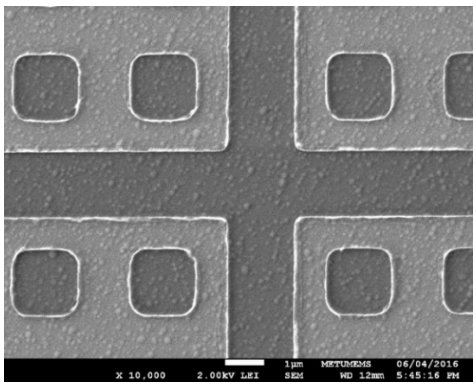

c) SEM image of NiCr layer after Inverse Sputtering with Ultra-i @3k rpm after + PR Strip (3min) + Flood Exposure + MF24A Developer + Acetone recipe.

Figure 3.9: SEM images belonging to various recipes of NiCr patterning. To make a differential comparison between the w/ NiCr and w/o NiCr cases, the NiCr layer should be etched separately. This optimization had to be done since O_2 plasma or SVC cannot be used to completely strip the PR. O_2 plasma will damage the thin NiCr layer and SVC will damage the Level M10 sacrificial layer. The last trial with flood exposure seems fine enough to get meaningful FTIR measurements, still there is a side sputtering of NiCr layer though.

Then the PR is softened with a PR Strip recipe (high RF power, high chuck temperature) for 3 minutes (better if it is increased). Flood exposure is done with the Aligner with an exposure time of 40 seconds to weaken the PR more, then another MF24A develop is applied. There might be a need to apply an acetone recipe as a last attempt or not, which can be decided by observing the PR residuals left behind after the Develop.

Figure 3.10 shows the SEM images of a successful implementation of the process flow just described above. All four cases; “with Perforation”, “without Perforation”, “with NiCr” and “without NiCr” for a specific type of pixel are shown. The ones with the NiCr layer are quite noticeable due to the side sputtering residuals at the edges of the pixel.

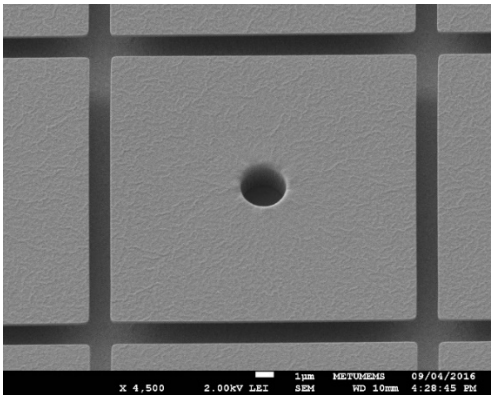

(a) SEM image of a pixel with "w/o Perforation" and "w/o NiCr" Layer case.

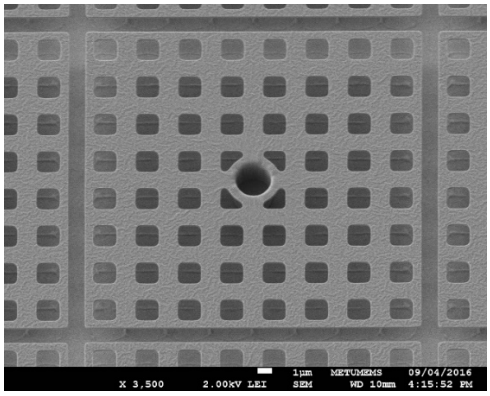

(b) SEM image of a pixel with "w/ Perforation" and "w/o NiCr" Layer case.

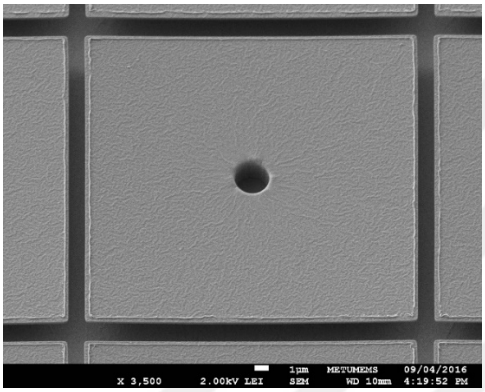

(c) SEM image of a pixel with "w/o Perforation" and "w/ NiCr" Layer case.

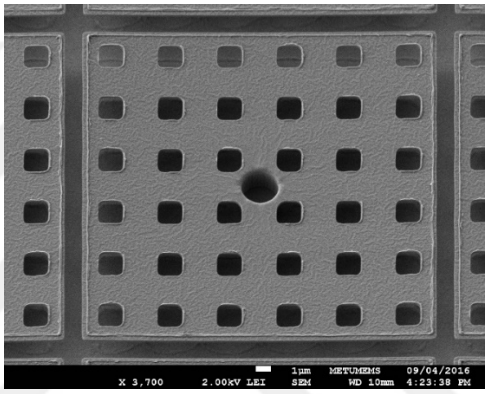

(d) SEM image of a pixel with "w/ Perforation" and "w/ NiCr" Layer case.

Figure 3.10: SEM images of all four cases; "with Perforation", "without Perforation", "with NiCr" and "without NiCr" for a specific type of pixel. With separate etching of the NiCr layer it is possible to make a differential analysis to examine the effect of the perforation and the NiCr layer on the absorption performance.

Canonical perforated umbrella structures are composed of Au reflector layer, an air gap of around 2.0µm, and suspended umbrella structures sandwiching a thin NiCr absorbing layer. The process involves the optimization of the sacrificial layer materials and patterning related processes such as lithography and etching of the individual layers. Four processes are finalized (labeled as P1, P2, P3 and P4). P1 was a dummy process just to have a rough idea about the process parameters. Measurable devices are manufactured with P2, P3 and P4. All processes are optimized to have an air gap of 2.0µm, an umbrella nitride thickness of totally 250nm and 100nm Au reflector layer. Different processes are examining different etching configurations

such as simultaneous etching or separate etching of all umbrella layers and different sacrificial material usage, such as LM10 and PI2610. The mask is designed in such a way that a differential analysis can be done between the cases with NiCr layer deposited or not and the umbrella layers are perforated or not. The simulation results state that to ensure the high absorption, independent of the period size, if a perforation percentage of 50%, (i.e.; (Perf. Size) / (Period Size) =0.5) is achieved, the highest absorption rate for the proposed canonical topology is obtained. To test the results of the simulations, various processes are finalized, examining the various period sizes and perforation sizes changing the perforation percentage to conduct a controlled experiment. The controlled experiment means that there are pixels presenting both bad and good absorption performances intentionally. With Process #2 (P2), Level M10 is used as the sacrificial layer, the NiCr layer is etched separately with Inverse Sputtering different from the nitride layers which are etched with RIE. Thus the effect of the NiCr layer on the absorption performance can be measured differentially. Process #3 (P3) uses PI2610 as the sacrificial layer. This material is the usual sacrificial layer which is used in the METU MEMS facility, which has a way longer release time than the Level M10 material. NiCr layer is also etched separately with this run. Process #4 (P4) also uses the Level M10 material as the sacrificial layer, but all umbrella layers; top, bottom nitride layers and the NiCr layer are etched simultaneously with RIE. Thus if there is any performance degradation with separate etching of the NiCr layer, it can be observed. With the last process NiCr layer is not exposed to any etching process, but protected by both the top and the bottom nitride layers. Figure 3.11 shows some of the successfully released pixel topologies belonging to Process #2. Although the process is not as clean as P3, as it will be observed with the next section, absorption performances are not affected with the contamination that much. Table 3-2 shows the difference between the design and the measurement for perforation sizes since the post-process feature sizes may affect the absorption performance. The period size and the post size are not affected by lithography or process-to-process variations that much. However, the measured values for perforation size are larger than the designed ones which can be fixed to some extent by optimizing the lithography.

Table 3-2: A summary of measured and designed topology parameters for different processes and different size of pixel pitches. All C-series (C9, C14, etc.) belong to 25µm and B-series (B8, B14, etc.) belong to 17µm pixel pitch sizes. There is a noticeable difference with the Post Sizes which actually does not affect the absorption performance much, nevertheless good agreement with the Period Size is observed. However there is noticeable over-etching problem observed with the Recess Size differences which will affect quite the absorption performance. I can optimize it with a few optimization trials with the lithography.

Period Size (µm)	Perf. Size (µm)	
	Designed	Measured
3.0	2.5	2.8
3.0	2.0	2.2
3.0	1.5	1.7
3.0	1.0	1.2
2.0	1.0	1.2
2.0	0.5	0.6

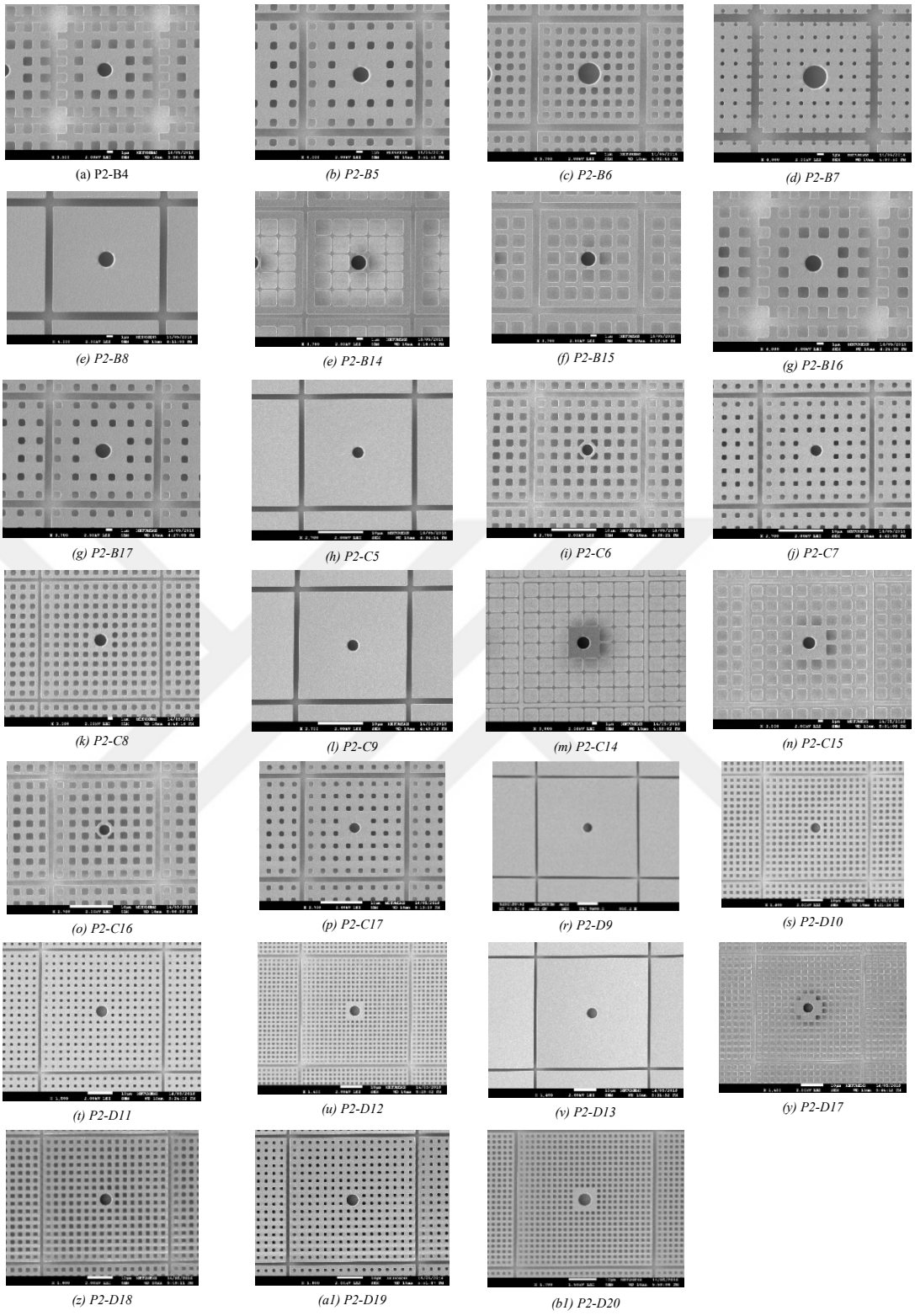

Figure 3.11: SEM images of successfully released perforated umbrella configurations used in FTIR measurements. These configurations belong to P2 process with 17 µm (P2-B Series), 25µm (P2-C Series) and 50 µm (P2-D Series) pixel pitches. This process is realized with the LM10 as the sacrificial layer and the NiCr layer is separately etched. Also with this process, there is a side-sputtering problem with the etching of the NiCr layer.

3.3 A Comparison of the FTIR Measurement versus HFSS Simulation Results

FTIR (Fourier Transform Infrared Spectroscopy) measurements were done with Bruker brand Hyperion 3000 device at Bilkent UNAM facility. The device is employed in reflection mode, the calibration for reflection is done with a 100nm Au samples prepared at METU MEMS facility. The device has a modular microscope with which the IR beam can be focused into a specific configuration desired, which is quite vital for the measurement of bolometer related samples. What an FTIR does is to measure how well a sample absorbs light at each wavelength; i.e., to measure spectral response. The most known technique to measure spectral response is "dispersive spectroscopy" technique. With this technique, the absorbed light is measured by the sample while a monochromatic beam is incident upon it and the same measurement is repeated for each f other wavelengths of concern. This is actually how UV-Vis spectrometers work. On the other hand, with FTIR technique, a beam containing many frequencies of light is incident upon the sample, then the absorbed light is measured. Next, the beam is modified to shine a different combination of frequencies upon the sample, which gives a second data point. With a special algorithm, by blocking some of the frequency components and obtaining many data points actually the Fourier transform of the absorption response belonging to the sample can be obtained.

Figure 3.12, Figure 3.13 and Figure 3.14, all show FTIR measurement results belonging to the P2, P3 and P4 respectively. With those measurements, the spectral response of pixels having different pixel pitches 12µm, 17 µm, 25µm and 50µm for different processes are examined. Each figure also contains "with NiCr" and "without NiCr" cases. Pixels employing NiCr as the absorbing layer introduces a wide band absorption characteristic to the quarter wave resonance topologies as simulated. "with NiCr" case also contains various perforation percentages which is actually the focus of this study.

Figure 3.12 shows the FTIR measurement results belonging to Process #2 (P2). With this process, there are measurement results for 17 µm, 25µm and 50µm pixel pitches. The sacrificial layer is implemented with Level M10. The NiCr layer is etched

separately from the umbrella nitride layers. This process has a severe side-sputtering problem introduced by the NiCr layer.

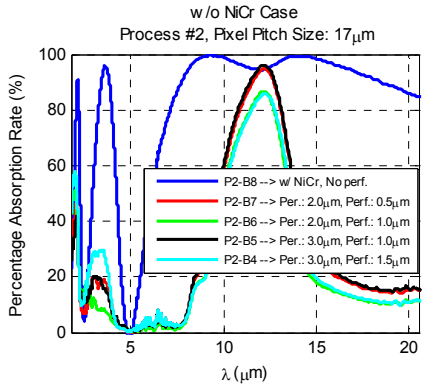

(a) P2-B Series: 17μm Pixel Pitch Size, w/o NiCr Layer Case.

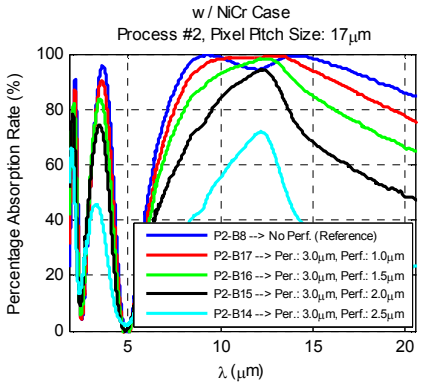

(b) P2-B Series: 17μm Pixel Pitch Size, w/ NiCr Layer Case.

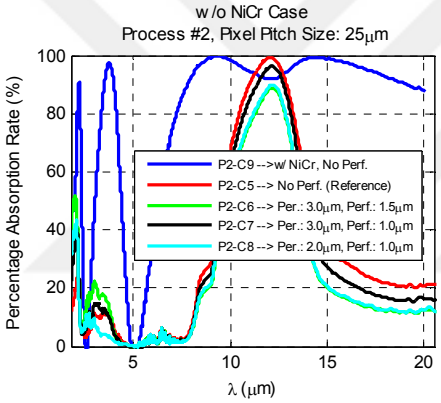

(c) P2-C Series: 25μm Pixel Pitch Size, w/o NiCr Layer Case, Figure 3.12 (continued).

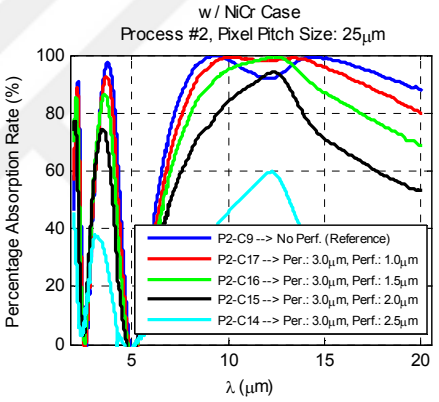

(d) P2-C Series: 25μm Pixel Pitch Size, w/ NiCr Layer Case, Figure 3.12 (continued).

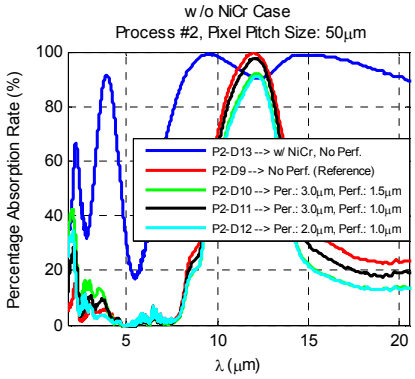

(e) P2-D Series: 50μm Pixel Pitch Size, w/o NiCr Layer Case.

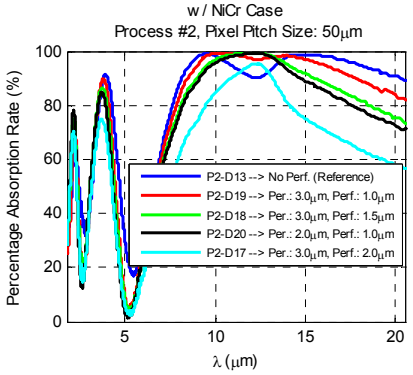

(f) P2-D Series: 50μm Pixel Pitch Size, w/o NiCr Layer Case.

Figure 3.12: These FTIR measurement results belong to the Process #2 (P2) for various pixel pitch sizes; 17μm, 25 μm and 50μm. This process is realized with LM10 as the sacrificial layer and also has a severe side sputtering problem regarding the inverse sputtering of the NiCr layer, but still the results are satisfying. All these results verify the fact that while the w/ NiCr case presents a broadband characteristic, the w/o NiCr case presents a narrow band, λ/4 resonance characteristic for the absorption performance. Also, as the perforation size exceeds the 50% of the period size, a degradation in absorption performance is observed.

Figure 3.13 shows the FTIR measurement results belonging to Process #3 (P3). With this process, there are measurement results for 12 μm, 17μm and 25μm pixel pitches. The sacrificial layer is implemented with PI2610. This process has a severe side-sputtering problem introduced by the NiCr layer. Severe side-sputtering problem with this process is revealed by increasing the PR strip duration after the Inverse Sputtering.

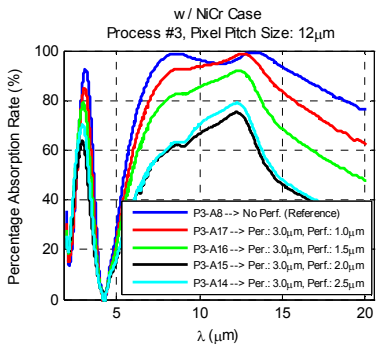

(a) P3-A Series: 12μm Pixel Pitch Size, w/ NiCr Layer Case, Figure 3.13 (continued).

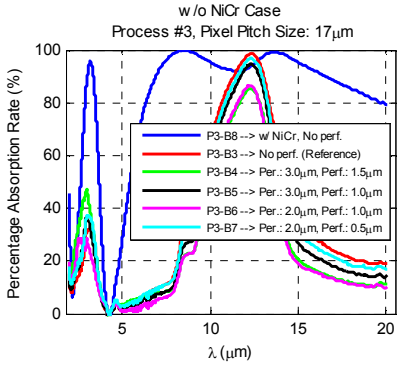

(b) P3-B Series: 17μm Pixel Pitch Size, w/o NiCr Layer Case.

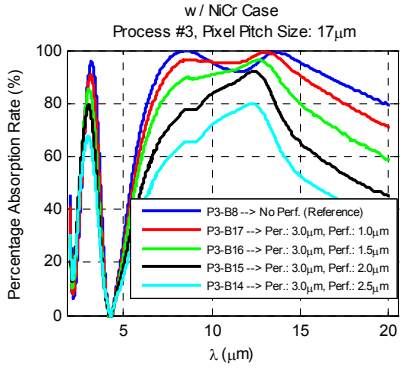

(c) P3-B Series: 17μm Pixel Pitch Size, w/ NiCr Layer Case.

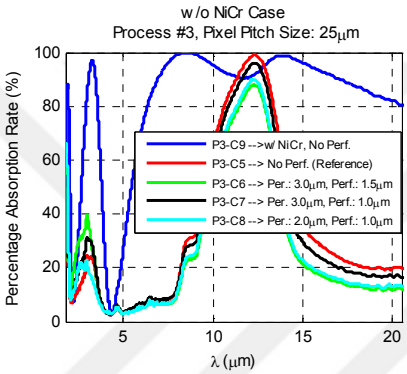

(d) P3-C Series: 25μm Pixel Pitch Size, w/o NiCr Layer Case.

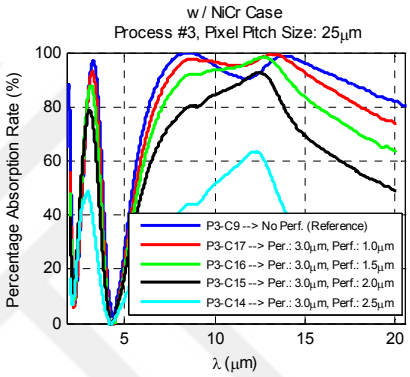

(e) P3-C Series: 25μm Pixel Pitch Size, w/ NiCr Layer Case.

Figure 3.13: These FTIR measurement results belong to the Process #3 (P3) for various pixel pitch sizes; 12μm, 17 μm and 25μm. This process is realized with PI2610 as the sacrificial layer and also has a severe side sputtering problem is relieved with this process. All these results verify the fact that while the w/ NiCr case presents a broadband characteristic, the w/o NiCr case presents a narrow band, λ/4 resonance characteristic for the absorption performance. Also, as the perforation size exceeds the 50% of the period size, a degradation in absorption performance is observed.

Figure 3.14 shows the FTIR measurement results belonging to Process #4 (P4). With this process, there are measurement results for 12 μm, 17μm and 25μm pixel pitches. The sacrificial layer is implemented with Level M10. With P4 process, the NiCr layer is simultaneously etched with the nitride layers through RIE method, which means that NiCr layer is protected during the etching by the nitride layers.

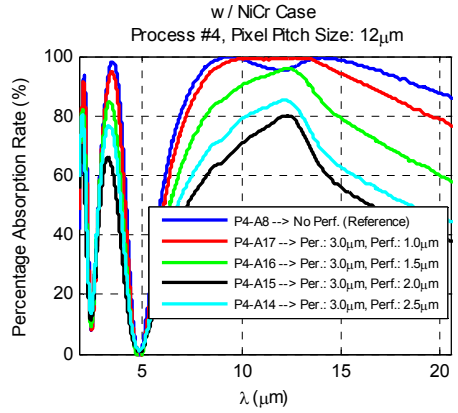

(a) P4-A Series: 12μm Pixel Pitch Size, w/ NiCr Layer Case.

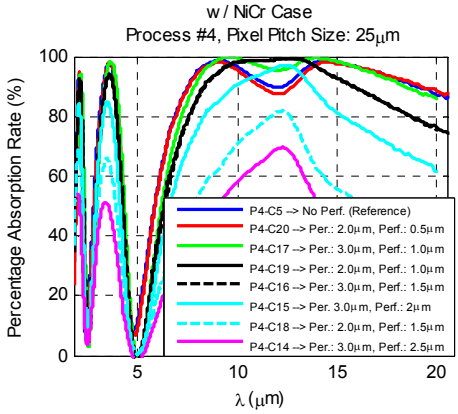

(b) P4-C Series: 25μm Pixel Pitch Size, w/ NiCr Layer Case.

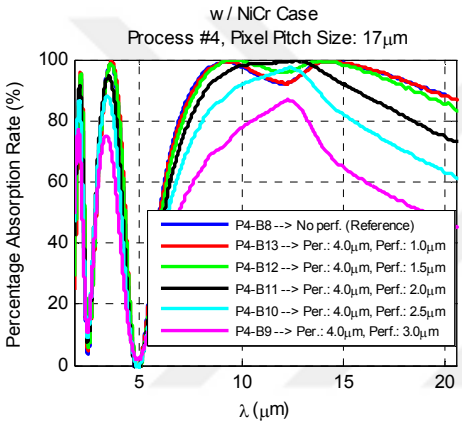

c) P4-B Series: 17μm Pixel Pitch Size, w/ NiCr Layer Case, Period Size → 4.0μm.

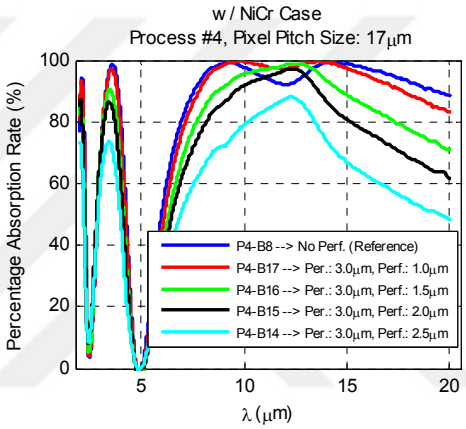

(d) P4-B Series: 17μm Pixel Pitch Size, w/ NiCr Layer Case, Period Size → 3.0μm.

Figure 3.14: These FTIR measurement results belong to the Process #4 (P4) with various pixel pitch sizes, 12μm, 17μm and 25μm and w/ NiCr case. P4 is also realized with the LM10 sacrificial layer material. With this process, all umbrella layers are simultaneously etched, which means that the NiCr layer is protected during the etching processes. These results also verify that as the perforation ratio increases, at some point (~50%), a degradation with the absorption performance is observed. With P4, observations for different period sizes are also made to verify the 50% perforation rate as the optimum value, it also checked out with the HFSS simulation results.

Figure 3.15 shows the FTIR measurement results for "Not Perforated" cases. For the very same topology, we are observing the effect of process to process and pixel to pixel variations on the absorption performance. The result is quite satisfying, despite to the many process related variations, the absorption characteristics are confined in a band for both "with NiCr" and "without NiCr" cases.

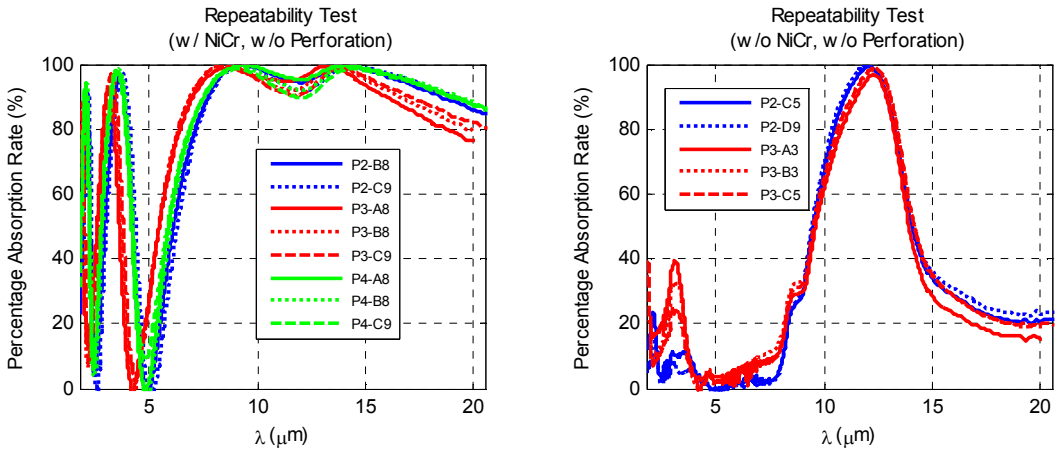

(a) w/ NiCr, w/o Perforation case for various pixels on different processes.

(b) w/o NiCr, w/o Perforation case for various pixels on different processes.

Figure 3.15: FTIR measurement results regarding the examination of the undesired process variations, such as air gap thicknesses, on the desired absorption performance for (w/ NiCr, w/o Perforation) and (w/o NiCr, w/o Perforation) cases, for various pixel pitch sizes and the processes. A cumulative effect of all undesired process related variations on the absorption performance in all IR range is observed o. The effect is more noticeable on the MWIR (3-5) μm range than on the LWIR range (8-12) μm, still not bad results.

Previous section explained for the FTIR measurement results for various processes and pixel pitch sizes with various perforation schemes implemented on them. The question is now how controlled was the fabrication. To evaluate the situation, there is also a comparison between the measurement and the HFSS simulation results. The comparison is done for the field distribution over the "Not Perforated" cases. The fitted data for the field is obtained through a comparison between the FTIR measurement results and the CTL technique results. The fitting is done for the meaningful part (high absorption) of the measured band to avoid the inherently coming measurement errors. The first two-dimensional fitting trial is done for the suspended pixels composed of only nitride layers; i.e., does not contain the sandwiched NiCr layer. Thus, both the air gap thickness and total umbrella nitride thickness can be obtained without considering the sheet resistance of the NiCr absorbing layer. Figure 3.16 shows the regarding results, belonging to the suspended nitride layer. The air gap thickness is fitted to 2.3μm and total nitride layer is fitted to 190nm both of which can be confirmed through cross-sectional SEM inspection.

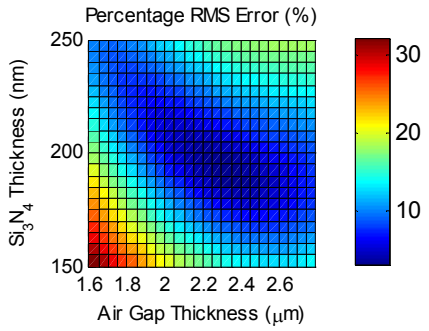

(a) Two dimensional optimization graph for suspended umbrella w/o NiCr.

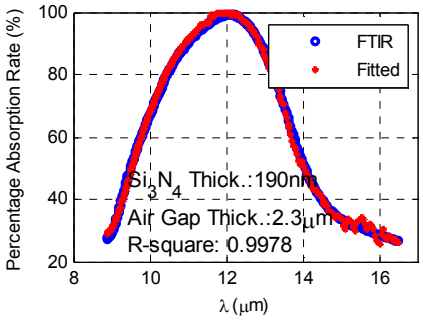

(b) LWIR band optimization results.

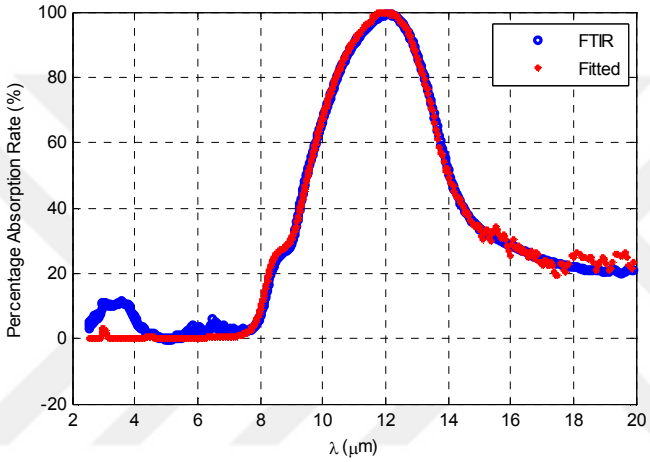

(c) Full band comparison of both the fitted CTL code and the FTIR measurement results. Since high frequency part of the band is noisy it is disregarded during optimization.

Figure 3.16: The simultaneous optimization results of both the umbrella nitride thickness and the air gap thickness through CTL code. The aim function is the FTIR measurement results. The air gap is fitted to 2.3μm, which is actually the optimized thickness during the sacrificial layer process optimizations. The nitride thickness is fitted to 190nm, which is actually quite different from the common knowledge used in the recipes it should have been (200+50) nm for both the top and the bottom nitrides. Nevertheless both results are verified through SEM inspection by observing the cross section of the layers. The total nitride layer thickness is actually measured around 190nm.

Figure 3.17 shows the optimization results for the pixels containing wide band absorbing NiCr layer. By using the air gap thickness obtained through the first fitting trial, a three variable fitting can be done; containing the bottom, top nitride layer thicknesses and the sheet resistance of the NiCr layer as the fit parameters. The fitted value for the nitride layer is (160nm + 20nm) and the fitted value for the sheet resistance is 460Ω/□. For this trial, there is a measurement error for the aim function;

i.e., FTIR measurement, around 5µm, which is also disregarded from the range used for the optimization. Both fitted values can also be verified through previous optimization trials.

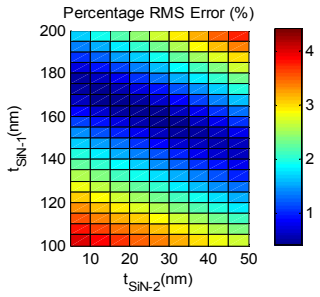

(a) Two dimensional optimization graph for suspended umbrella w/ NiCr.

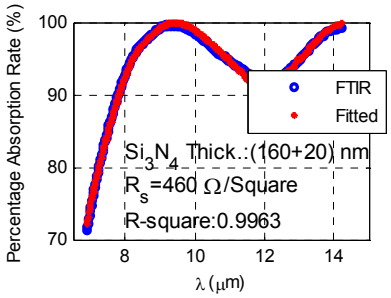

(b) LWIR band optimization results.

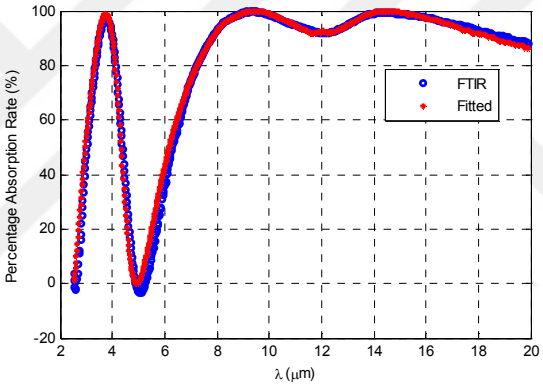

(c) Full band comparison of both the fitted CTL code and the FTIR measurement results.

Figure 3.17: The simultaneous optimization results of both the top and the bottom umbrella nitride thicknesses through CTL code. For the optimization the LWIR band values are used The aim function is the FTIR measurement results. The air gap is 2.3µm and the total nitride thickness should be around 190nm from the previous optimization results. A three variable fitting also predicts the sheet resistance around 460Ω/□. This value can also be verified with the previously done NiCr layer optimizations. The nitride layer thickness is fitted to (160+20) nm which is not far from 190nm.

Figure 3.18 shows one of the critical results obtained through these processes regarding the perforation rate. The larger the perforation size, the better the thermal performance and vacuum performance. However, how large the perforation size should be without losing from the IR absorption performance is the issue. Through HFSS simulation results it is observed that 50% perforation ratio is an optimized

value for not losing from the IR absorption performance, even for some configurations, this value means an increase in the IR absorption rate.

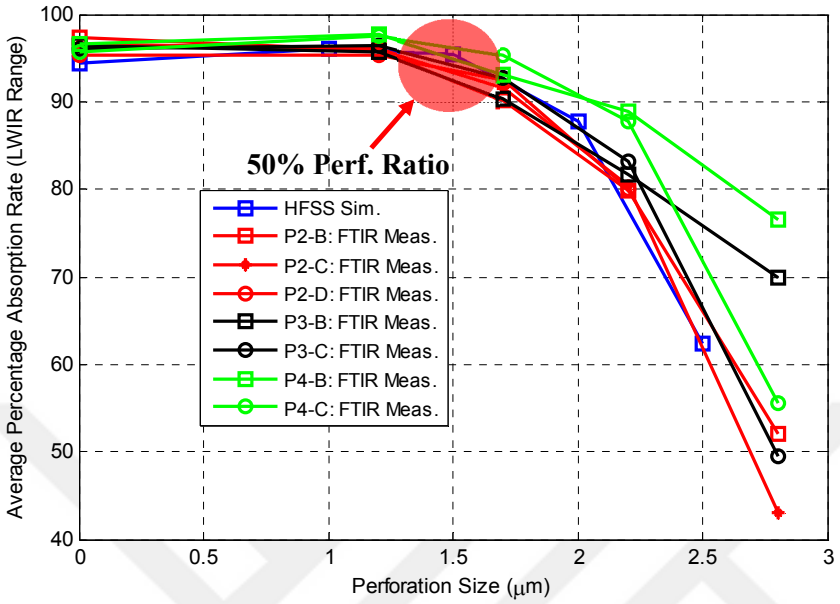

Figure 3.18: A comparison of the HFSS simulation results with the FTIR measurement results regarding the dependency of the absorption performance on the perforation sizes (duty cycles) for the w/ NiCr cases. The measurements are collected from all three processes and various pixel pitch sizes for the same period size, 3μm. All those results show that 1.5 μm perforation size for 3.0μm period size (50% Perf. Rate) is the limit to prevent any degradation with the absorption performance. The contamination can be blamed for the deviations of the FTIR measurement results from the HFSS simulation results for the larger perforation sizes.

Figure 3.19 shows the FTIR vs. HFSS simulation results for different period sizes, 3μm and 4μm. Both cases verify the 50% perforation rate. In this figure the focus should be on the breakpoint value where the absorption performance starts to degrade instead of the individual absorption rate values.

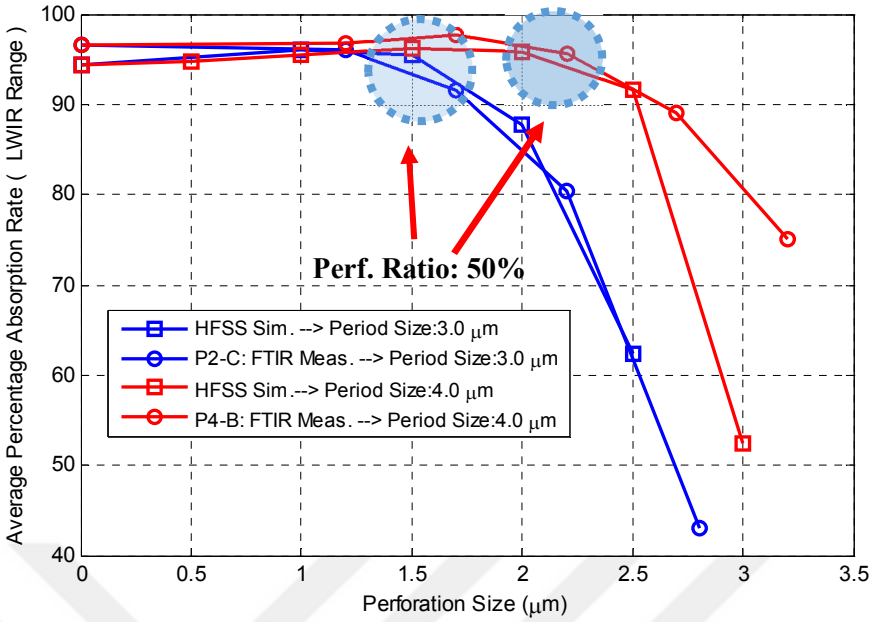

Figure 3.19: A comparison of the HFSS simulation results with the FTIR measurement results regarding the dependency of the absorption performance on the perforation sizes (duty cycles) for the w/ NiCr cases and for different period sizes. All results show that 1.5 μm recess size for 3.0μm period and 2.0 μm for 4.0 μm (50% duty cycle) period is the limit to prevent any degradation with the absorption performance, which was already predicted by the HFSS simulations.

To sum up, through both HFSS simulation results and the FTIR measurement results, the following results are verified. First, the results show that the NiCr layer is successfully modelled with a simple non-dispersive scheme. Second there is a limit value for the perforation size; i.e., it is not true that the larger the perforation size, the better the performance. The perforation size should not exceed 50% of the period size. Another result underlines the fact that this optimum perforation ratio is independent of the pixel pitch sizes, the period sizes, and umbrella nitride thicknesses.

3.4 Application of Perforation on High Performance Pixels

3.4.1 IR Absorption Performance

Optimizations regarding the perforation have been done in the previous sections with the canonical topology which involves only the umbrella and the post structure. In

this section, there are results of direct application of the optimized structures to the full pixel structures which include both the body nitride and the arm structures different from the canonical topology. Figure 3.20 shows the SEM images of application of the perforation to the 17µm pixels. These pixels are two sacrificial layer structures. In the first level, there are the supporting legs and the active material, in the second one, the umbrella is placed on. The air gap thickness is around 1.0µm for each level; however the non-conformal deposition changes the math a little.

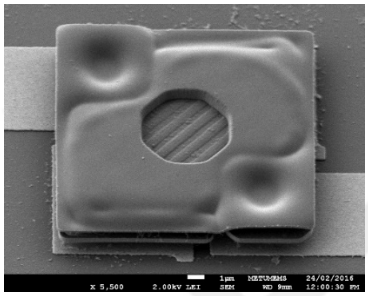

(a) SEM image of suspended 17µm single pixel without perforation.

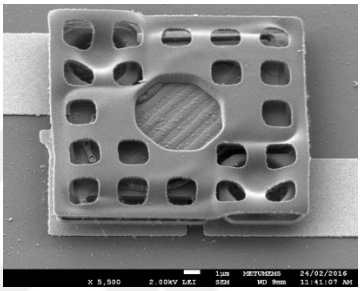

(b) SEM image of suspended 17µm single pixel with perforation.

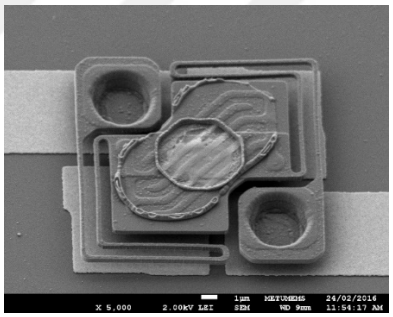

(c) SEM image of the structures underneath the umbrella layer. The umbrella is separated away.

Figure 3.20: SEM images of 17µm single pixel structures produced at METU MEMS Center by Eren Canga. Single pixel consists of mainly the active material, supporting legs and umbrella structure.

Figure 3.20 shows the FTIR results belonging to the 17µm, high performance pixel arrays with and without perforation. A differential analysis is done to observe the effect of the 50% perforation. The result is as expected, the absorption characteristics is not disturbed much. Process variations or measurement errors can be blamed for the difference.

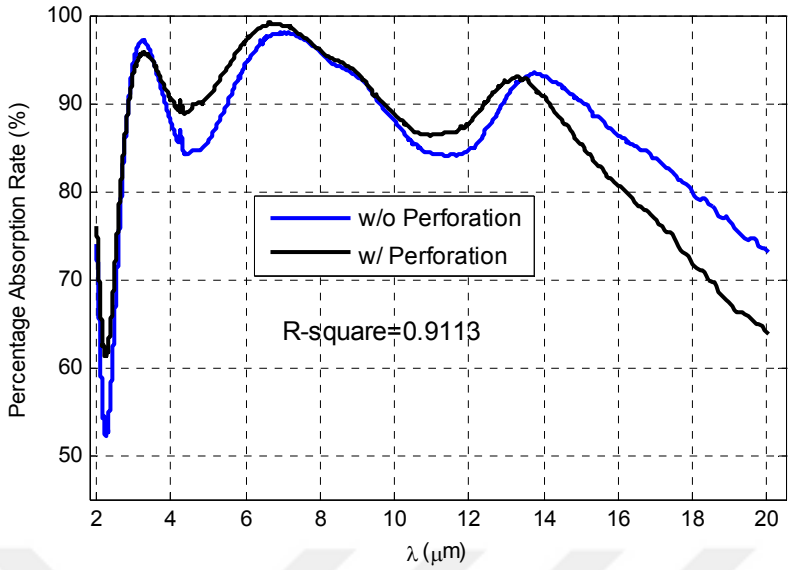

(a) Sample-1.

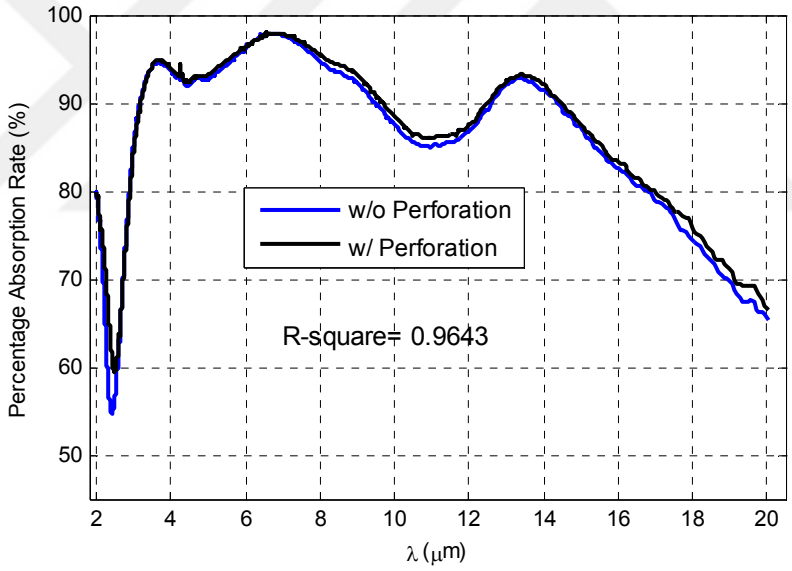

(b) Sample-2

Figure 3.21: FTIR absorption measurement results of both "not perforated" and "perforated" cases belonging to two samples (Sample-1, 2) of 17μm pixel arrays. Average absorption rate in LWIR range is measured to be around 90%. The perforation rate is around 50%; i.e., the period size is 3.0μm and the perforation size is 1.4μm. The problematic etching with the active material can be blamed for the relatively bad result with Sample-2. Also the absorption rate can still be increased by tuning the air gaps, thus shifting the maximum absorption in the figures to the LWIR range. Due to non-conformal deposition of the sacrificial layer with this process run, there is still a need for fine tuning of the air gap thicknesses. Nevertheless, both measurements prove the optimized 50% perforation ratio to prevent the absorption performance from degradation.

3.4.2 Thermal Simulations

One of the aspects foreseen with application of the perforation was an improvement through Thermal Time Constant (TTC). Since the total thermal mass will decrease through perforation, thermal capacitance will also decrease, in turn, improving the TTC. Nevertheless, the thermal capacitance is not the only parameter affecting the TTC, thermal resistance should also be considered. There is a trade-off between the time constant and the thermal isolation performance. If you manage to increase the thermal resistance, the isolation will be better and in turn, for the same amount of incident IR power, the voltage readings from the pixel will be higher, which is good. However, for the same amount of thermal mass, this will also increase the TTC which is bad. As the pixel pitch size is reduced, one of the challenges would be to prevent the thermal isolation performance from getting worse. Keeping it at the same level will also be a success. In such a scenario, you will also be able to create thinner arm and body nitride which can keep the whole structure mechanically still intact. Then, the effect of the perforation on TTC will be more noticeable. Figure 3.22 and Figure 3.23 show the results of such a scenario for 25µm pixels by using differential analysis.

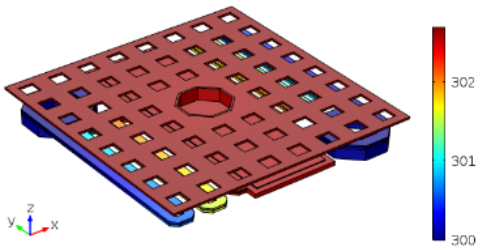

(a) Spatial temperature distribution over the full pixel structure at the steady state.

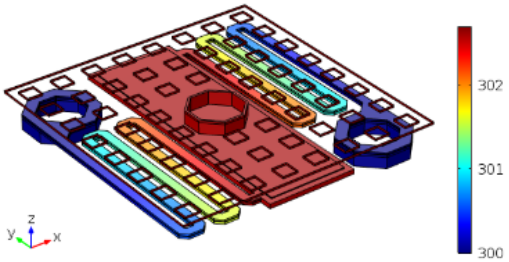

(b) Spatial temperature distribution over the full pixel structure at the steady state. The umbrella is made transparent for better observation of the temperature distribution for the underneath structures

Figure 3.22: Transient Thermal simulation results for a 25µm pixel with perforated umbrella structure. The total body nitride thickness is 100nm, so the arms are. In reality, this much of arm thickness cannot hold the whole structural layers, nevertheless, to prove our point with the perforations through simulations, this thickness is still acceptable. The image is taken at the steady state. The final maximum temperature difference is about 2.6K. The perforated umbrella and the active material are heated as expected and the arms are isolating the hot spots from the ROIC part as expected. The simulation results are generated by COMSOL Multiphysics.

Figure 3.23 shows the transient thermal analysis results for 25µm pixels for different thicknesses of body nitrides and for various perforation rates. The results show that for the topology suggested with Figure 3.22, the improvement with the TTC is more than 10%. As the pixel dimensions get reduced and the thermal isolation performance is handled, I expect, it would be much better than those results.

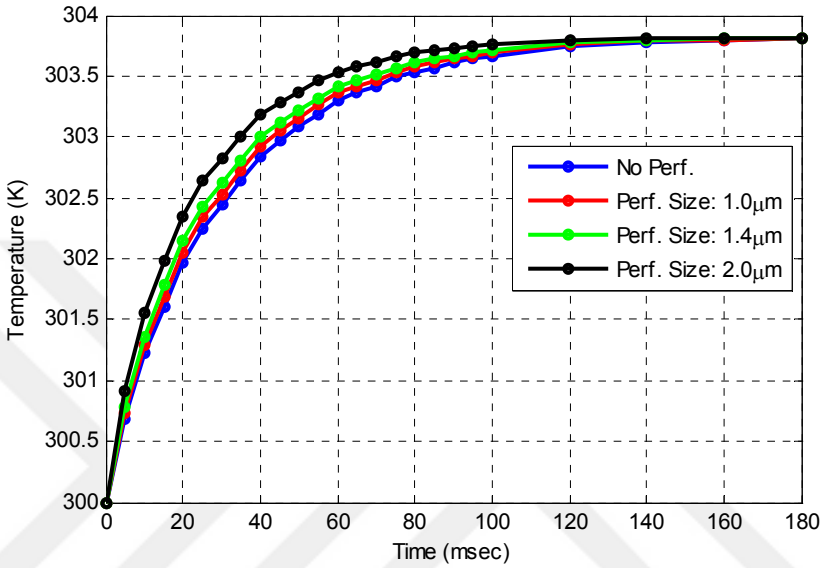

(a) Body nitride thickness is (50nm+50nm), Figure 3.23 (continued).

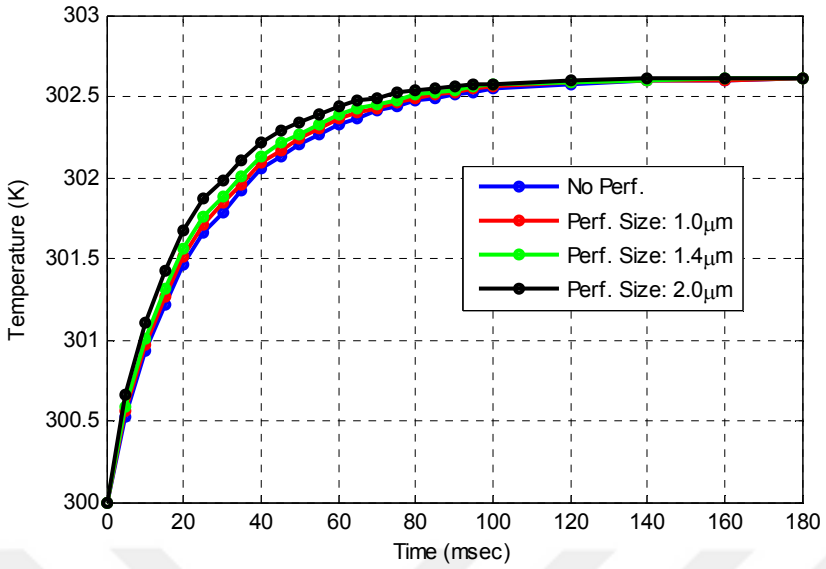

(a) Body nitride thickness is (200nm+200nm).

Figure 3.23: The Transient Thermal simulation results for two different body nitride thicknesses, 100nm and 400nm. Since the maximum temperature that 100nm case is larger than the other it can be deduced that the thermal isolation is better for the 100nm case. Graphically, the performance improvement with the thermal time constant due to perforation can also be easily observed.

Table 3-3 shows the tabulated TTC data for the previously proposed configurations to test the effect of the perforation on the TTC performance. An improvement more than 10% is expected with the employment of the perforation on the umbrella layers.

Table 3-3: Tabulated simulation data for the thermal time constant (TTC) of 25μm pixels with umbrella structures for different body nitride thicknesses and for various perforation rates. Simulations suggest that there is an improvement by 10% to 16% with the thermal time constant for a 50% perforation rate. The period size is 3.0μm.

	Thermal Time Constant (TTC, msec)	
	Body Nitride Thick.:100nm	*Body Nitride Thick.:400nm*
No Perforation	*29.2*	*24.7*
Perf. Size: 1.0 μm	*26.8*	*23.5*
Perf. Size: 1.4μm	*24.6*	*22.2*
Perf. Size: 2.0μm	*21.0*	*19.6*

In summary, within this section the FTIR measurement results are presented for the optimized perforation ratio, which is 50%, on full pixel structures. The result is as expected by the canonical topology; the absorption performance is kept intact although a reduction in the mass of the absorbing material. Secondly, thermal simulation results are presented to check if the TTC is improved as expected with the employment of the perforation. The results are promising and expected to be better as the pixel dimensions are reduced.

CHAPTER IV

CONCLUSION AND FUTURE WORK

This study examined the design, implementation, fabrication and functionality of the perforation on high fill factor structures for infrared sensors. First the motivation behind all these studies is explained after a summary of the previous studies in the literature that led us to this point. Then the benefits such as the absorption enhancement, improvements with thermal time constant, vacuum requirements and the etching performance through the implementation of the perforation are explained and some of them are examined through measurements and simulations. The perforation is applied to a topology where the active material layer and the high fill factor layer are separated away from each other within a finite distance. Thus, there emerges a need for the IR characterization of the sub-layers, Si_3N_4 and NiCr, forming the umbrella layer. A non-dispersive model for the NiCr absorbing material is proposed and the model is confirmed with the comparison of both the simulation and measurement results. During the optimization trials of the NiCr layer, a performance degradation by O_2 plasma exposure is also observed and verified through FTIR measurements, accordingly, the functionality of the cover silicon nitride is explained. Then with the employment of HFSS EM simulation program, the optimization trials regarding the dimensions of the perforation and the thickness of the umbrella layer on a canonical topology are performed. The canonical topology, which is selected as a free standing perforated umbrella structure, is employed to lower the simulation costs. A nice match between the HFSS simulations and FTIR measurement results for this canonical topology is observed. The optimized perforation ratio is advised to be around 50% to prevent any degradation with the absorption performance. Through FTIR measurements on the canonical topology, the wideband absorption characteristic, which is promoted with the inclusion of the resistive NiCr layer between the silicon nitride layers of the umbrella, is also verified by using differential analysis. The optimized value obtained from those studies is directly

applied to a high performance pixel topology. Again with the employment of differential analysis, no degradation regarding the absorption performance is observed through the implementation of the perforation. FTIR measurements also reveal that the absorption performance is around 90% in LWIR range for the tested high performance pixel topology. Lastly, with the application of the perforation, an improvement by more than 10% with the thermal time constant is observed via transient thermal simulations.

For the future work, the application of the perforation is also to be tested with low-cost detectors. However for low-cost type, it will not be possible to compare both the simulation and measurement results since there is no any reflector layer within the low-cost topology implemented at METU MEMS Center. If there is no any reflector layer, since there is no information for the IR characterization of the underneath CMOS layers, it will be impossible to simulate the whole structure correctly. However, a reflector layer placed in the topology would solve the problem. Actually the first studies in the literature involve such structures, thus this possibility can also be examined as a future work. Nevertheless, the perforation is still to be tested by employing differential analysis for the current topology. For the high performance detectors, a fully 3D EM simulation setup should be established instead of the employment of simpler canonical versions of it. Thus it would be possible to assess the effect of the each layer on the absorption performance of the detector pixels one by one. The responsivity of the pixels should also be measured under varying vacuum conditions for both high performance and low-cost detectors to prove the usefulness of the perforation. The feasibility of other metals such as Titanium (Ti), Titanium Nitrate (TiN) and Tungsten (W), which can be deposited at the METU MEMS Center, as the absorbing layer instead of the NiCr can also be examined.

REFERENCES

[1] P. W. Kruse, *Uncooled Thermal Imaging: Arrays, Systems, and Applications*. SPIE Press, 2001.

[2] A. Rogalski, "Infrared detectors: An overview," *Infrared Phys. Technol.*, vol. 43, no. 3–5, pp. 187–210, 2002.

[3] A. Rogalski, "Infrared detectors: Status and trends," *Prog. Quantum Electron.*, vol. 27, no. 2–3, pp. 59–210, 2003.

[4] A. Rogalski, "Recent progress in infrared detector technologies," in *Infrared Physics and Technology*, 2011, vol. 54, no. 3, pp. 136–154.

[5] R. D. Hudson, *Infrared system engineering*. Wiley-Interscience, 1969.

[6] W. Herschel, "Experiments on the Refrangibility of the Invisible Rays of the Sun. By William Herschel, LL. D. F. R. S.," *Philos. Trans. R. Soc. London*, vol. 90, no. 0, pp. 284–292, 1800.

[7] T. H. Seebeck, "Uber die Magnetische Polarisation der Metalle und Erze durch Temperatur-Differenz," *Ann. der Phys. und Chemie*, vol. 6, pp. 253–286, 1826.

[8] W. Smith, "Effect of Light on Selenium During the Passage of An Electric Current*," *Nature*, vol. 7, no. 173, pp. 303–303, 1873.

[9] A. Rogalski and K. Chrzanowski, "Infrared devices and techniques (revision)," *Metrol. Meas. Syst.*, vol. 21, no. 4, pp. 565–618, 2014.

[10] N. Chi anh, H. J. Shin, K. Kim, Y. hee Han, and S. Moon, "Characterization of uncooled bolometer with vanadium tungsten oxide infrared active layer," vol. 124, pp. 87–91, 2005.

[11] S. K. Ajmera, a. J. Syllaios, G. S. Tyber, M. F. Taylor, and R. E. Hollingsworth, "Amorphous Silicon Thin-Films for Uncooled Infrared Microbolometer Sensors," vol. 7660, pp. 766012–766012–8, 2010.

[12] V. S. Jagtap, A. F. Dégardin, and A. J. Kreisler, "Low temperature amorphous growth of semiconducting Y – Ba – Cu – O oxide thin fi lms in view of infrared bolometric detection," *Thin Solid Films*, vol. 520, no. 14, pp. 4754–4757, 2012.

[13] Y. Lv, M. Hu, M. Wu, and Z. Liu, "Preparation of Vanadium Oxide Thin Films with High Temperature Coefficient of Resistance," vol. 201, pp. 4969–4972, 2007.

[14] E. Alpman, "Development of Low-Cost Uncooled Infrared Detec tor Arrays in Standard CMOS and SOI-CMOS Processes," Middle East Technical University, 2005.

[15] F. Tankut, "Development and Characterization of Low-Cost Uncooled

Infrared Sensors for Commercial Applications," Middle East Technical University, 2013.

[16] E. Inceturkmen, "A Low Cost 128X128 Uncooled Infrared Detector Array in a Standard SOI CMOS Technology," Middle East Technical University, 2008.

[17] F. Tankut, T. Akın, and S. Eminoğlu, *Development and characterization of low-cost uncooled infrared sensors for commercial applications. [Electronic resource]*. Ankara : METU ; 2013.

[18] R. K. Bhan, R. S. Saxena, C. R. Jalwania, and S. K. Lomash, "Uncooled infrared microbolometer arrays and their characterisation techniques," *Def. Sci. J.*, vol. 59, no. 6, pp. 580–589, 2009.

[19] G. D. Skidmore, C. J. Han, and C. Li, "Uncooled microbolometers at DRS and elsewhere through 2013," vol. 9100, p. 910003, 2014.

[20] P. Eriksson and J. Y. Andersson, "Thermal Characterization of Surface-Micromachined Silicon Nitride Membranes for Thermal Infrared Detectors," vol. 6, no. 1, pp. 55–61, 1997.

[21] Y. J. Y. and S. G. K. Sang Baek Ju, "Design and Fabrication of a High Fill-Factor Microbolometer Using Double Sacrificial Layers."

[22] F. Niklaus, F. Ab, C. Vieider, A. Ab, and H. Jakobsen, "MEMS-Based Uncooled Infrared Bolometer Arrays – A Review," vol. 6836, pp. 1–15, 2007.

[23] M. Kohin and N. R. Butler, "Performance limits of uncooled VOx microbolometer focal plane arrays," *Proc. SPIE*, vol. 5406. pp. 447–453, 2004.

[24] J. and R. V. Clarke, "Flicker Noise: Equilibrium Temperature and Resistance Fluctuations," vol. 13, no. 2, 1976.

[25] F. N. Hooge, "l / f Noise Sources," vol. 41, no. 11, pp. 1926–1935, 1994.

[26] R. A. Wood, "Use of vanadium oxide in microbolometer sensors." Google Patents, 1995.

[27] R. A. Wood, "Uncooled thermal imaging with monolithic silicon focal planes," *Proc. SPIE*, vol. 2020. pp. 322–329, 1993.

[28] C. Li, G. D. Skidmore, C. Howard, C. J. Han, L. Wood, D. Peysha, E. Williams, C. Trujillo, J. Emmett, G. Robas, Others, D. Jardine, C.-F. Wan, and E. Clarke, "Recent development of ultra small pixel uncooled focal plane arrays at DRS," *Proc. SPIE*, vol. 6542, p. 65421Y, 2007.

[29] J.-J. Yon, E. Mottin, and J.-L. Tissot, "Latest amorphous silicon microbolometer developments at LETI-LIR," *Proc. SPIE*, vol. 6940, p. 69401W, 2008.

[30] J. L. Tissot, "LETI/LIR's amorphous silicon uncooled microbolometer development," *Proc. SPIE 3379*, vol. 3379, no. April 1998, pp. 139–144, 1998.

[31] J. J. Yon, A. Astier, S. Bisotto, G. Chamingis, A. Durand, J. L. Martin, E. Mottin, J. L. Ouvrier-Buffet, and J. L. Tissot, "First demonstration of 25 μm pitch uncooled amorphous silicon microbolometer IRFPA at LETI-LIR,"

Proc. SPIE, vol. 5783, pp. 432–440, 2005.

[32] C. Li, G. Skidmore, C. Howard, E. Clarke, and C. J. Han, "Advancement in 17-micron pixel pitch uncooled focal plane arrays," *Proc. SPIE*, vol. 7298, no. April, p. 72980S–72980S–11, 2009.

[33] C. J. Han, R. Rawlings, M. Sweeney, S. Whicker, D. Peysha, E. Clarke, B. Sullivan, C. Li, and P. Howard, "320x240 and 640x480 UFPAs for TWS and DVE Applications," vol. 5783, pp. 559–565, 2005.

[34] C. Li, C. J. Han, and G. Skidmore, "Overview of DRS uncooled VOx infrared detector development," *Opt. Eng.*, vol. 50, no. 6, p. 061017, 2011.

[35] D. S. Tezcan, S. Eminoglu, and T. Akin, "A low-cost uncooled infrared microbolometer detector in standard CMOS technology," *IEEE Trans. Electron Devices*, vol. 50, no. 2, pp. 494–502, 2003.

[36] M. Y. Tanrikulu, "An uncooled infrared microbolometer array using surface micromachined MEMS technology." Dissertation for the Degree of Doctor of Philosophy, 2007.

[37] Ş. E. Küçük, "Development of High Fill Factor and High Performance," 2011.

[38] U. Thermal and U. S. Diode, "a New Uncooled Thermal Ir Detector," pp. 102–107.

[39] J. C. Brasunas, B. Lakew, and R. Fettig, "A comment on the reported detectivity of a new uncooled thermal infrared detector," *Sensors Actuators, A Phys.*, vol. 96, no. 2–3, pp. 211–213, 2002.

[40] T. Ishikawa, M. Ueno, K. Endo, Y. Nakaki, H. Hata, T. Sone, M. Kimata, and T. Ozeki, "Low-cost 320x240 uncooled IRFPA using a conventional silicon IC process," *Proc. SPIE*, vol. 3698. pp. 556–564, 1999.

[41] M. Ueno, Y. Kosasayama, T. Sugino, Y. Nakaki, Y. Fujii, H. Inoue, K. Kama, T. Seto, M. Takeda, and M. Kimata, "640 x 480 pixel uncooled infrared FPA with SOI diode detectors," *Infrared Technol. Appl. XXXI, Pts 1 2*, vol. 5783, pp. 566–577, 2005.

[42] D. Takamuro, T. Maegawa, T. Sugino, Y. Kosasayama, T. Ohnakado, H. Hata, M. Ueno, H. Fukumoto, K. Ishida, H. Katayama, T. Imai, and M. Ueno, "Development of new SOI diode structure for beyond 17 μm pixel pitch SOI diode uncooled IRFPAs," vol. 8012, p. 80121E–80121E–10, 2011.

[43] and K. K. Y. Kosasayama, T. Sugino, Y. Nakaki, M. Ueno, "High sensitive uncooled infrared FPA with SOI diode detectors," *Japan Soc. Infrared Sci. Technol.*, no. February, 2008.

[44] S. Eminoglu, M. Y. Tanrikulu, D. S. Tezcan, and T. Akin, "A low-cost small pixel uncooled infrared detector for large focal plane arrays using a standard CMOS process," *Infrared Detect. Focal Pl. Arrays Vii*, vol. 4721, pp. 111–121, 2002.

[45] S. Eminoglu, M. Y. Tanrikulu, and T. Akin, "A Low Cost 64x64 Uncooled Infrared Detector Array in Standard CMOS," pp. 6–9, 2003.

[46] T. A. Selim Eminoglu, Mahmud Yusuf Tanrikulu, "A Low-Cost 128x128

Uncooled Infrared Detector Array in CMOS Process," *Microelectromechanical Syst. J.*, vol. 17, no. 1, pp. 20–30, 2005.

[47] O. Ertürk and T. Akın, *Design and implementation of high fill factor structures on low-cost uncooled infrared sensors. [Electronic resource]*. Ankara : METU, 2015.

[48] A. W. van Herwaarden and P. M. Sarro, "Thermal sensor based on the seebeck effect," *Sensors and Actuators*, vol. 10, no. 3–4, pp. 321–346, 1986.

[49] P. M. Sarro, "Integrated silicon thermopile infrared detectors," p. 117, 1987.

[50] A. Graf, M. Arndt, M. Sauer, and G. Gerlach, "Review of micromachined thermopiles for infrared detection," *Meas. Sci. Technol.*, vol. 18, no. 7, pp. R59–R75, 2007.

[51] M. C. Foote and S. Gaalema, "Progress Towards High-Performance Thermopile Imaging Arrays," vol. 4369, pp. 350–354, 2001.

[52] C. Calaza, N. Viarani, G. Pedretti, M. Gottardi, A. Simoni, V. Zanini, and M. Zen, "An uncooled infrared focal plane array for low-cost applications fabricated with standard CMOS technology," *Sensors Actuators, A Phys.*, vol. 132, no. 1 SPEC. ISS., pp. 129–138, 2006.

[53] A. Schaufelbühl, N. Schneeberger, U. Münch, M. Waelti, O. Paul, O. Brand, H. Baltes, C. Menolfi, Q. Huang, E. Doering, and M. Loepfe, "Uncooled low-cost thermal imager based on micromachined CMOS integrated sensor array," *J. Microelectromechanical Syst.*, vol. 10, no. 4, pp. 503–510, 2001.

[54] M. C. Foote, M. Kenyon, T. R. Krueger, T. a. McCann, R. Chacon, E. W. Jones, M. R. Dickie, J. T. Schofield, D. J. McCleese, and S. Gaalema, "Thermopile Detector Arrays for Space Science Applications," vol. 4999, no. 2003, pp. 443–447, 2004.

[55] D. Xu, B. Xiong, G. Wu, Y. Ma, and Y. Wang, "Uncooled thermoelectric infrared sensor with advanced micromachining," *IEEE Sens. J.*, vol. 12, no. 6, pp. 2014–2023, 2012.

[56] S. D. Ivanov and E. G. Kostsov, "Thermal Detectors of Uncooled Multi-Element Infrared Imaging Arrays . I . Thermally Insulated Elements," vol. 51, no. 6, pp. 601–608, 2015.

[57] M. Ray, M. D. Jack, W. A. Radford, and D. F. Murphy, "Advanced small pixel high fill factor uncooled focal plane array." Google Patents, 2000.

[58] H. Lee, J. Yoon, E. Yoon, S. Ju, Y. Yong, S. Kim, and A. Display, "A High Fill-Factor IR Bolometer Using Multi-Level Electrothermal Structures," pp. 463–466, 1998.

[59] N. Engheta, "Thin absorbing screens using metamaterial surfaces," *IEEE Antennas Propag. Soc. Int. Symp. (IEEE Cat. No.02CH37313)*, vol. 2, pp. 392–395, 2002.

[60] C. M. Watts, X. Liu, and W. J. Padilla, "Metamaterial Electromagnetic Wave Absorbers," 2012.

[61] N. I. Landy, "A Perfect Metamaterial Absorber," 2008.

[62] B. E. Cole, “Microstructure design for high IR sensitivity.” Google Patents, 2000.

[63] a. D. Parsons, “Thin-film infrared absorber structures for advanced thermal detectors,” *J. Vac. Sci. Technol. A Vacuum, Surfaces, Film.*, vol. 6, no. 3, p. 1686, 1988.

[64] S. P. Lee and C. N. Chen, “Interferometer-based bolometer.” Google Patents, 1997.

[65] D. P. Butler, Z. Celik-Butler, P. C. Shan, and A. Jahanzeb, “Uncooled amorphous YBaCuO thin film infrared detector.” Google Patents, 1998.

[66] A. D. Parsons and D. J. Pedder, “Thin Film Infrared Absorber Structures for Advanced Thermal Detectors,” vol. 1686, no. 1988, 2016.

[67] Q. Cheng, S. Member, S. Paradis, T. Bui, and M. Almasri, “Design of Dual-Band Uncooled Infrared Microbolometer,” vol. 11, no. 1, pp. 167–175, 2011.

[68] L. Wang and X. Li, “Preparation of VO2 Microbolometer for CO2 Gas Detection,” pp. 1774–1777, 2010.

[69] C. Vedel, J. Martin, J. O. Buffet, J. Tissot, M. Vilain, J. Yon, and L. C. E. A. G, “Amorphous Silicon Based Uncooled Microbolometer IRFPA,” vol. 3698, no. April, 1999.

[70] N. T. Eigenfeld, J. M. Gray, J. J. Brown, G. D. Skidmore, S. M. George, and V. M. Bright, “Ultra-thin 3D Nano-Devices from Atomic Layer Deposition on Polyimide,” pp. 3962–3967, 2014.

[71] G. D. Skidmore and C. G. Howard, “Pixel structure having an umbrella type absorber with one or more recesses or channels sized to increase radiation absorption.” Google Patents, 2009.

[72] A. M. Kennedy and S. H. Black, “Pixel structure with reduced vacuum requirements.” Google Patents, 2013.

[73] P. Wang, S. Chen, X. Gan, R. Sun, W. Chen, S. Yang, and H. Wang, “High Sensitivity 17 μ m Pixel Pitch 640 × 512 Uncooled Infrared Focal Plane Arrays Based on Amorphous Vanadium Oxide Thin Films,” vol. 36, no. 9, pp. 923–925, 2015.

[74] H. G. Tompkins and E. A. Irene, *Handbook of Ellipsometry*. Springer Berlin Heidelberg, 2005.

[75] H. Tompkins, “WVASE32 Software Training Manual.” JA Woolaam Inc., Lincoln, NE, 2006.

[76] S. Zhou, W. Liu, C. Cai, H. Liu, S. Province, T. Film, O. Test, and O. Key, “Comparative investigation of infrared optical absorption properties of silicon oxide , oxynitride and nitride films,” vol. 7995, pp. 7–10, 2011.

[77] K. O. Bugaev, A. A. Zelenina, and V. A. Volodin, “Vibrational Spectroscopy of Chemical Species in Silicon and Silicon-Rich Nitride Thin Films,” vol. 2012, 2012.

[78] J. Kischkat, S. Peters, B. Gruska, M. Semtsiv, M. Chashnikova, M. Klinkmüller, O. Fedosenko, S. Machulik, A. Aleksandrova, G. Monastyrskyi,

Y. Flores, and W. T. Masselink, “Mid-infrared optical properties of thin films of aluminum oxide , titanium dioxide , silicon dioxide , aluminum nitride , and silicon nitride,” vol. 51, no. 28, pp. 6789–6798, 2012.

[79] M. Mac, “Infrared Optical Constants and Dielectric Response Functions of Silicon Nitride and Oxynitride Films,” vol. 449, no. 2, pp. 439–449, 2001.

[80] “User’s Guide-High Frequency Structure Simulator.” Ansoft Corp., 2005.

[81] Z. Liu, G. Fang, Y. Wang, Y. Bai, and K. Yao, “Comparison of V2O5 Microbolometer Optical Performance Using NiCr and Ti Thin Films,” vol. 33, no. April, pp. 2327–2332, 2000.

[82] M. H. J. Lee and R. J. Collier, “Measurement of the sheet resistance of thin metallic films at 130GHz,” *Conf. Proc. - 33rd Eur. Microw. Conf. EuMC 2003*, vol. 1, no. 0, pp. 471–474, 2003.